2019

Advanced materials for rechargeable lithium-oxygen batteries and zinc-air batteries

Viet Thien Pham
University of Wollongong

UNIVERSITY OF WOLLONGONG

Australian Institute of Innovative Materials

ADVANCED MATERIALS FOR RECHARGEABLE LITHIUM-OXYGEN BATTERIES AND ZINC-AIR BATTERIES

by

Viet Thien Pham

B.Eng., M. Eng.

This thesis is presented as part of the requirement for the

Award of the Degree of

Doctor of Philosophy

Institute for Superconducting & Electronic Materials

Australian Institute of Innovative Materials

Faculty of Mechanical, Material and Mechatronics Engineering
University of Wollongong, NSW, Australia

The University of Wollongong

CERTIFICATE OF ORIGINALITY

I, Viet Thien Pham, declare that all the works presented in this thesis is original and was carried out at the Institute for Superconducting and Electronic Materials, Faculty of Engineering, University of Wollongong. This thesis, submitted in fulfilment of the requirements for the award of Doctor of Philosophy of Engineering-Research, is wholly my own work unless otherwise referenced or acknowledged. This document has not been submitted for qualifications at any other academic institution.

Viet Thien Pham

Apr, 2019

(Signature)_____

ACKNOWLEDGEMENTS

It is my great pleasure to acknowledge the valuable assistances that I have received from all the people in the Institute for Superconducting and Electronic Materials (ISEM), University of Wollongong, Australia, throughout my doctoral studies.

I firstly wish to express my utmost gratitude to my thesis supervisor, Professor Hua Kun Liu for her guidance, academic supervision, financial support and constant encouragement throughout the project. I am also deeply grateful to my co-supervisors Dr. Wenbin Luo, Prof Shulei Chou, Prof Jiazhao Wang for their supervision and invaluable advice for my research. I also would like to thank Prof. Shi Xue Dou, the director of ISEM, University of Wollongong, for his great support during my study.

I would like to express my appreciation to Prof. Jia Zhao Wang for sharing her valuable time with me in discussions of the background and prospects for lithium-oxygen battery research. Special thanks should be given to Dr. Tania Sliver for critical reading of manuscripts and Mrs. Crystal Mahfouz for her help in official matters. Technical assistance from Dr. Gilberto Casillas (ARM), A Prof. Konstantin Konstantinov (TGA and BET), Dr. Dongqi Shi (XPS) and A Prof.Germanas Peleckis (XRD) is highly appreciated. Dr. Xun Xu, Dr. Jun Wang, Mr. Haipeng Guo, Dr. Li Li Liu, Dr. Yun Xiao Wang and other staffs members and students in ISEM, IPRI, EMC, AIIM, workshop also deserve thanks, for their kindly help and willingness to share knowledge with me during this research.

Finally, I am very grateful for the encouragement and understandings given to me by my parents, and other members of my family who supported me through all my Phd study.

TABLE OF CONTENTS

TABLE OF FIGURES

LIST OF TABLES

ABSTRACT

Metal air batteries, including lithium-oxygen (Li-O_2) and zinc air batteries (ZAB), have drawn research attention around the world due to their superior high energy densities. A Li-O_2 cell discharges to Li_2O_2 product at 3.1 V and could deliver a specific energy as high as 3623 Wh/kg, which makes it a possible candidate system to power a full-size electric car. Up to now, the challenges of metal air batteries have been the cycling instability of electrolytes and their low round–trip efficiency, which could be increased by optimizing the cathode catalysts and structures. In the past ten years, many advances have been achieved, but the challenges remain. In this doctoral work, several promising efficient catalysts for Li-O_2 batteries and ZAB have been synthesized as novel cathode catalysts, and their electrical performances have been investigated in details. These include $LaNi_{0.9}Cu_{0.1}O_3$ perovskite oxide nanosheets, arrays of TiN@Pt_3Cu nanowires, and Ni_3Pt alloy. These porous structures support fast O_2 and electrolyte transport as well as forming a continuous conductive network throughout the whole energy

conversion process. The electrolytes for Li-O_2 batteries include organic solvents and lithium salts, and the electrolyte for the ZAB is an alkaline solution. The electrolyte usually suffers from degradation during cycling. Herein, a gel electrolyte was designed for the ZAB, which can not only avoid electrolyte evaporation, but also provides a flexible structure. In this work, Ni_3Pt alloy deposited on nickel foam was employed as the cathode material. The results show that the gel electrolyte has high ionic conductivity and low activation energy with a high operating voltage.

This PhD study was begun by studying carbon- and binder-free three-dimensional (3D) perovskite oxide as air electrode for Li-O_2 batteries. Transition-metal-doped perovskite oxide $LaNi_{0.9}M_{0.1}O_3$ (M = Cu, Co) nanosheets were grown on nickel foam to serve as a complete carbon- and binder-free 3D porous air electrode for lithium–oxygen batteries. The design of this porous air electrode can facilitate rapid gas and electrolyte diffusion, as well as forming a continuous electronically conductive network throughout the whole energy conversion process. Because of the combination of abundant lattice strain and the oxygen vacancy effect caused by substitution of an element with a different valence state in Ni sites, $LaNi_{0.9}Cu_{0.1}O_3$ exhibits a significant oxygen reduction reaction (ORR) and oxygen evolution reaction (OER), showing improvement in both aqueous and non-aqueous systems compared with pure $LaNiO_3$ and $LaNi_{0.9}Co_{0.1}O_3$. Especially with the redox mediator additive tetrathiafulvalene (TTF) in the electrolyte, this $LaNi_{0.9}Cu_{0.1}O_3$ perovskite oxide nanosheet catalyst grown on 3D microporous nickel foam exhibits excellent bifunctional catalytic activity in the Li-O_2 battery, showing the same highly active catalytic kinetics and high round-trip efficiency as those of reported precious metal catalysts. The overpotential remains at 0.72 V, and the round-trip efficiency is as high as 80% under a current density of 0.1 mA cm^{-2}, with capacity limited to 1000 mA h g^{-1}.

Secondly, TiN@Pt_3Cu nanowire arrays were applied as an efficient electrode for Li-O_2 batteries. To achieve high round-trip efficiency and satisfactory cycling stability, the air electrode

structure and the electrocatalysts play important roles. Here, a 3D array composed of one-dimensional TiN@Pt_3Cu nanowires was synthesized and employed as a completely porous air electrode in a lithium–oxygen battery. The TiN nanowires were primarily used as an air electrode frame and catalyst support to provide a network with high electronic conductivity because of the high-orientation of the one-dimensional crystalline structure. Meanwhile, the deposited icosahedral Pt_3Cu nanocrystals exhibit highly efficient catalytic activity owing to the abundant {111} active lattice facets and multiple twin boundaries. This porous air electrode comprises a one-dimensional TiN@Pt_3Cu nanowire array that demonstrates excellent energy conversion efficiency and rate performance in full discharge and charge modes. The discharge capacity is as high as 4600 mAh g^{-1} along with an 84% conversion efficiency at a current density of 0.2 mA cm^{-2}, and when the current density was increased to 0.8 mA cm^{-2}, the discharge capacity was still greater than 3500 mAh g^{-1} with nearly 70% efficiency. This designed array is a promising bi-functional porous air electrode for Li-O_2 batteries, forming a continuous conductive network with high catalytic activity to facilitate rapid gas and electrolyte diffusion, and catalytic reactions throughout the whole energy conversion process.

Finally, an integrated air electrode was designed for the ZAB. The Ni_3Pt alloy was deposited on 3D nickel foam by pulsed laser deposition for use as an integrated air electrode for rechargeable ZAB. The conductive nickel foam and the Ni_3Pt electrocatalyst loaded on the nickel foam create a porous and conductive integrated air electrode that favors rapid gas and electrolyte diffusion throughout the whole energy conversion process. The high electrocatalytic activity of Ni_3Pt alloy was investigated by rotating disk electrode, and the design of the air electrode is crucial for the performance of the air battery. The ZAB in this work can operate with overpotential below 0.62 V for 478 cycles (10 minutes per cycle) under a current density of 10 mA cm^{-2}, and the charge potential always stays lower than 1.7 V. The high performance ZAB enabled in this work paves the way for a promising technique to fabricate cathodes by pulsed laser deposition.

ABBREVIATIONS

ARM	Atomic resolution analytical microscope
BET	Brunauer-Emmett-Teller
CNTs	Carbon nanotubes
CNFs	Carbon nanofibers
CV	Cyclic voltammetry
DEC	Diethyl carbonate
DMC	Dimethyl carbonate
E_a	Activation energy
EC	Ethylene carbonate
EDS	Energy dispersive spectroscopy
EG	Ethylene glycol
EMC	Ethyl methyl carbonate
EIS	Electrochemical impedance spectroscopy
ETPTA	Ethoxylated trimethylolpropane triacrylate
EV	Electric vehicle
FESEM	Field emission scanning electron microscopy
GC	Glassy carbon
GDL	Gas diffusion layer
GFS	Glass fiber separator
GPEs	Gel-polymer electrolyte
HEV	Hybrid electric vehicle

HRTEM	High-resolution transmission electron microscope
IL	Ionic liquid
LIB	Lithium-ion battery
LiTFSI	Lithium bis-(trifluoromethanesulfonyl) imide
LSV	Linear sweep voltammetry
MAB	Metal air battery
MTMO	Mixed transition-metal oxide
NGM-Co	hierarchical Co/N/O tri-doped graphene
NMP	N-methyl-2-pyrrolidinone
OER	Oxygen evolution reaction
ORR	Oxygen reduction reaction
PC	Propylene carbonate
PTFE	Poly(tetrafluoroethylene)
PVP	Polyvinyl pyridine
PVDF	Polyvinylidene fluoride
PHEVs	Plug-in hybrid electric vehicles
RDE	Rotating disk electrode
SAED	Selected area electron diffraction
SEI	Solid electrolyte interphase
STEM	Scanning transmission electron microscopy
SEM	Scanning electron microscopy
TEM	Transmission electron microscope
TGA	Thermogravimetric analysis
XRD	X-ray diffraction
XPS	X-ray photoelectron spectroscopy
F	Faraday

mW	Miliwatt
g	Gram
mins	Minutes
hrs	Hours
M	Moles per litre
nm	Nanometre
V	Volts
ZAB	Zinc air battery

Chapter 1 Introduction

The effort to replace petrol cars by electric vehicles and the utilization of renewable energy are intended to solve the problems of climate change, energy security, and sustainability. The metal air battery (MAB) with superior theoretical energy density (up to 2-3 kW kg^{-1}) is considered as the next-generation energy storage and conversion device. The performance of a MAB depends on the effectiveness of the catalyst for the oxygen reduction reaction (ORR) during the discharge process and the oxygen evolution reaction (OER) during the charge process. A Li-O_2 cell discharging to Li_2O_2 product at 3.1 V could deliver a specific energy as high as 3623 Wh/kg, which makes it a possible candidate system to power a full-size electric car. Another type of MAB is the rechargeable zinc air battery (ZAB), which has a theoretical energy density of 1086 Wh/kg. The ZAB contains zinc metal and alkaline electrolyte, which are more environmentally friendly than the Li metal and organic electrolyte of Li-O_2. The motivation of this Phd study is to develop new MABs such as Li-O_2 and ZAB with superior energy density (1-3 kWh/kg). The study in this thesis also explore new materials such as $LaNi_{0.9}Cu_{0.1}O_3$ perovskite oxide nanosheets, arrays of TiN@Pt_3Cu nanowires, and Ni_3Pt alloy as efficient catalyst for oxygen reduction reaction (ORR) and oxygen evolution reaction (OER).

The Li-O_2 battery can be divided to four types of structure, based on the electrolyte used in the battery: non-aqueous, aqueous, hybrid, and all-solid-state batteries. Among the four categories, the non-aqueous system is the most studied one. Therefore, this thesis is focused on the research on non-aqueous Li-O_2 batteries. The rechargeable ZAB includes an alkaline electrolyte, however, which is aqueous and makes it feasible to test the battery in the normal air environment.

The MAB is composed of a metal anode, a porous air cathode, and an electrolyte between the two electrodes. The research effort on MABs could be described in terms of the following directions: (1) exploration of new electrocatalyst materials, (2) improvement of the stability and performance of the battery electrolyte, and (3) anode stabilization. In this PhD project, various types of electrocatalysts were designed for Li-O_2 batteries and ZABs. Additionally, a gel electrolyte consisting of polyvinyl alcohol (PVA), KOH, and water was introduced for the rechargeable ZAB.

The scope of this thesis is covered as follow:

Chapter 1 includes the introduction and an outline of the thesis.

Chapter 2 contains a detailed literature review on Li-O_2 batteries and ZABs. This chapter covers the general background and current challenges for rechargeable Li-O_2 batteries and ZABs.

Chapter 3 starts with the synthesis method for electrocatalysts, and the physical and electrochemical characterization techniques used in this PhD study.

In Chapter 4, the hydrothermal method was used to fabricate one-dimensional perovskite oxide $LaNi_{0.9}M_{0.1}O_3$ (M = Cu, Co) nanosheets as an efficient catalyst for the ORR and OER in Li-O_2 batteries.

In Chapter 5, an array of one-dimensional TiN@Pt_3Cu nanowires was studied, in which the TiN creates an electronically conductive cathode network. This material delivers excellent performance in Li-O_2 cells with discharge capacity as high as 4600 mAh g^{-1} and conversion efficiency of 84% at a current density of 0.2 mA cm^{-2}.

In Chapter 6, Ni_3Pt alloy was coated on nickel foam by pulsed laser deposition. The high electrocatalytic activity of Ni_3Pt alloy was investigated by rotating disk electrode, and the design of the air electrode is crucial for the performance of the air battery. The zinc air battery in this work can operate with overpotential below 0.62 V for 478 cycles (10 minutes per cycle) under a current density of 10 mA cm^{-2}, and the charge potential always stays lower than 1.7 V.

Chapter 7 outlines the significant outcomes and achievements of this thesis, accompanied by a reference list and publications gained during the PhD study.

Chapter 2 Literature Review

Oil price swings and the climate change issue have forced us to search for new energy storage systems, such as smart grid. The lithium-ion batteries (LIBs), which possesses higher energy density than previous power sources such as nickel metal hydride (Ni-MH) batteries are being considered to fulfil the world's energy storage demands. Nevertheless, the maximum energy density of current LIBs, which is limited by the intercalation chemistry, cannot meet the requirements for electric vehicles (EVs). As a result, the metal air batteries (MABs) are considered as an alternative to the current LIBs due to their extremely high energy density (**Figure 2.1**).

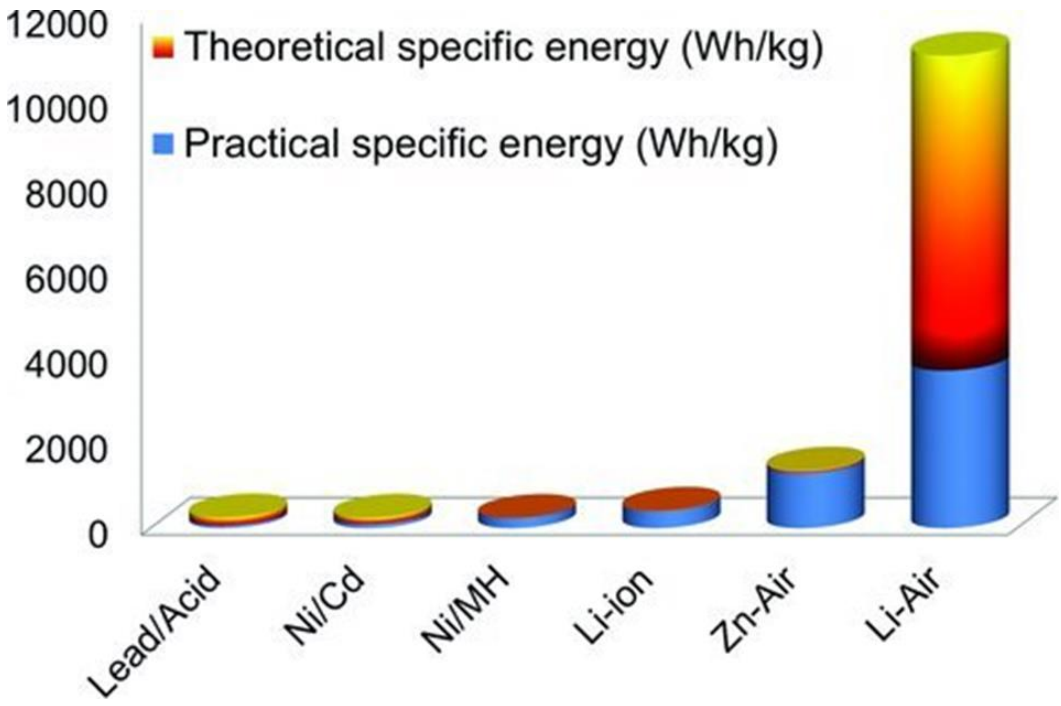

Figure 2.1 Theoretical and practical energy densities of various types of rechargeable battery. [1]

In Figure 2.1, the rechargeable Zn-Air and Li-Air are considered as the two new alternative batteries to replace the LIBs in the future, although there are still many challenges and

difficulties for developing real commercialized Li-Air and Zn-Air batteries. The background on these two systems will be covered in the next sections.

2.1 Lithium oxygen batteries

2.1.1 General background and brief history

34 % of the world's total primary energy is used for automobile applications such as in cars, trucks, and other petrol engine vehicles. This is considered as a major cause of geopolitical instability. As a result, the first hybrid electric vehicles (HEVs) and plug-in hybrid electric vehicles (PHEVs) were fabricated by Toyota. After that, Tesla introduced pure electric vehicles (PEVs) onto the market [2-5]. The use of alternative energy sources, such as solar and wind power, could limit our dependence on fossil fuels and, thus reduce CO_2 emissions. Better energy storage devices are highly demanding. One of the most viable candidates for such devices is the rechargeable Li battery [2, 6]. Among the variable storage systems, the lithium (Li) ion battery (LIB) is the most promising candidate due to its high specific energy (150 Wh/kg), high energy density (650 Wh/l) [7], good rate capability and safety, and low cost. At the level of powering a vehicle, however, gasoline still outperforms Li ion batteries due to its huge specific energy density (12888 Wh/kg) and volumetric energy density (9500 Wh/l)[8]. In order to meet electric vehicle (EV) requirements, new systems with higher specific energy than the lithium ion battery need to be considered.

In 1996, Abraham reported the first rechargeable Li-O_2 battery [5], which included a Li anode [10], an organic-impregnated polyacrylonitrile electrolyte, and a carbon electrode. A decade later, the Bruce group introduced a non-aqueous Li-O_2 battery with a lithium anode, 1 M $LiPF_6$ in propylene carbonate as electrolyte, and α-MnO_2 nanowires as the cathode catalyst

[11]. The new materials delivered capacity of 730 mAh/g (including mass of carbon, binder, and electrode) at a discharge voltage of 2.75 V. For the past ten years, many groups have reported their work on the Li-O_2 battery with new catalyst materials [12, 13], new architectures [14, 15], and improved performance [14-21]. There are many challenges in developing the Li-O_2 battery, however [9]. A lithium oxygen (Li-O_2) battery discharging to Li_2O_2 at 3.1 V has specific energy of 3623 Wh/kg [9], which is significantly higher than that of the lithium ion battery.

The simple structure and large specific capacity of the Li-O_2 battery have attracted much attention around the world. New developments in materials technology have paved the way for research efforts on Li-O_2 batteries [22, 23]. Several research groups are now developing advanced catalysts and cathode substrates to increase their round-trip efficiency and cycle life using mostly organic electrolytes. Most cathode materials include porous carbon, graphene, and carbon nanotubes (CNTs) [21,24] or carbon nanofibers (CNFs) [24, 25] with catalysts such as metal oxides (MnO_2 [26, 27], Co_3O_4 [28, 29]), noble metals [30], and other materials [31,32].

Another factor that affect battery performance is the electrolyte. The solubility, diffusion coefficients, and partial pressure of O_2 in the electrolyte can enhance the battery efficiency significantly [33, 34]. Read and co-workers [35] started the research on electrolytes and showed that the discharge product is Li_2O_2/Li_2O and that the formation of these oxides in the cathode is a function of the electrolyte type and discharge rate. It was shown that the Li_2O discharge product can discharge at a voltage below 2.0 V (vs. Li/Li+). By limiting the discharge voltage to above 2.0 V, the formation of Li_2O is expected to take place. At a voltage of 2.9 V, the formation of Li_2O_2 was demonstrated. In 2009, IBM launched a project to develop electric vehicles that were powered by Li-O_2 batteries [36]. As the complex structure of air battery is

under heavy research, more aspects are being brought into focus to improve the battery performance [1].

2.1.2 Working mechanism

The working mechanism of the Li-O_2 battery can be found in Figure 2.2(a), which shows a schematic diagram of a Li-O_2 cell [37]. The cell includes a Li metal anode, 1 M lithium bis(trifluoromethanesulfonyl)imide (LiTFSI) in propylene carbonate electrolyte dropped on a 250 μm thick glass mat fiber separator, and a cathode. In this case, the cathode is a mixture of Super P, α-MnO_2, polyvinylidene fluoride (PVDF) in a ratio of 54:10:36. The paste was loaded on Ni foam, which served as the current collector.

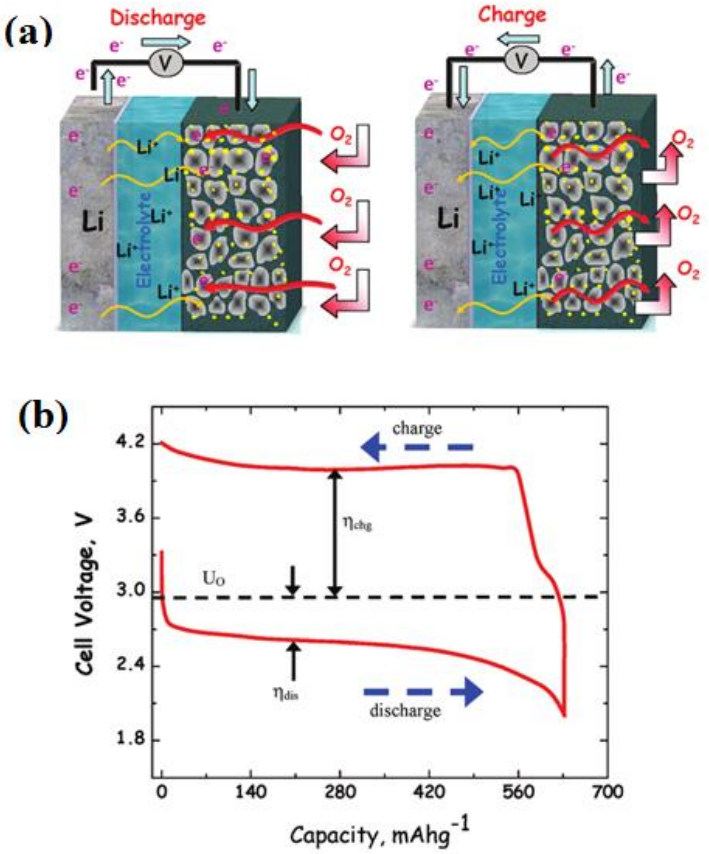

Figure 2.2 (a) Schematic operation proposed and (b) a typical measured discharge-charge cycle (based on Super P (SP) carbon) for rechargeable nonaqueous Li-O_2 batteries. [37]

Figure 2.2(b) shows the discharge and charge profile of the cell. As the battery discharges, Li metal is oxidized to Li^+ ions and electrons ($Li \rightarrow Li^+ + e^-$). The Li ions move through the electrolyte to the cathode, and the electrons move through external circuit to cathode. At the cathode, Li ions are reduced by oxygen (O_2) to form the lithium peroxide (Li_2O_2) discharge product ($2\ Li^+ + O_2 + 2e^- \rightarrow Li_2O_2$). Since O_2 is reduced during discharge, people often call this the oxygen-reduction reaction (ORR). The standard potential of the discharge reaction is U_o = 2.96 V, using the Nernst equation. In the charging process, a voltage $U > U_o$ applied on the external circuit will reverse the discharge process. During the charge process, Li_2O_2 is oxidized to form Li ions, O_2, and electrons ($Li_2O_2 \rightarrow 2Li^+ + O_2 + 2e^-$). Electrons will move to the anode through external circuit, and Li ions will move through the electrolyte to anode. Finally, the Li ions are reduced at the anode to reform Li metal. Because an external voltage oxidizes Li_2O_2 to O_2 during charging, people often call this the oxygen evolution reaction (OER).

From Figure 2.2(b), the discharge voltage stays below 2.96 V. The discharge overpotential (η_{dis}) is around 0.2 V, which originates from the insolubility of Li_2O_2. As the discharge process continues, Li_2O_2 builds up on the cathode surface and blocks access of the reacting species (Li^+, O_2, and electrons) to the active surface. This process explains how the overpotential increases during discharge. At the end of the discharge process, a significant amount of Li_2O_2 has accumulated at the cathode, which requires a large charge overpotential (η_{chg}) of 0.8 V to oxidize the Li_2O_2 back to Li^+, O_2, and electrons. Due to the high η_{dis} and η_{chg}, the ratio of the discharge voltage to the charge voltage is 2.6 V/4 V = 65% [37], which means that 35% of the energy was wasted during the charge/discharge process. Since this review was reported in 2010 [37], many groups have improved battery performance during cycling and addressed low overpotential by using new catalyst materials [38].

2.1.3 Basic concepts

Basic concepts are described as followed to explain battery operation and related electrochemical processes:

- Potential

The theromodynamic and kinetic equations that arise from the properties of the active species involved are used to describe the battery characteristics. Each electrochemical reactions is related to a standard electrode potential, E^0, which can be calculated from the Gibbs free energy under equilibrium conditions:

(2.1) $\Delta G = W = -nFE^0$

Where ΔG is the Gibbs free energy, W is the work, F is the Faraday constant (96485 C), n is the number of electrons involved in a stoichiometric reaction, and E^0 is the electrode potential.

- Overpotential

In electrochemistry, the overpotential is the potential difference (voltage) between a half-reaction's thermodynamically determined reduction potential and the potential at which the redox event is experimentally observed. The term is directly related to a cell's voltage efficiency.

- Charging

Charging is the process in which a secondary cell or rechargeable battery is charged with energy by the input of an electric current. The battery is restored to ots charged condition by applying a charging current for a certain period of time.

- Discharging

The operation of a cell or battery in which the battery provides a certain current and voltage to an output device.

- Specific energy and Energy density

Energy density is the amount of energy stored in a given system or region of space per unit volume ($Wh \cdot l^{-1}$). Additionally, it may also be used for energy per unit mass ($Wh \cdot kg^{-1}$), and the accurate term for this is specific energy.

- Energy efficiency

Energy efficiency (η) is the ratio between the discharge specific energy of the cell and the charge specific energy, in energy terms. In the air battery system, energy efficiency is determined by the properties of the electrocatalysts in the cells.

(2.2) $Energy\ efficiency = Q_d / Q_c \times 100\ \%$

2.1.4 Opportunity and challenges

(a) High energy density and low rate capability

Research on the Li-O_2 battery has been carried out for more than 40 years, although the results are still not at the practical level. The requirement for a high energy density battery is urgent, but there are many challenges. One of the problems is the rate capability. Up to now, only limited current densities have been reported, and generally, the discharge current is one or two orders of magnitude lower than for commercial Li-ion batteries. The low current density can be related to the rates of the ORR and OER reactions at the cathode, which can be improved by developing better electrocatalysts.

(b) Problems with the ambient gas

The term "Li-O_2 battery" also explain another problem of this type of battery. The ambient air is consists of N_2 (78 %) and O_2 (21 %) with other gases making up the rest. CO_2 and moisture in the ambient air can significantly influence the electrochemical performance of a Li-O_2 cell with a negative impact on cyclability, even in small amounts [39, 40]. For example, lithium metal can react with H_2O in the air and form LiOH and H_2. Aurbach's work [39,40] showed that CO_2 can also react with the Li ions to form Li_2CO_3 on the electrode surface, and

Takechi et al. [41] also pointed out that Li_2CO_3 can be formed by the reaction of CO_2 and Li_2O_2. In order to solve the CO_2 and H_2O problems, O_2-selective membranes are currently under intense development.

(c) Catalyst and electrolyte issues

Among the multiple issues affecting the Li-O_2 battery performance, low ORR activity is the main issue reported. The cathode ORR in a Li-O_2 battery is slower than the Li oxidation in LIBs, which explains why the rate capability in a Li-O_2 battery is poorer than in LIBs [42, 43]. Therefore, the cathode catalyst in Li-O_2 batteries has gained more research focus than the anode part, explaining the numerous research reports focused on the cathode catalysts [44]. MnO_2 was reported to reduce the overpotential of the battery [3, 11, 26]. Several types of electrolytes have been applied in Li-O_2 batteries, including propylene carbonate (PC) [45], dimethoxyethane (DME) [46], tetraethylene glycol dimethyl ether (TEGDME) [47], dimethylformamide (DMF) [48], dimethylsulfoxide (DMSO), tetramethylene sulfone [49], etc. Most of the electrolytes above are not stable and are easily attacked by the discharge species such as O^{2-}, O_2^{2-} (Li_2O_2), LiO_2, and LiO_2^- [50]. Choosing the right electrolyte is essential for improving the performance of Li-O_2 batteries. It was reported that carbon-based electrolyte is not stable in an oxygen environment, while ether based electrolytes such as TEGDME are more stable than carbon based electrolytes. Additionally, a redox mediator was reported to reduce the overpotential in lithium-oxygen batteries [51]. The redox mediator can suppress the charging instability of Li-O_2 batteries and improve the discharge process. In this doctoral thesis, tetrathiafulvalene (TTF) mediator [52, 53] was used to improve the charge process in Li-O_2 cells.

2.1.5 Cathode materials

(a) Air cathode: good electronic, ionic conduction, fast oxygen diffusion, and a high degree of porosity

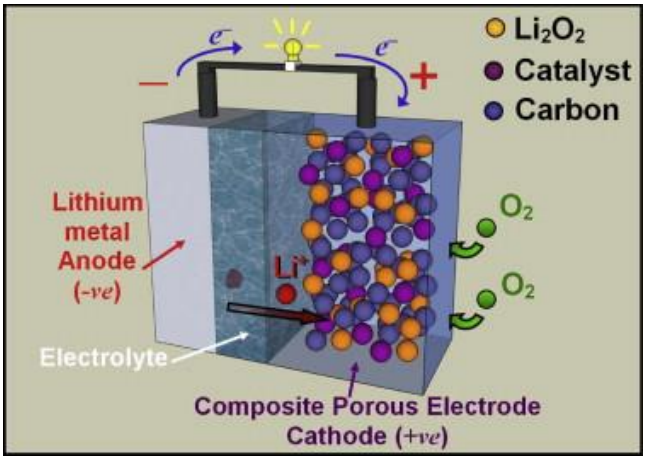

Figure 2.3 Schematic illustration of a rechargeable Li–O_2 battery. Lithium metal anode; porous α-MnO_2-catalyzed Li_2O_2 cathode, $LiPF_6$-propylene carbonate organic electrolyte.[54]

The cathode materials include catalysts (Pt, Au, Ru, α-MnO_2, etc.), conductive carbon (super P, Ketjenblack (KB), reduced graphene oxide (rGO)), and binders (PVDF, polytetrafluoroethylene (PTFE), etc.) loaded on the current collector (stainless steel mesh, Ni foam, carbon paper, etc.). In a Li-O_2 battery, the cathode plays a vital role [9]. A good cathode needs to host the discharge product (Li_2O_2, Li_2O, or LiOH) and facilitate the discharge process, which oxidizes those species back to Li^+, O_2, and electrons. The cathode materials should feature the following properties: good electronic and ionic conductivity, fast oxygen diffusion, and a high degree of porosity. These properties make graphene [17-19,55-57], 3D foam-like $NiCo_2O_4$ [58] [**Figure 2.4**], porous Co_3O_4 [59][**Figure 2.5**], spongy $LaNiCo_3$ nanocubes [38][**Figure 2.6**], and other materials with large surface area ideal candidates for Li-O_2 cathode catalysts [60]. The porous materials tend to provide large surface area; as a result, they produce the high number of active sites, which enhance the reaction to

form Li_2O_2 in discharge process. The improvement of Li_2O_2 accumulation helps increase the discharge voltage of Li-O_2 batteries. The high number of active sites also enhance the Li_2O_2 decomposition, which occurs in the charge process.

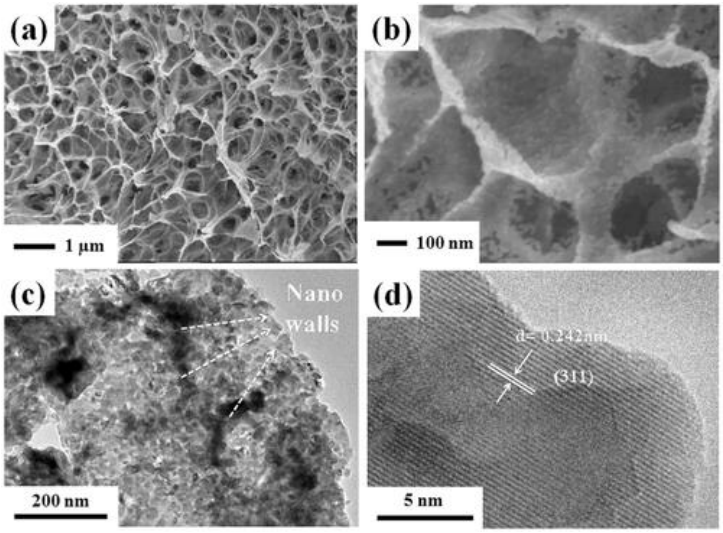

Figure 2.4 (a, b) High resolution scanning electron microscope (HRSEM) images, (c) transmission electron microscope (TEM) image, with the dashed lines indicating the nanowalls, and (d) high resolution TEM (HRTEM) image of the as-prepared 3D foam-like $NiCo_2O_4$.[58]

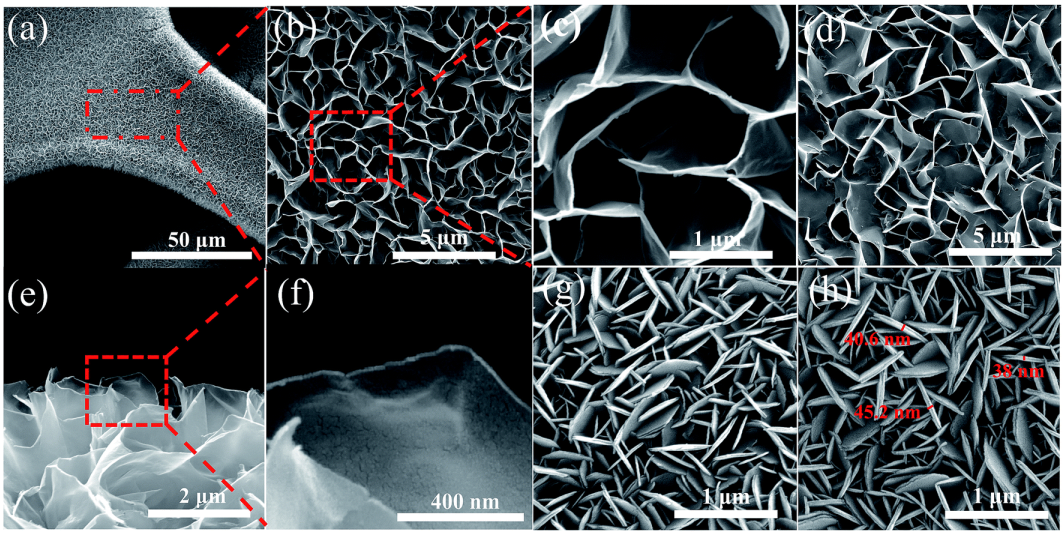

Figure 2.5 (a–c) Scanning electron microscope (SEM) images of the ethylene glycol-cobalt oxide CoO_3 (EG-CO) sample at different magnifications viewed from the top; (d) SEM image of the EG-CO precursor; (e and f) SEM images of the EG-CO sample viewed from the side; (g) SEM images of the de-ionized water–cobalt oxide CoO_3 (DW-CO) precursor and (h) SEM image of the DW-CO sample.[59]

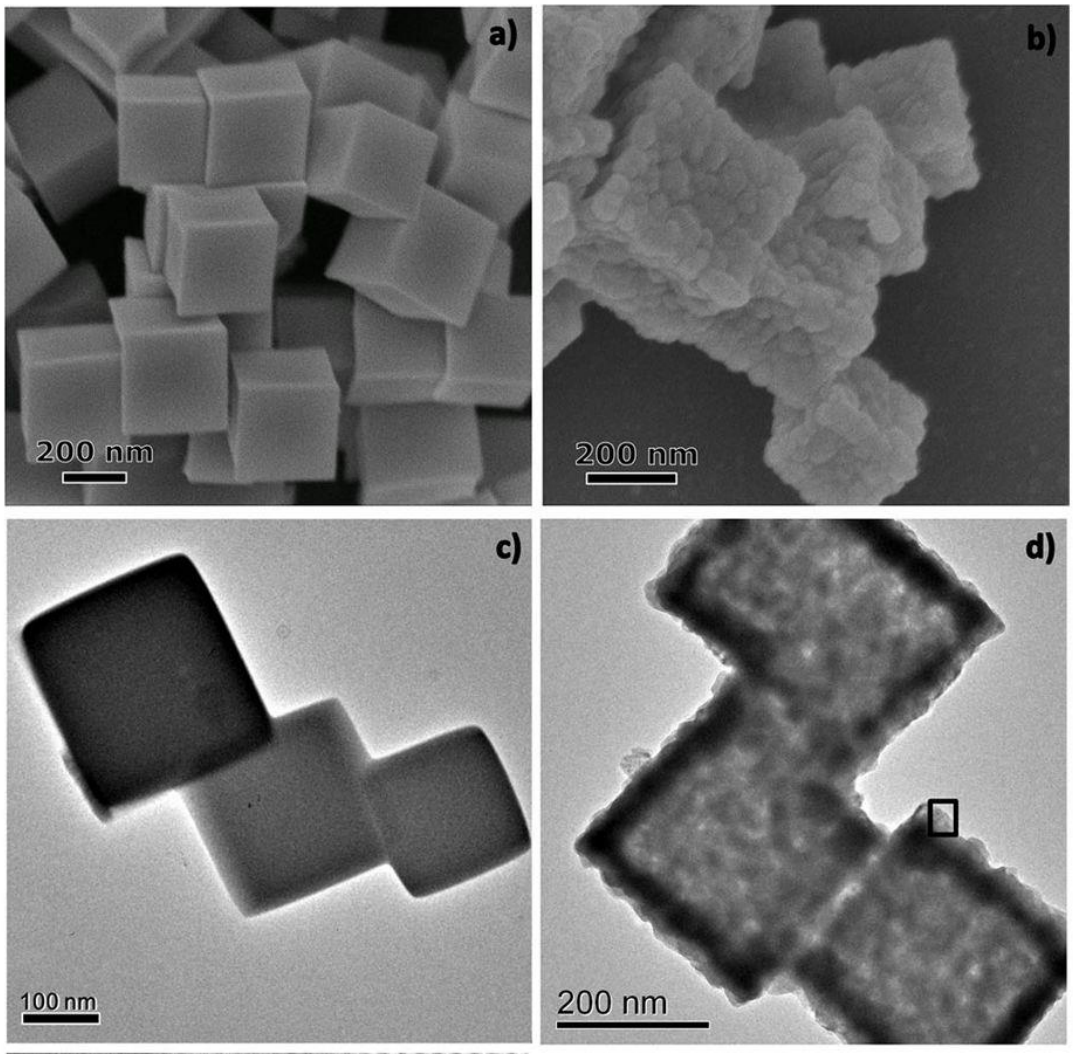

Figure 2.6 SEM (a, b) and TEM (c, d) images of the obtained $LaNiO_3$ nanocubes before (a, c) and after (b, d) annealing, respectively. [38]

(b) Current collector

Firstly, the current collector at cathode should serve as gas diffusion layer (GDL), which allows O_2 to go through the electrode for the discharge process. Secondly, the cathode needs to be stable during charge and discharge, and the current collector provides support. Metal mesh [14, 21], metal foam [12, 52], and carbonaceous substrates [61] [**Figure 2.7**] are commonly used as current collectors in Li-O_2 batteries.

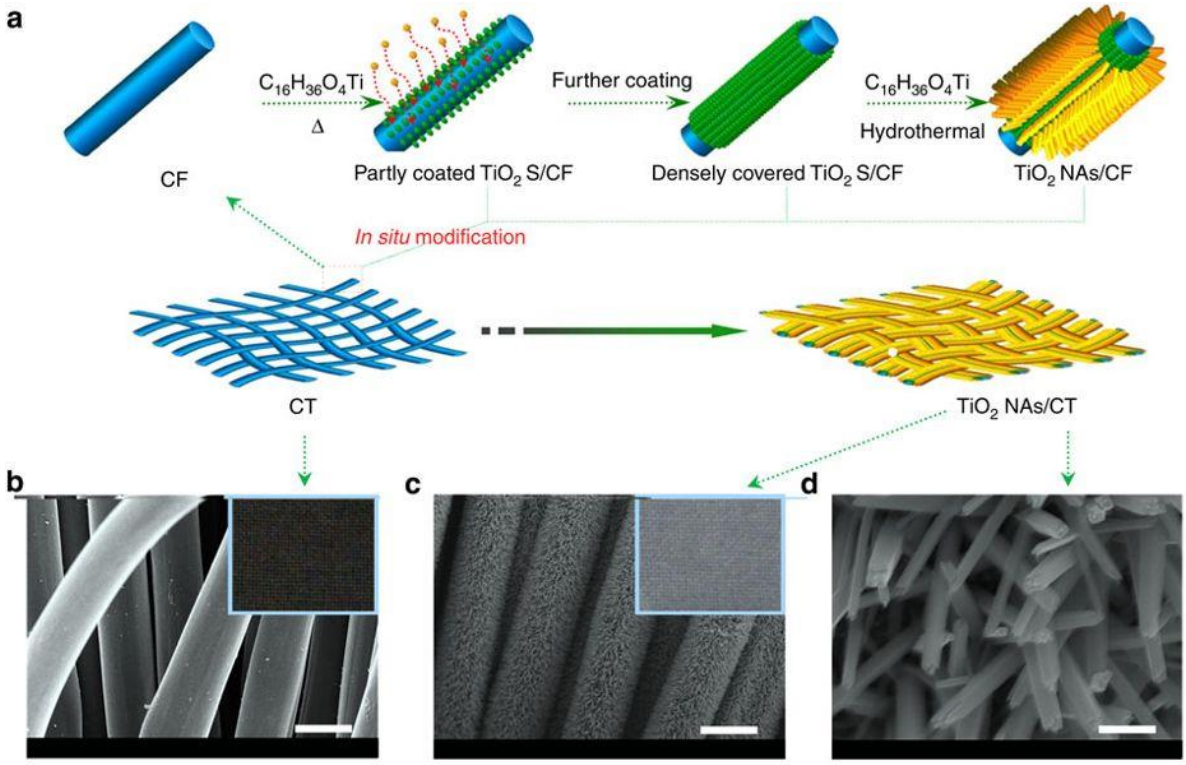

Figure 2.7 (**a**) Schematic illustration of the design and preparation of hierarchical rutile TiO_2 nanowire arrays (TiO_2 NAs)/ grown on carbon textiles (CT). (**b**) Scanning electron microscope image and photograph (inset) of pristine–CT (scale bar, 10 μm). (**c**) SEM image and photograph (inset) of the obtained TiO_2 NAs/CT cathode (scale bar, 10 μm). (**d**) Enlarged image of **c.** Scale bars: 500 nm. [61]

Carbon based supports have the advantage of low mass advantage, although carbon tends to react with Li_2O_2 to form Li_2CO_3 [46, 62-64] at a high charge voltage via following reactions [60].

$$Li_2O_2 + C + 1/2O_2 \rightarrow Li_2CO_3$$

$$2Li_2O_2 + C \rightarrow Li_2O + Li_2CO_3$$

Carbon oxidation can be avoided by using a metal substrate such as Ni foam. Ni foam serves as both a current collector and a substrate to grow the catalyst [12, 52, 59, 65-68].

(c) ORR and OER catalysts

In Li-O_2 batteries, the catalyst can work as an ORR or OER catalyst. The materials will lower the activation barrier of the reaction (possibly reducing the activation energy of the reaction). As a result, the discharge overpotential (η_{dis}) or charge overpotential (η_{chg}) could be

significantly reduced. In 2010, the Shao Horn group introduced the use of platinum−gold nanoparticles as a bifunctional catalyst [20]. **Figure 2.8** shows how Au catalyses the ORR process and Pt enhances the OER step. In the past nine years, many groups have reported several new catalyst materials with the excellent bifunctional ORR-OER effects [11, 13, 16-17, 19, 20, 37]. Based on their chemical composition, catalysts could be divided into four groups, including porous carbon materials, precious metals, non-precious metals, and transition metal oxides.

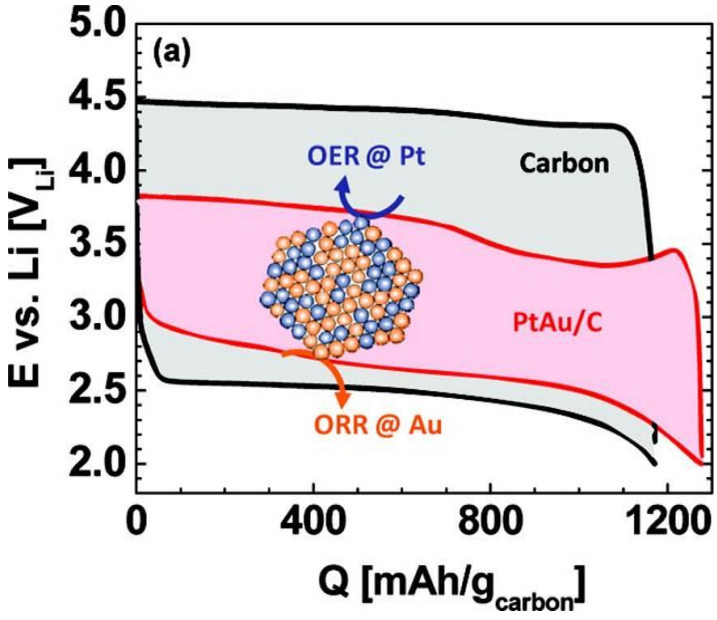

Figure 2.8 Li−O_2 cell discharge/charge profiles of carbon (black, 85 mA/g_{carbon}) and PtAu/C (red, 100 mA/g_{carbon}) in the third cycle at 0.04 mA/cm^2 electrode, with the inset showing the structure of the PtAu catalyst. [20]

(c1) Porous carbon materials

Carbon based catalysts offer high capacity due to their low mass [9]. Additionally, carbonaceous cathode is a good electronic conductor that facilitates electron transport. In most cases, carbon improves the ORR activity of discharge process [19]. The strategy has to combine carbon materials such as graphene [19, 55], CNT [69], or N-doped carbon [70] with other OER catalyst materials as bi-functional catalysts.

Despite its good performance, carbon creates two problems. Firstly, carbon reacts with Li_2O_2 to form Li_2CO_3 at high charge voltages [64]. Secondly, most carbonaceous materials are hydrophobic. As a result, the non-aqueous electrolyte wets the entire catalyst surface, which restricts the flow of oxygen in the air electrode [60]. In general, carbon is the most popular material. It has drawbacks in the OER process, however, and reacts with Li_2O_2 at high charge voltage [60]. Other catalysts with both excellent ORR and excellent OER performance are necessary to boost Li-O_2 battery performance.

(c2) Precious metals

Despite their high cost, noble metals such as Pt, Au, Ru, Ag, and Pd have been used as catalysts for both OER and ORR processes for many years [19- 21, 71]. In 2010, the Shao-Horn group reported the use of Pt-Au nanoparticles as a bifunctional catalyst [20] (Figure 2.8). Later, Lee discovered that ruthenium oxide (Ru_2O) could improve the OER process significantly [19] (**Figure 2.9**). The charge potential was reduced to 3.7 V, which is significantly low compared to the charge potential at 4.5 V of charged carbon. Recently, Pt alloy [21] was proved efficient for improving the specific capacity and overpotential in Li-O_2 batteries (**Figure 2.10**). The Li-O_2 cell using Lou et al.'s Pt-Gd catalyst could be cycled at 4000 mAh g^{-1} with the overpotential at 0.8 V.[21]

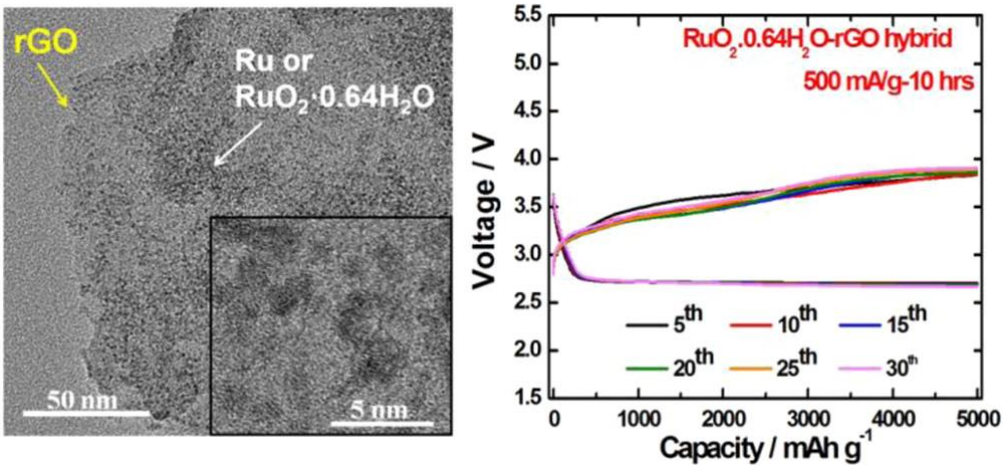

Figure 2.9 TEM image with enlargement in inset (left) and discharge–charge cycles (right) of Li-air cells using RuO_2·O.64H_2O-rGO hybrid as catalyst material. [19]

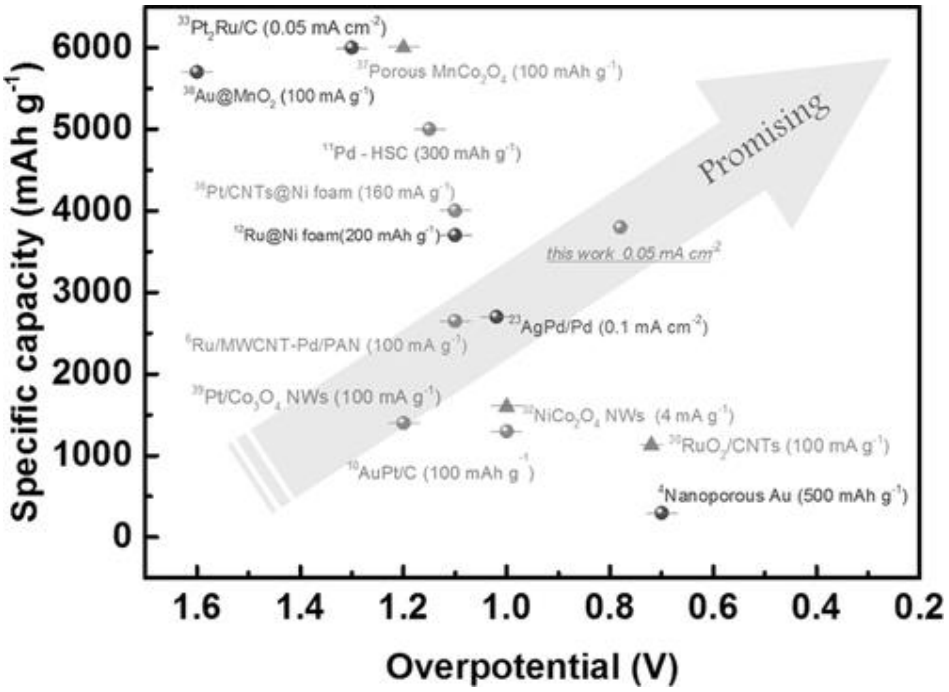

Figure 2.10 Full discharge capacity and overpotential results from previously published works on cathode electrocatalysts. [21]

(c3) Non-precious metals

Transition metal–nitrogen–carbon (M–N/C, M = Fe, Co, etc.) nanostructures are the most promising class of non-precious metal catalysts (NPMCs) for the ORR process. In 2012, work from Shui et al. showed that Fe/N/C composite [72] could lower the charge potential compared to α-MnO_2, which was earlier reported by the Bruce group [11].

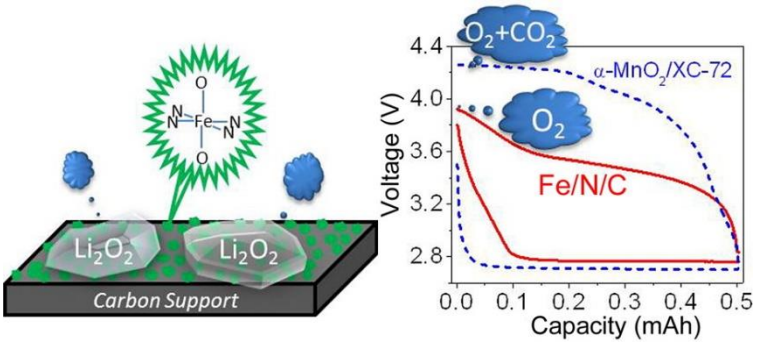

Figure 2.11 Li_2O_2 formation on Fe/N/C catalyst and the discharge-charge cycle of Fe/N/C composite compared with MnO_2 catalyst. [72]

Additionally, the transition metal based catalyst also helps to reduce the cost for the catalyst. Recently, alloys of transition metals and noble metals were also applied as catalyst for Li-O_2 batteries, including PtCu [53], PtCo[74], and PtNi[73].

(c4) Transition metal oxides

Since the Bruce group reported their work on α-MnO_2 [11], much attention has been paid to single oxides (M_xO_y, where M is a transition metal). α-MnO_2 gives the lowest charge potential of 3.5 V among the other oxides, such as α-MnO_2, CuO, NiO, and Co_3O. A report from the Bruce group also recommended Co_3O_4 as a good catalyst that offers the best compromise between the initial capacity and capacity retention [28]. In addition to the single oxide, two element transition metal oxides ($M_xN_yO_z$) were predicted to give good OER performance [75].

$M_xN_yO_z$ oxides such as $NiCo_2O_4$ [58] and $LaNiO_3$ (LNO) [38] serve as cost effective materials for Li-O_2 batteries. **Figure 2.12** shows LNO performance compared to carbon material with lower charge overpotential, but the discharge terminal voltage is reduced to 2 V after the 24th cycle, with capacity limited to 1000 mAh g^{-1}. In 2014, the Goodenough group reported Mg doped $LaNi_{1-x}Mg_xO_3$ as a bifunctional catalyst for lithium air batteries [76]. As a cathode catalyst, LNO is an inexpensive choice comparing to noble metals such as Pt and Au. The partial replacement of Ni element in LNO was also reported to enhance the catalyst performance.

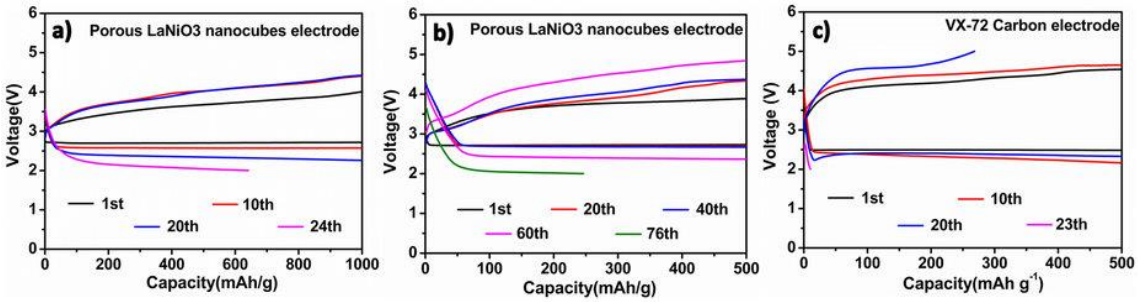

Figure 2.12 (a), (b) Cycling performance of porous $LaNiO_3$ nanocube electrode at 0.08 mA cm^{-2} with limited capacity of 1000 mAh $g^{-1}$and 500 mAh g^{-1}, respectively; (c) Cycling performance of VX-72 carbon electrode at 0.08 mA cm^{-2} with limited capacity of 500 mAh g^{-1}. [38]

2.1.6 Anode

The anode of Li-O_2 batteries is generally pure lithium metal. There are few works, however, that reported the application of lithiated silicon, Li_xSi [77], and lithiated Al-carbon [78]. Because of the high reactivity of Li metal, the Li needs to be protected. **Figure 2.13** shows architecture of a non-aqueous Li-O_2 battery [37a]. In this configuration, the Li metal is in contact with the non-aqueous electrolyte, reacts with the electrolyte, and forms a stable solid-electrolyte interphase (SEI). Due to its simplicity and rechargeability, the non-aqueous architecture is the most widely used system.

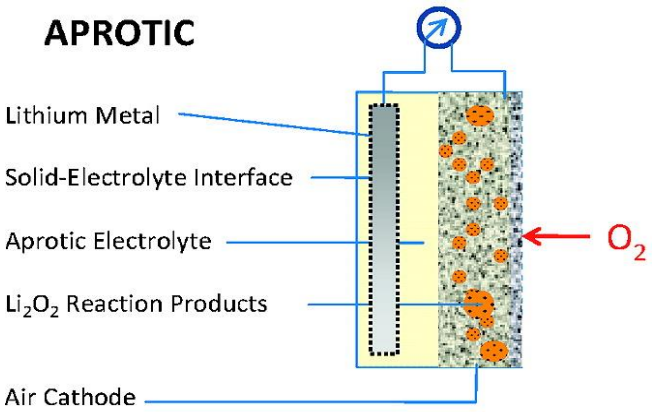

Figure 3.13 Architecture of non-aqueous (aprotic) Li-O_2 battery, which assumes the use of lithium metal as the anode. Spontaneously occurring SEIs on the lithium anode are indicated by dashed lines. [37a]

Dendritic lithium formation and the electrochemical instability of a lithium metal electrode remain significant challenges that must be overcome to allow the operation of Li-O_2 batteries. There are several ways to reduce the dendrite formation such as addition of additive in electrolyte. As shown in Figure 2.14, the sharp Li can be avoided by introducing 0.05 M $CsPF_6$. [37b] The additive in this work acts as an electrostatic shield which prevent further Li accumulation at sharp edges on Li metal surface.

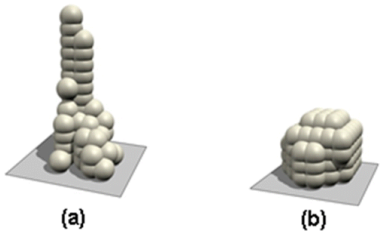

Figure 4.14 Simulated Li deposition onto a flat electrode surface from (a) 1 M $LiPF_6$ solution in PC and (b) from 1 M $LiPF_6$ + 0.05 M $CsPF_6$ solution in PC. [37b]

Additionally, it was reported that high Li salt concentration could suppress dendrite formation. The use of highly concentrated electrolytes (Figure 2.15 c,d) composed of ether solvents and the LiFSI salt enables the high-rate cycling of a lithium metal anode at high Coulombic efficiency (up to 99.1%) without dendrite growth. [37c]

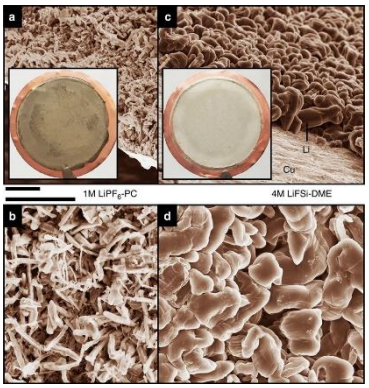

Figure 2.15 SEM images of the morphologies of Li metal after plating on Cu substrates in different electrolytes. (**a**,**b**) 1 M $LiPF_6$-PC. (**c**,**d**) 4 M LiFSI-DME. The current density was 1.0 mA cm^{-2} and the deposition time was 1.5 h. The diameter of the Cu substrate shown in the insert of (**a**,**c**) was 2 cm. Scale bar, 10 μm. [37c]

Another approach to mitigate the dendrite issue is covering the Li surface with a protective layer before cycling. This should be a strong physical barrier against dendrite propagation. It

is shown in Figure 2.16 that a thin Li_3PO_4 layer on Li with the good Li-ion conductivity and high Young's modulus mechanical properties exhibited a smooth, compact interface without obvious dendrites after 200 cycles. [37d]

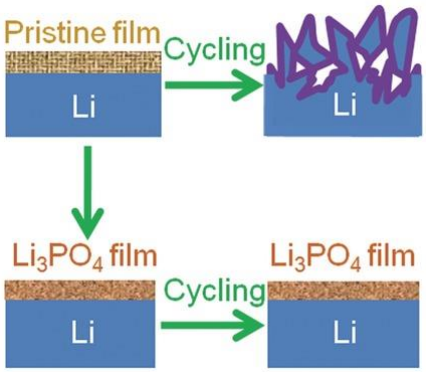

Figure 2.16 Schematics of the different Li anode structures. [37d]

In conclusion, after analysing a few cases, the dendrite formation can be reduced by using additives, high Li salt concentration, protective layer, and so forth.

2.1.7 Non-aqueous electrolytes:

(a) Electrolyte decomposition

Because of the similarity of the Li-O_2 cell to the lithium-ion battery cell, the first idea was to apply the electrolytes used of lithium ion batteries for Li-O_2 batteries. In Figure **2.17**, 1 M $LiPF_6$ in propylene carbonate (PC) electrolyte was used under O_2 [79]. Upon cycling, the formation of other products such as Li acetate, formate, and carbonate was observed between 6 and 30 cycles. The decomposition of PC electrolyte was proposed to explain the presence of Li acetate, formate, and carbonate. These by-products are unwanted, and they may reduce the performance of batteries.

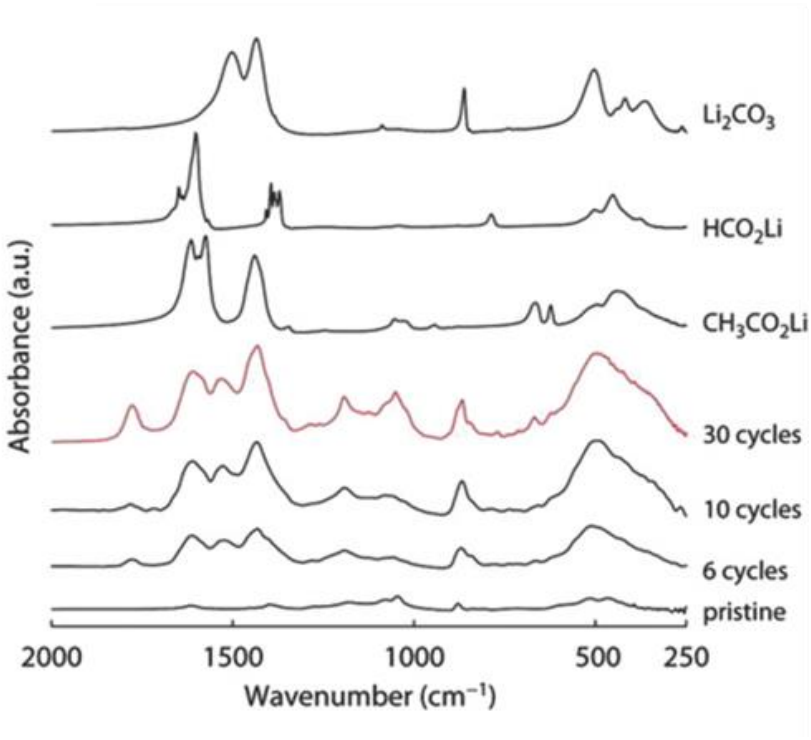

Figure 2.17 Fourier transform infrared (FTIR) spectra of composite electrodes containing the pristine material and electrodes after the indicated number of cycles between 2 and 4.2 V at the end of charge. Spectra of Li acetate, formate, and carbonate are shown for comparison. [79]

(b) Various types of non-aqueous electrolytes

Normally, researchers prefer to have stable electrolytes that do not decompose during cycling. Many types of electrolyte have been applied for Li-air batteries including carbonate-based electrolytes [79-86], ether-based electrolytes [87-93], dimethylsulfoxide (DMSO) electrolyte [94-97], ionic liquids [98-106], acetonitrile electrolytes [107-119], amide-based electrolytes [120-122], solid polymer electrolytes [123-124], and solid glass-ceramic electrolytes [125-126]. Among these electrolytes, ionic liquids have the advantage of stability at high charging voltages.

2.1.8 Redox mediators

Additives or redox mediators (RMs) can be used to enhance the performance of the discharge or charge process. In Figure 2.18, the discharge voltage can be improved significantly by adding K^+ additive to the electrolyte. The presence of RM (K^+ additive) in the electrolyte can

enhance the morphology of the discharge products (Figure 2.18). It is shown in Figure 2.18 that the discharge voltage is increased significantly with the addition of potassium trifluoromethanesulfonate (KOTf).

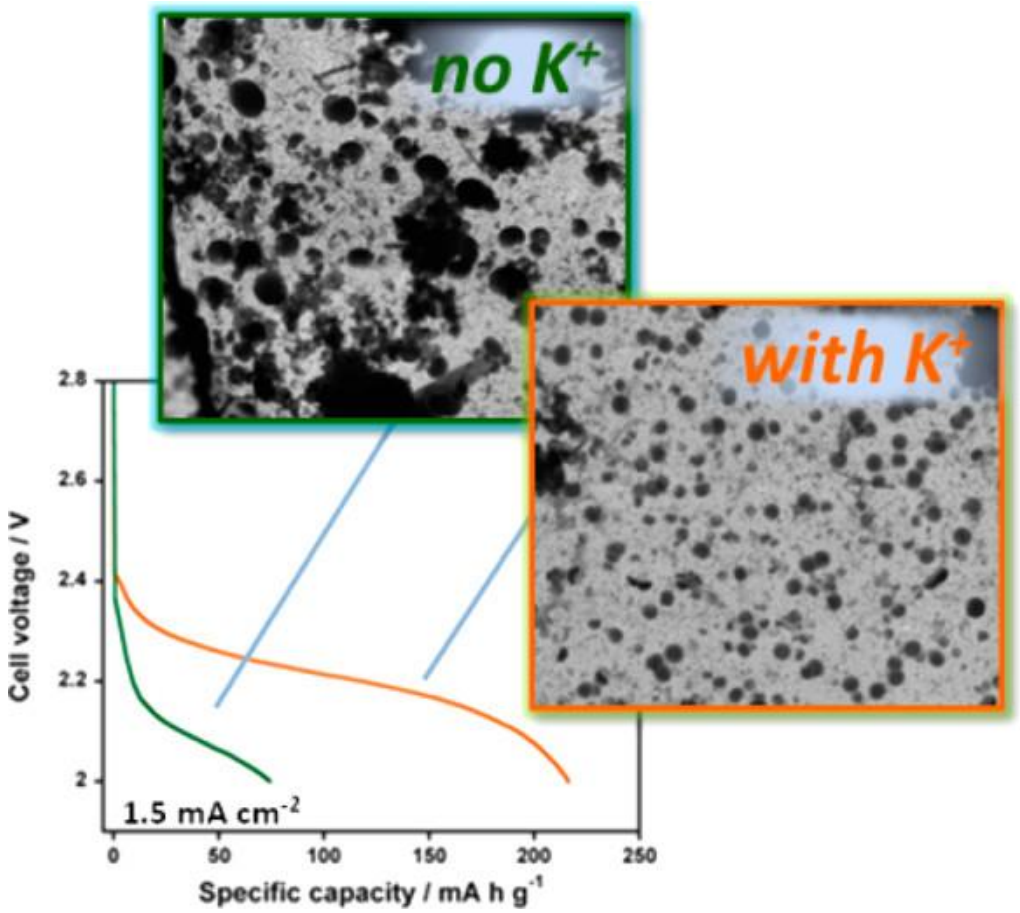

Figure 2.18 The first discharge curves of batteries with and without K^+ additive in the electrolyte with the corresponding Transmission electron microscope (TEM) images of the discharge products. [127]

2, 5-Di-tert-butyl-1, 4-benzoquinone (DBBQ) was also reported as an additive or mediator for the discharge process.[128] In the charge process, the charge voltage could be reduced by introducing 2, 2, 6, 6-tetramethyl-1-piperidinyloxy (TEMPO) [128], tetrathiafulvalene (TTF) [129], tris[4-(diethylamino)phenyl]amine (TDPA) [130], $LiNO_3$ [131], LiBr [132], and InI_3 [133] into the electrolyte. Several other RMs are listed by Lim et al. [134] RM is currently a hot topic, and it could significantly enhance the performance of the Li-O_2 battery.

2.2 Zinc-air batteries

(a) Alkaline electrolyte with water loss and zinc corrosion issues

Among all the MABs, the primary Zn-air battery is the only commercialized product, and alkaline solution is the electrolyte for it. [135,136] The primary Zn-air is successful because of its excellent discharge process, which is linked to the oxygen reduction reaction (ORR). In order to make a secondary Zn-air battery successful, it is necessary to design a good charge process that is governed by the oxygen evolution reaction (OER) and the complex structure of the whole battery. This review is focused on the problems of alkaline electrolytes. As a result, the best way to design the electrolyte for rechargeable Zn-air batteries can be found. Firstly, the alkaline electrolyte has the problem of water loss, and it requires the regular top up or replacement of electrolyte. [137] Secondly, the Zn anode is corroded in alkaline electrolyte. As shown in **Figure 2.19**d and Figure 2.19e, it is necessary to replace the electrolyte and zinc foil.

(b) Alkaline polymer electrolyte

In order to solve the water loss issue, polymer was added to the highly alkaline solution to form an alkaline polymer electrolyte such as hydroponics gel [138,139], polyvinyl alcohol (PVA), polymer matrix [140-141], or Sago gel polymer electrolyte [142].

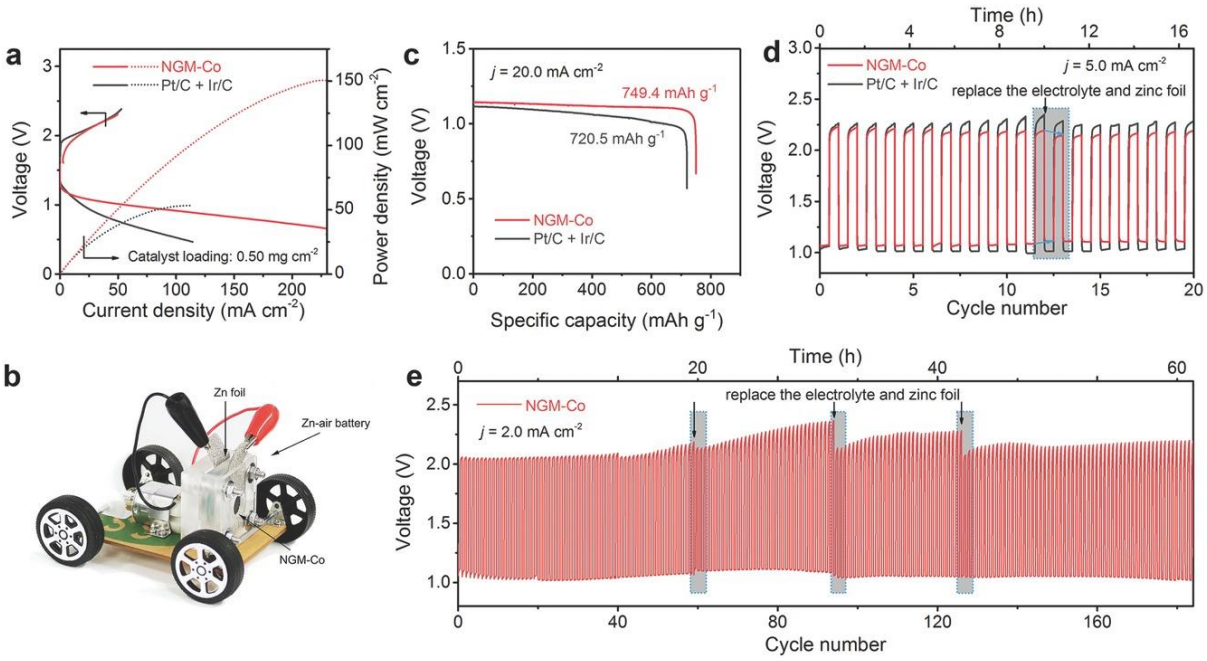

Figure 2.19 Application of hierarchical Co/N/O tri-doped graphene catalyst (NGM-Co) in rechargeable liquid Zn-air batteries. a) Charge and discharge polarization curves. b) Photograph of a toy car powered by one Zn-air battery based on NGM-Co catalyst. c) Discharge curves of Zn-air batteries assembled with the NGM-Co and Pt/C + Ir/C catalysts at 20.0 mA cm^{-2} discharging rate. d) Galvanostatic discharge–charge cycling curves at 5.0 mA cm^{-2} of the rechargeable Zn-air batteries. e) Long-term cycling test at 2.0 mA cm^{-2}. The electrolyte and zinc foil were replaced for a subsequent cycling as indicated by the arrows in (d) and (e). [137]

Figure 2.20 shows cyclic voltammograms (CVs) in the −1.5 to +1.5 V range for polyethylene oxide (PEO)–PVA polymer electrolyte and two types of separators (PP/PE and cellulose). It is clearly that the polyethylene (PE)/polypropylene (PP) and cellulose separators have much narrower electrochemical stability windows than PEO–PVA, as shown in Figure 2.20. The electrochemical stability obviously makes PEO-PVA a strong candidate for Zn-air batteries.

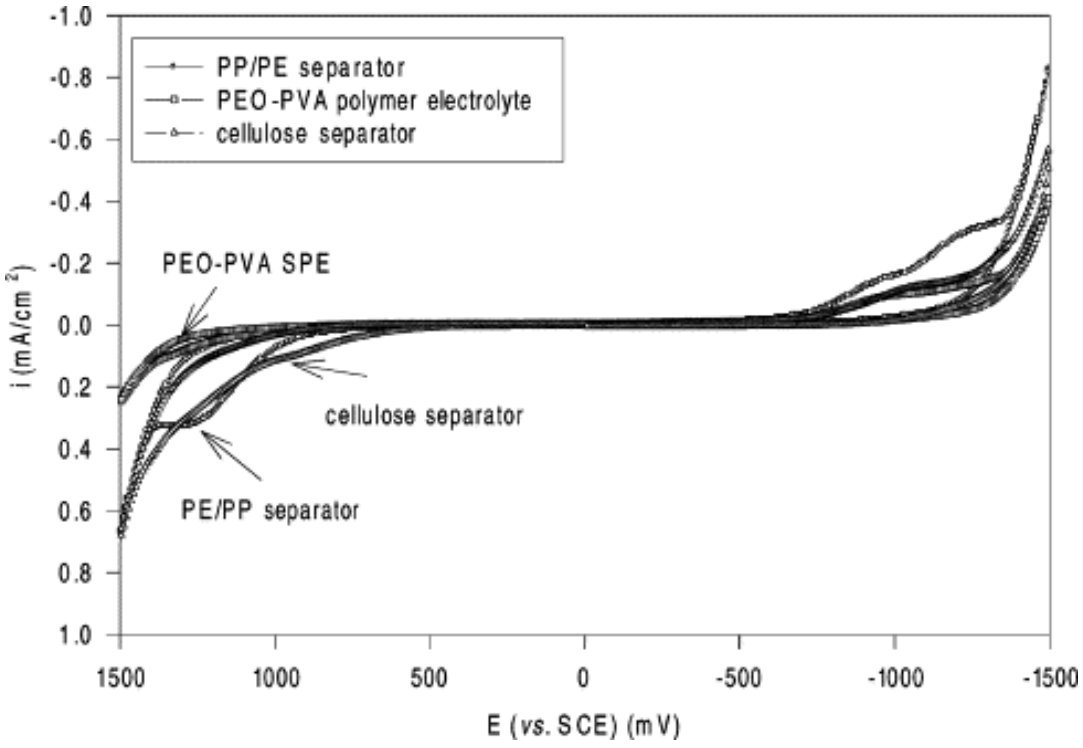

Figure 2.20 Cyclic voltammograms of composite PEO–PVA polymer electrolyte film, with PE/PP and cellulose separators at scan rate of 1 mV/s at 25°C. [140] SCE: saturated calomel electrode.

(c) Neutral electrolyte, PEG, and dendrite suppression

A type of neutral electrolyte was developed for rechargeable zinc-air battery application. [143-145] Rechargeable zinc-air battery tests in Goh et al.'s group [143] showed that such a battery with neutral electrolyte could last up to 1000 hours over hundreds of discharge-charge cycles, with discharge-charge capacity ranging from 20 to 120 mAh/g. No zinc dendrites were formed during the long battery test. As shown in Figure **2.21**c, Figure 2.21d, Figure 2.21g, and Figure 2.21h, significant suppression of dendrite growth could be obtained with polyethylene glycol (PEG) concentrations of 1000 and 10000 ppm.

Based on the literature review, this PhD work was focused on the study of electrocatalysts for metal air batteries, in particular the two systems represented by the Li-O_2 battery and the rechargeable zinc air battery. The metal oxide $LaNiCuO_3$ and nanoparticles of Pt_3Cu on an

array of TiN nanorods were applied as catalysts for the Li-O_2 battery. In the case of the rechargeable zinc air battery, a film of Ni_3Pt catalyst [prepared by pulsed laser deposition (PLD)] on Ni foam was used as air cathode for the battery.

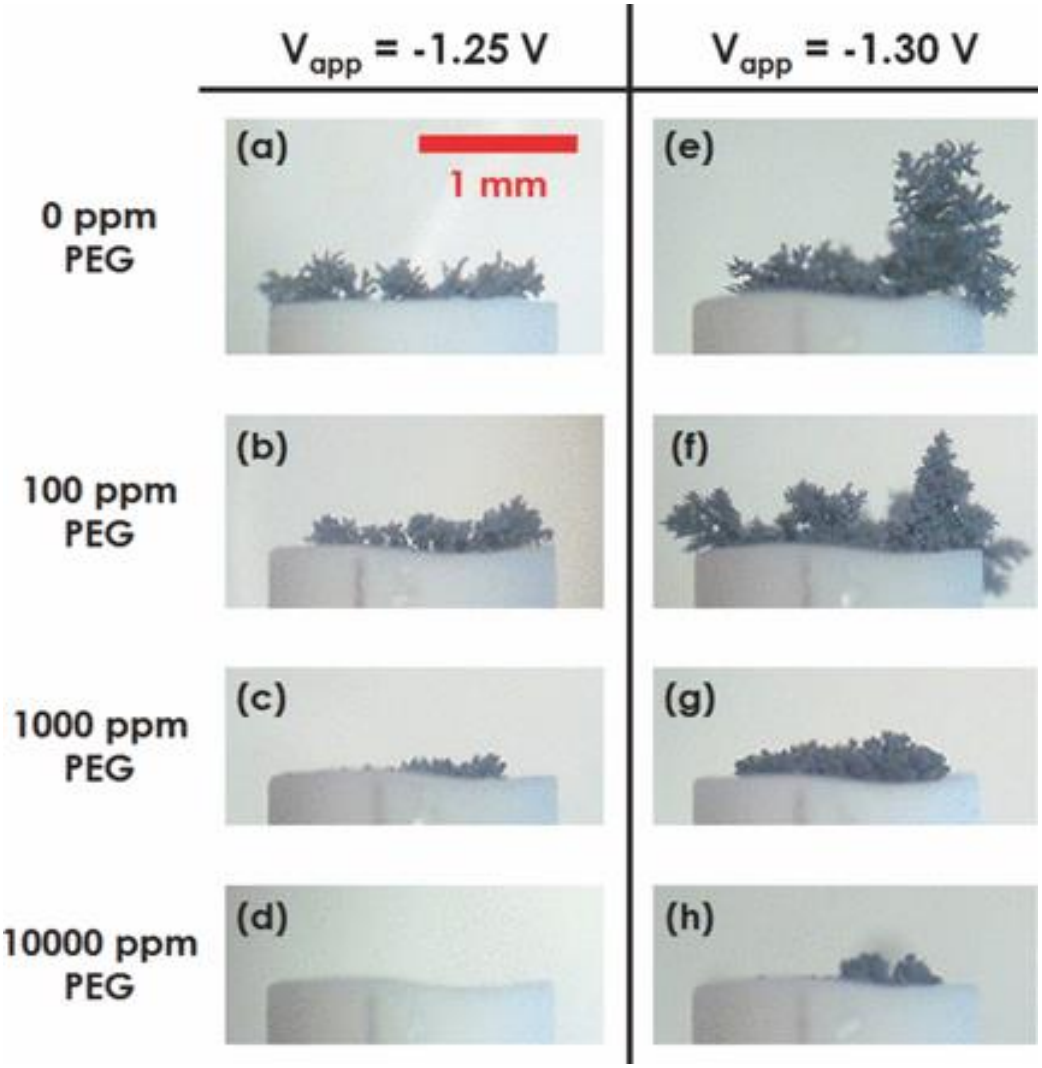

Figure 2.21 Optical microscope images of Zn dendrites protruding from the tip of a polyvinyl chloride (PVC)-coated wire electrode on which Zn was electrodeposited potentiostatically for 8 minutes. The electrolyte contains 0.1 M $ZnCl_2$ with various concentrations of PEG: 0 ppm [(a) and (e)], 100 ppm [(b) and (f)], 1000 ppm [(c) and (g)], and 10000 ppm [(d) and (h)]. Two operating voltages are compared: –1.25 V vs. Ag/AgCl [(a)–(d)] and –1.30 V vs. Ag/AgCl [(e)–(h)]. [146]

Chapter 3 Experiment

3.1 List of materials and chemicals

All of the chemicals and materials were purchased from Sigma Aldrich, and the chemicals are listed in Table 3.1.

Table 3.1 Details of materials used in this PhD study.

Materials/Chemicals	**Chemical formulae**	**Purity (%)**	**Supplier**
Acetone	CH_3COCH_3	≥99.5	Sigma-Aldrich
Ammonia solution	NH_3	28-30	Merck
Argon gas	Ar	99.9	BOC
Carbon black	C		Timcal, Belgium
Cobalt (II) nitrate hexahydrate	$Co(NO_3)_2 \cdot 6H_2O$	98.5	Sigma-Aldrich
Copper (II) nitrate trihydrate	$Cu(NO_3)_2 \cdot 3H_2O$	≥99	Sigma-Aldrich
Ethanol	C_2H_5O	Reagent	Q-Store Australia
Ethylene glycol	$HOCH_2CH_2OH$	99.8	Sigma-Aldrich
Isopropanol	$(CH_3)_2CHOH$		Sigma-Aldrich
Lanthanum (III) nitrate hexahydrate	$La(NO_3)_3 \cdot 6H_2O$	99.999	Sigma-Aldrich
Lithium trifluoromethanesulfonate	$LiCF_3SO_3$	99.995	Sigma-Aldrich
Nafion®		5% in water	Sigma-Aldrich

Nitric acid	HNO_3	70	Sigma-Aldrich
Nickel (II) nitrate hexahydrate	$Ni(NO_3)_2 \cdot 6H_2O$	98.5	Sigma-Aldrich
Poly(vinyl alcohol)			Sigma-Aldrich
Potassium hydroxide	KOH	90	Sigma-Aldrich
Tetraethylene glycol dimethyl ether	$CH_3O(CH_2CH_2O)_4CH_3$	>99.0	Sigma-Aldrich
Zinc acetate dihydrate	$Zn(O_2CCH_3)_2 \cdot 2H_2O$	99.999	Sigma-Aldrich

3.2 Experimental procedures

The experimental procedures in this thesis can be divided into five parts, including materials synthesis, physical characterization, electrocatalytic characterization, electrode preparation and CR2032 type coin-cell (with holes) assembly, and electrochemical characterization.

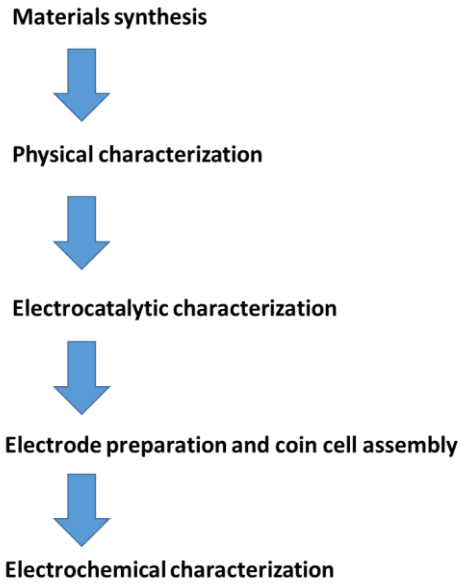

Figure 3.1 Outline of procedures and techniques used in this thesis.

3.3 Materials synthesis

In this PhD study, electrocatalysts were prepared by several methods. The details on each method can be found in the next sections.

3.3.1 Pulsed laser deposition

Pulsed laser deposition (PLD) is a physical vapour deposition (PVD) technique where a high-power pulsed laser beam is focused inside a vacuum chamber to strike a target of the material that is to be deposited. This material is vaporized from the target and is deposited as a thin film on a substrate (such as a silicon wafer facing the target). This process can occur in ultra-high vacuum or in the presence of a background gas. In this study, catalyst materials (Pt alloy materials) were deposited on nickel foam substrate in a PLD system.

Figure 3.2 PLD450 system containing a high vacuum chamber.

3.3.2 Hydrothermal synthesis

Hydrothermal synthesis can be used to produce several oxide materials at high temperature in an enclosed and pressurized environment. It can be defined as a method for producing single

crystals that depends on the solubility of minerals in hot water under high pressure. The advantages of the hydrothermal method over other types of crystal growth include the ability to create crystalline phases that are not stable at their melting points. In addition, materials that have a high vapour pressure near their melting points can also be grown by the hydrothermal method. This method is also particularly suitable for the growth of large good-quality crystals while maintaining good control over their composition.

The crystallization vessels that are used are called autoclaves. These are usually thick-walled steel cylinders with a hermetic seal that must be able to withstand high temperatures and pressures for prolonged periods of time. Furthermore, the autoclave material must be inert with respect to the solvent. The closure is the most important element of the autoclave. In most cases, steel-corroding solutions are used in hydrothermal experiments. To prevent corrosion of the internal cavity of the autoclave, protective inserts are generally used. These may have the same shape as the autoclave and fit into the internal cavity (contact-type insert). The hydrothermal autoclaves used in this PhD thesis work are 4748 acid digestion bombs with 125 ml capacity from the Parr Instrument Company, as is shown in **Figure 3.3**. The outer parts are made of stainless steel with six cap screws to seal the polytetrafluoroethylene (PTFE) liner. The temperature can reach as high as 250 ºC, and the pressure can reach as high as 1900 psi. In typical experiments, the precursor solution was transferred to the PTFE liner, and the autoclave was then kept in a conventional oven for the preset time and temperature.

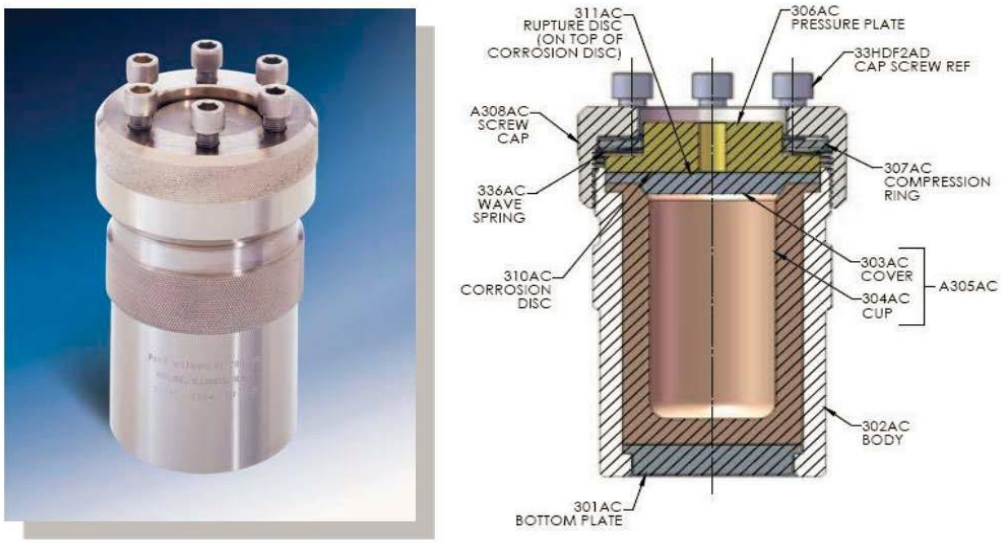

Figure 3.3 Acid digestion bomb 4748 from Parr Instruments (left) with a cross-sectional view (right).

3.4 Structural and physical characterization

Physical characterization was used to identify the phases of materials, their morphology, and the porosity of catalyst materials. The purpose of these tests was to find materials with high surface area as well as characterizing the physical properties of materials. The equipment used in this study belongs to the Institute for Superconducting and Electronic Materials (ISEM) and the Intelligent Polymer Research Institute (IPRI) at the Australian Institute for Innovative Materials (AIIM).

3.4.1 X-ray diffraction (XRD)

XRD is a technique used for determining the atomic and molecular structure of a crystal, in which the crystalline structure causes a beam of incident X-rays to diffract into many specific directions. The XRD technique in this PhD study was used to determine if the materials were in the correct phase as well as the degree of crystallinity of active materials.

In this doctoral work, X-ray diffraction measurements were carried out using a scanning mode with a copper Kα radiation source. The diffractometers used were a GBC MMA (**Figure 3.4**) and a Rigaku SA-HFM3. The systems were interfaced with Visual XRD and Traces software for graphical processing and data manipulation. The sample powders and were dropped with ethanol onto glass slides and left it to dry.

Figure 3.4 GBC MMA XRD system.

3.4.2 Field emission scanning electron microscopy (FESEM) and energy dispersive spectroscopy (EDS)

The FESEM technique was used to identify the morphology of the materials in this study. The EDS technique is useful to find out which elements are present in materials. In this PhD work, a JEOL JSM-7500FA field-emission scanning electron microscope (FESEM) and an attached EDS analysis facility were used.

The JEOL JSM-7500FA is a 30 kV semi in-lens cold field emission gun – scanning electron microscope capable of 1.4 nm spatial resolution. It is well suited for the characterization of insulating materials and nanomaterials, and of medical and biological samples. The beam irradiation technique provides exceptional image quality at acceleration voltages as low as 0.1 kV. This reduces charging effects in uncoated insulating materials and beam damage in

electron-sensitive materials. The transmitted electron detector can attain a resolution of 0.6 nm at 30 kV and is suitable for imaging thin foils or nanosized materials on thin support films.

3.4.3 Transmission electron microscopy (TEM)

Transmission electron microscopy (TEM) is a microscopy technique in which a beam of electrons is transmitted through an ultra-thin specimen, interacting with the specimen as it passes through. In this PhD study, TEM was used to identify the crystal structure and the morphology at high magnification. Defects in the crystal structure can be investigated in the high resolution TEM mode. TEM images were collected using a JEOL 2011 200 keV transmission electron microscope, with a JEOL energy-dispersive X-ray spectroscopy (EDS) detector and a JEOL EDS software analysis system.

3.4.4 Atomic resolution analytical microscope (ARM)

The JEOL JEM-ARM200F is a 200 kV probe corrected scanning transmission electron microscope (STEM) capable of atomic resolution imaging. At 200 kV, the microscope features a resolution of < 0.08 nm, while at 80 kV, a resolution of < 0.14 nm is possible.

The microscope features a large area silicon drift detector (SDD) EDS detector that allows elemental mapping with atomic resolution. Moreover, the microscope is equipped with a cold field emission gun with a resolution of 0.3 eV, which, when coupled with the GIF Quantum

imaging filter, enables not only elemental analysis at the atomic level, but also determination of the electronic structure; i.e., oxidation state, chemical bonding, and surface plasmons.

Figure 3.5 JEOL JEM-ARM200F atomic resolution analytical microscope.

3.4.5 X-ray photoelectron spectroscopy (XPS)

X-ray photoelectron spectroscopy (XPS) is a surface-sensitive quantitative spectroscopic technique that measures the elemental composition in the parts per thousand range and can determine the empirical formula, chemical state, and electronic state of the elements that exist within a material. XPS spectra are obtained by irradiating a material with a beam of X-rays while simultaneously measuring the kinetic energy and number of electrons that escape from the top 0 to 10 nm of the material being analysed. XPS requires a high vacuum (P ~ 10 - 8 millibar) or ultra-high vacuum conditions, although a current area of development is ambient-pressure XPS, in which samples are analysed at pressures of a few tens of millibars. It is a

surface chemical analysis technique that can be used to analyse: (i) the surface chemistry of a material in its as-received state or after some treatment; (ii) the empirical formula of pure materials; (iii) the elements that contaminate a surface; (iv) the chemical or electronic state of each element in the surface; (v) the uniformity of the elemental composition across the top surface; and (vi) the uniformity of the elemental composition as a function of ion beam etching. XPS experiments in this thesis were carried out on a VG Scientific ESCALAB 2201 XL instrument using aluminum Kα X-ray radiation. XPS spectral analysis was conducted using XPS Peak-fit software.

3.4.6 Brunauer-Emmett-Teller (BET) measurements

The well-known Brunauer-Emmett-Teller measurements are based on the theory of physical adsorption of gas molecules on a solid surface and serves as an important analysis technique for the measurement of the specific surface area of a material. The analysis is carried out at liquid nitrogen temperature (77 K) over many relative pressures. The samples have to be kept dry at 100 ºC overnight and degassed before analysis to provide more accurate results. In this study, the BET measurements were conducted on a Quantachrome Nova 1000 nitrogen gas analyser, and an Autosorb-iQ-Cx nitrogen adsorption instrument was used to determine the specific surface area of the synthesized powders.

3.5 Electrocatalytic characterization

The electrocatalytic tests were used to compare the catalytic activity of the active materials with other standard ORR and OER materials, such as Pt/C commercial catalyst for the ORR and IrO_2 for the OER. The electrocatalytic test is a procedure to find out if a material is an excellent catalyst.

Rotating disk electrode (RDE)

The rotating disk electrode (RDE) is a hydrodynamic working electrode used in a three-electrode system. The electrode rotates during experiments, inducing a flux of analyte to the electrode. These working electrodes are used in electrochemical studies when investigating reaction mechanisms related to redox chemistry. The electrode includes a conductive disk embedded in an inert nonconductive polymer or resin that can be attached to an electric motor that has very fine control of the electrode's rotation rate. The disk, like any working electrode, is generally made of a noble metal or glassy carbon (as shown in Fig. 3.6).

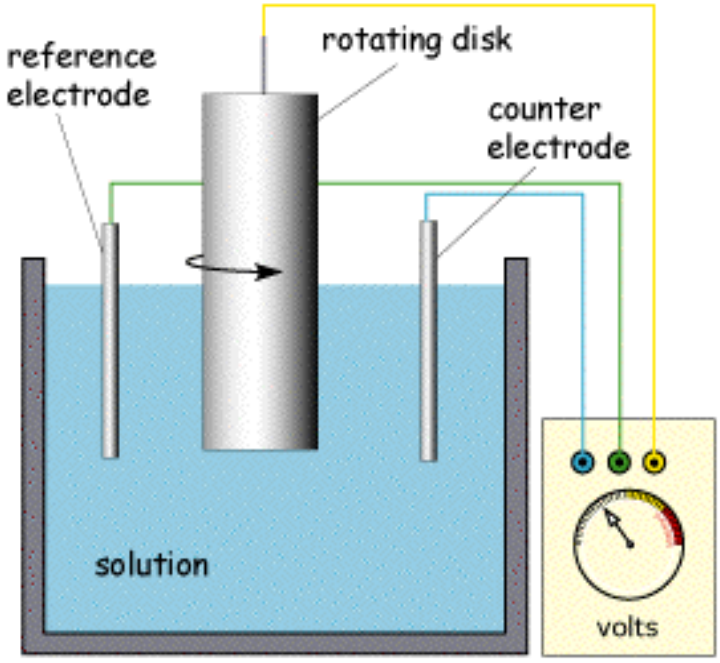

Figure 3.6 Schematic illustration of the rotating disk electrode.

This disk's rotation is usually described in terms of angular velocity. As the disk turns, some of the solution is dragged along by the spinning disk, and the resulting centrifugal force flings the solution away from the centre of the electrode. The solution flows up, perpendicular to the electrode, from the bulk to replace the boundary layer. The sum result is laminar flow of the

solution towards and across the electrode. The rate of the solution flow can be controlled by the electrode's angular velocity and modelled mathematically. This flow can quickly achieve conditions in which the steady-state current is controlled by the solution flow rather than diffusion. By running RDE, different electrochemical phenomena can be investigated, including multi-electron transfer, the kinetics of slow electron transfer, adsorption/desorption steps, and electrochemical reaction mechanisms. In this work, the aqueous electrochemical tests involving the RDE were carried out using computer-controlled potentiostats (Princeton 2273 and 616 Princeton Applied Research) with a typical three-electrode cell. Platinum foil was used as the counter-electrode and an Ag/AgCl (saturated KCl filled) electrode as the reference electrode. The working electrodes were prepared by applying the respective catalyst onto pre-polished glassy carbon (GC) disk electrodes.

3.6 Electrode preparation and coin-cell assembly technique

Electrochemical performances were tested using CR2032 type coin cells with holes in the cathode part. The working electrodes for Li-O_2 batteries were prepared by mixing the active materials with 10 % poly(tetrafluoroethylene) (PTFE) or 10 % poly(vinylidene difluoride) (PVDF) in a solvent, consisting of either Nafion® (5 %) or 1-methyl-2-pyrrolidinone (NMP), respectively. The slurry was uniformly pasted onto glass microfiber filters, which are used for the separator, or onto stainless steel mesh in combination with Nafion® (5 %) as solvent and polypropylene as separator. The typical loading of cathode powder on a 1x1 cm^2 electrode was 1-2 mg cm^{-2}, depending on the density of the electrochemically active samples. The electrolyte consisted of a solution of 1 M $LiPF_6$ in tetraethylene glycol dimethyl ether (TEGDME), or 1 M $LiCF_3SO_3$ in TEGDME. Pure lithium-foil was used as the counter electrode. The cells were assembled in an argon-filled glove box (Mbraun, Unilab, Germany). In a typical assembly, 2-3

drops of electrolyte is enough to soak the electrode and separator. The negative cap was stacked on after the spring and the assembly were crimped to ensure air-tight sealing. Every measurement was repeated at least three times to ensure reliability.

3.7 Electrochemical characterization

3.7.1 Cyclic voltammetry (CV)

Cyclic voltammetry (CV) is an electrochemical technique to measure the current that is developed in an electrochemical cell under conditions where the voltage is in excess of that predicted by the Nernst equation. CV is performed by cycling the potential of a working electrode and measuring the resulting current. In a cyclic voltammetry experiment, the working electrode potential is ramped linearly versus time. After the set potential is reached in a CV experiment, the working electrode's potential is ramped in the opposite direction to return to the initial potential. If a redox reaction is present in the electrochemical reaction, a distinct peak can be observed in both the forward and the reverse scans. In this work, the CV data were collected on Princeton 2273 and 636 instruments, Princeton Applied Research, or on an Arbin BT2000.

3.7.2 Galvanostatic charge and discharge

The capacity and cycling performance of the Li-O_2 batteries were investigated by galvanostatic charge-discharge testing at various current densities. The charge or discharge capacity (Q) equals the total electron charge in each process, and it can be calculated from the recorded current and the time: $Q = I \times t$. All tests were carried out on a Land CT 2001. Multi-channel battery testers were used at room temperature in oxygen atmosphere.

3.7.3 Linear sweep voltammetry (LSV)

Linear sweep voltammetry is a voltammetric method, in which the current at a working electrode is measured while the potential between the working electrode and a reference electrode is swept linearly in time. Linear sweep voltammetry can identify unknown species, while the height of the limiting current can determine the concentration. LSVs were collected on a PARSTAT 2273 Princeton Applied Research or Arbin BT 2000 workstation.

Chapter 4 Carbon-and Binder-free 3D porous perovskite oxide air electrode for rechargeable lithium-oxygen battery

4.1 Introduction

The lithium-oxygen battery has attracted much attention due to its ultrahigh theoretical energy density. This system is still far from practical application, however, due to its low efficiency and poor cycling performance, at least at present. [147-149] The key approach to addressing these issues is to design an appropriate porous air electrode structure accommodating reaction product formation, along with a bifunctional electrocatalyst that features high activity towards the oxygen reduction reaction (ORR) and the oxygen evolution reaction (OER).[150-154] Generally, the air electrode includes a porous structured electrocatalyst with electronically conductive carbon black and binder. The common utilization of carbon-based materials and binder is accompanied by fatal instability problems, however, with the cathode suffering nucleophilic attack of highly-sensitive intermediate radicals and decomposition to LiF, LiOH, and Li_2CO_3. [155] These additional products are mostly irreversible and unexpected, and they have a

detrimental influence on the electrochemical performance, resulting in especially low round-trip efficiency and poor cycling performance. Additionally, both carbon and non-aqueous electrolytes for Li–O_2 batteries are hydrophobic. Due to the low surface tension between the carbon material and the electrolyte, the electrolyte tends to wet all the catalyst surfaces, which restricts oxygen diffusion in the air electrodes.[156] In order to avoid the above problems, much more attention is being devoted to developing an appropriate air electrode, such as by using stable metal-based substrates, such as nickel foam or titanium mesh, as catalyst substrates. These metal substrates can offer stable, conductive, three-dimensional (3D) microporous structures which facilitate electrolyte flow and air diffusion. [157-159]

From the catalyst perspective, noble-metal-free ABO_3 perovskite oxides, in which A is traditionally from Group I-III and B is a transition-metal ion with six-fold octahedral coordination, are being spotlighted as cost-effective and efficient electrocatalyst candidates for the role of bifunctional catalyst, with electronic structures that are made sensitive to strain by doping with different elements. [160-162] The ORR and OER catalytic activities can be influenced dramatically by controlling the degree of eg orbital splitting and polarization in the octahedral structure through the strain induced by element substitution to yield changes in the orbital occupancy or polarization.[163-165] Meanwhile, oxygen vacancy, intrinsic to perovskite oxide, plays a pivotal role in catalytic activity enhancement by tuning the valence states of the B-site transition metal cations. [163]One perovskite oxide, $LaNiO_3$, is inherently sensitive to oxygen stoichiometry, and several groups have investigated the oxygen content dependence of its conductivity and optimized the catalytic activity by producing lattice strain and oxygen vacancy. [166-170] Two works about the role of oxygen vacancy in CoO were also reported recently. [171-172] In this work, the abundant lattice strains and oxygen vacancy were induced in this perovskite oxide by B-site element substitution, using elements with different ionic radius sizes and valence states, such as Cu^{2+}(73 pm) and Co^{3+}(60 pm). The perovskite oxide $LaNiO_3$

was reported as cathode catalyst for Li-O_2 battery. [38] The doping of Cu and Co at Ni-site are expected to create several defects. It was reported that the defects in graphene could enhance the Li_2O_2 formation process which improve the discharge process of Li-O_2 battery. [48] As a result, $LaNi_{0.9}M_{0.1}O_3$ (M = Cu, Co) perovskite oxides were grown on microporous nickel foam in the form of nanosheets and employed as novel complete air electrodes for the Li-O_2 battery. The design of this 3D porous air-electrode structure can provide a continuous conductive network and improve the adsorption of and immersion in electrolyte of the deposited porous nanosheets of perovskite oxide in order to facilitate the oxygen catalytic reaction kinetics for high-energy conversion.

4.2. Experimental

Preparation of $LaNi_{0.9}M_{0.1}O_3$ (M = Cu, Co) on Ni foam

$LaNi_{0.9}M_{0.1}O_3$ on Ni foam was synthesized by hydrothermal process.

$LaNiO_3$ on Ni foam: The amount of 1 mmol $La(NO_3)_3.6H_2O$, 1 mmol $Ni(NO_3)_2.6H_2O$ and 14 mmol KOH were dissolved in 45 mL of water. Ni foam was cut to circular shape with 1.9 cm diameter. Then, it was immersed in 6M HCl solution to remove any oxide surface layers. Afterwards, the Ni foam and the aqueous solution were transferred to a Teflon-lined stainless-steel autoclave, which was sealed and maintained at 160^{o}C for 8 h. Finally, the product was taken out, washed, vacuum dried and then thermally treated at 400^{o}C in nitrogen for 2 h. The mass loading of $LaNiO_3$ on Ni foam was calculated from the difference in weight between the pristine Ni foam and the $LaNiO_3$ coated foam.

$LaNi_{0.9}Cu_{0.1}O_3$ on Ni foam: The amount of 1 mmol $La(NO_3)_3.6H_2O$, 0.9 mmol $Ni(NO_3)_2.6H_2O$, 0.1 mmol of $Cu(NO_3)_2.3H_2O$ and 14 mmol KOH were dissolved in 45 mL of

water. The same process to clean Ni foam in HCl was applied. Ni foam and aqueous solution were kept in autoclave for 8h at 160^{o}C, followed by a annealing in N_2 atmosphere at 400^{o}C for 2h.

$LaNi_{0.9}Co_{0.1}O_3$ on Ni foam: The amount of 1 mmol $La(NO_3)_3.6H_2O$, 0.9 mmol $Ni(NO_3)_2.6H_2O$, 0.1 mmol of $Co(NO_3)_2.6H_2O$ and 14 mmol KOH were dissolved in 45 mL of water. The same process to clean Ni foam in HCl was applied. Ni foam and aqueous solution were kept in autoclave for 8h at 160^{o}C, followed by a annealing in N_2 atmosphere at 400^{o}C for 2h.

$LaNi_{0.9}Cu_{0.1}O_3$ powder: The amount of 1 mmol $La(NO_3)_3.6H_2O$, 0.9 mmol $Ni(NO_3)_2.6H_2O$, 0.1 mmol of $Cu(NO_3)_2.3H_2O$ and 14 mmol KOH were dissolved in 45 mL of water. The solution was transferred to Teflon-lined stainless-steel autoclave, which was sealed and maintained at 160^{o}C for 8 h. The powder was collected by centrifuged, then annealed in N_2 at 400^{o}C for 2h.

$LaNi_{0.9}Co_{0.1}O_3$ powder: The amount of 1 mmol $La(NO_3)_3.6H_2O$, 0.9 mmol $Ni(NO_3)_2.6H_2O$, 0.1 mmol of $Co(NO_3)_2.6H_2O$ and 14 mmol KOH were dissolved in 45 mL of water. The solution was transferred to Teflon-lined stainless-steel autoclave, which was sealed and maintained at 160^{o}C for 8 h. The powder was collected by centrifuged, then annealed in N_2 at 400^{o}C for 2h.

4.3 Results and discussion

4.3.1 Structure and morphology

All the $LaNi_{0.9}M_{0.1}O_3$ (M = Cu, Co) samples on nickel foam were synthesized via the hydrothermal method (please see Experimental section for more details). Field emission scanning electron microscopy (FESEM) was used to analyse the structure of the air electrode and the morphology of three different kinds of catalysts, $LaNiO_3$, $LaNi_{0.9}Cu_{0.1}O_3$, and $LaNi_{0.9}Co_{0.1}O_3$, which were grown on nickel foam, as shown in **Figure 4.1**. All the catalysts were grown uniformly on the surface of the 3D microporous nickel foam electrode and showed a nanosheet array structure. Among these three different catalysts, the thickness of the $LaNi_{0.9}Cu_{0.1}O_3$ nanosheets, in the range of 10 nm, is much less than for pure $LaNiO_3$ and $LaNi_{0.9}Co_{0.1}O_3$. The surface area of this perovskite structure was estimated by BET method at 30 $m^2 g^{-1}$. It was nearly 8 times as high as the reported value of the bulk $LaNiO_3$.[173] This whole 3D structured porous electrode with a large amount of nanosheet catalyst can also provide a large surface area and abundant highly efficient catalytic active sites for reaction product accommodation. Meanwhile, as a complete air electrode without any unstable carbon conductive additive or binder, this air electrode can also overcome the impedance increase that is due to the formation of interfacial Li_2CO_3 via the reaction of lithium peroxide with carbon or binder decomposition.

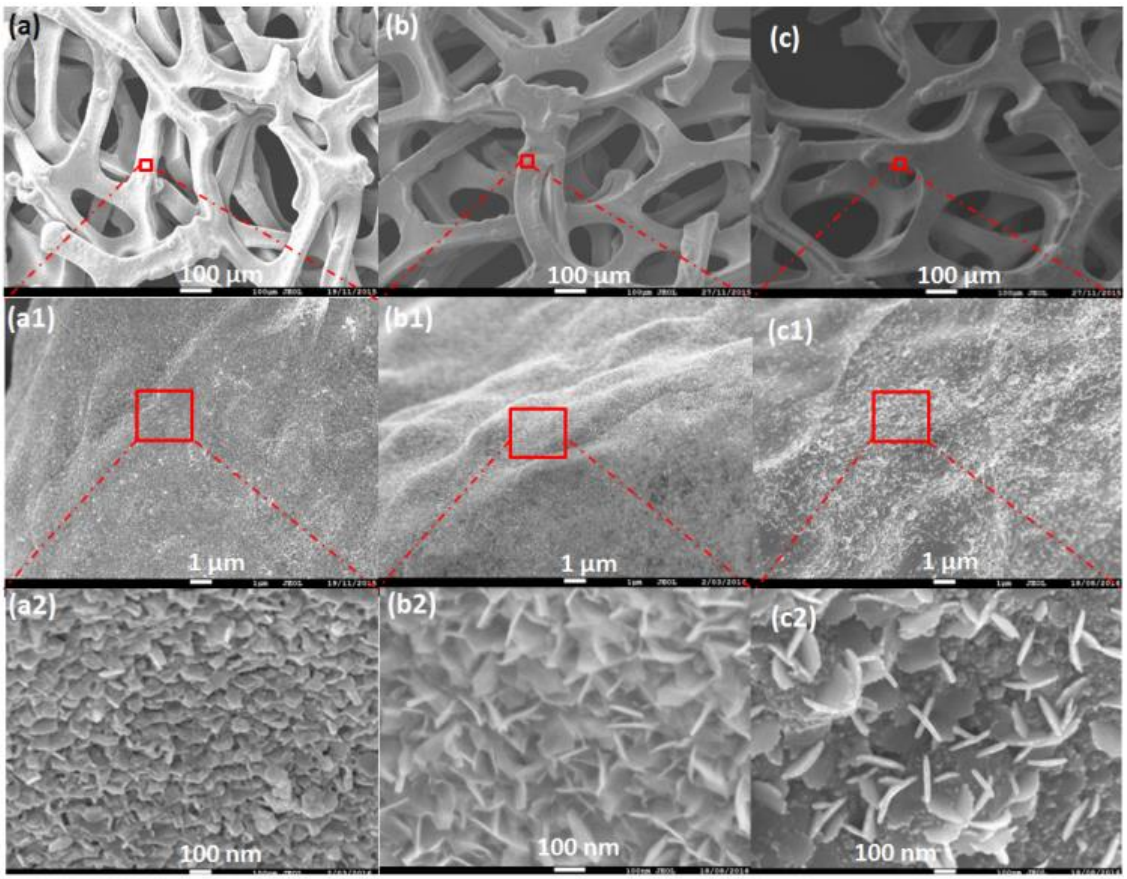

Figure 4.1 FESEM images at different magnifications of (a-a2) $LaNiO_3$, (b-b2) $LaNi_{0.9}Cu_{0.1}O_3$, (c-c2) $LaNi_{0.9}Co_{0.1}O_3$.

For structural characterization, the powder X-ray diffraction (XRD) patterns of the perovskites with partial substitution of Ni^{3+} by Co^{3+} and Cu^{2+} is presented in **Figure 4.2**. They show that all the samples can be indexed to the standard perovskite $LaNiO_3$ phase with hexagonal structure. There are obvious differences, however, in the peak intensity ratio between the (012) and (110) peaks, $I_{(012)}/I_{(110)}$. $LaNi_{0.9}Cu_{0.1}O_3$ shows the highest $I_{(012)}/I_{(110)}$ value, 0.92, while $LaNi_{0.9}Co_{0.1}O_3$ shows a lower ratio value, 0.54, slightly higher than that of pure $LaNiO_3$. According to some reported results,[174-176] compared to $LaNiO_3$ and $LaNi_{0.9}Co_{0.1}O_3$, there will be a small loss of oxygen in $LaNi_{0.9}Cu_{0.1}O_3$. Secondly, when Cu^{2+} was introduced into Ni^{3+} sites, an obvious left shift of the (110) and (012) peaks appeared in $LaNi_{0.9}Cu_{0.1}O_3$. The conclusion can be reached that the change in the

perovskite from the substitution for Ni^{3+} by Cu^{2+} with a different valence state results in an increase in the crystalline plate distance and oxygen vacancy.

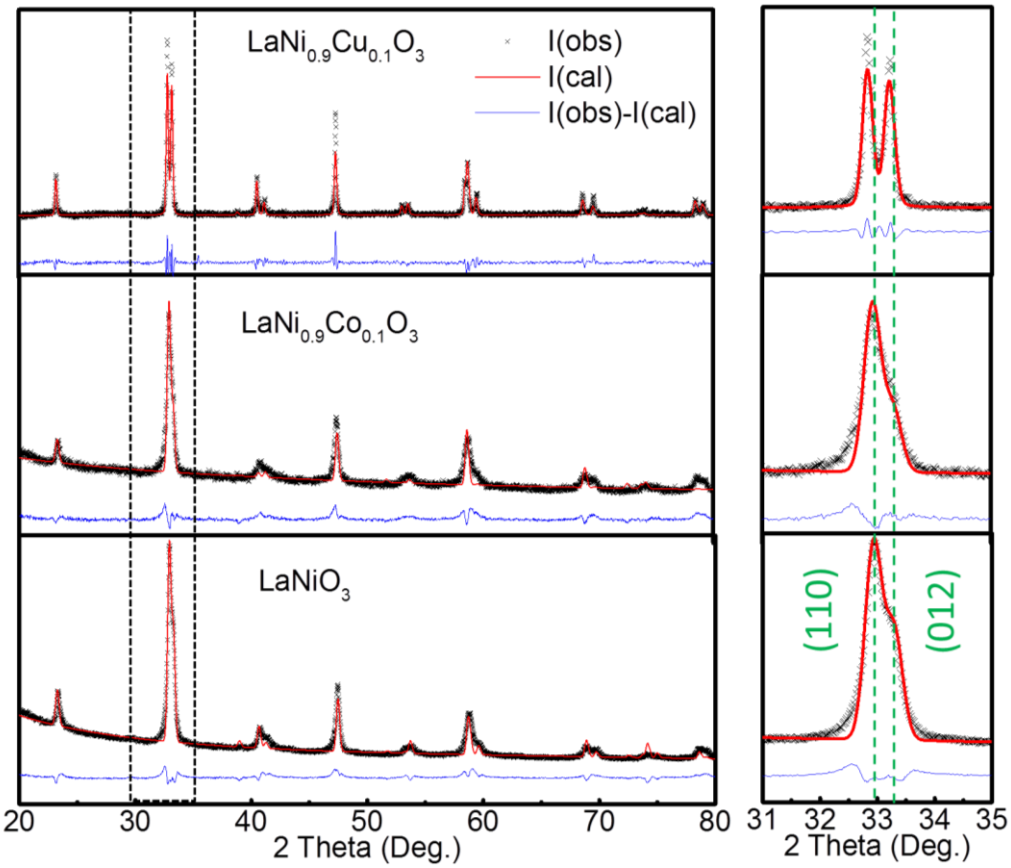

Figure 4.2 XRD patterns of the synthesized $LaNiO_3$, $LaNi_{0.9}Cu_{0.1}O_3$, and $LaNi_{0.9}Co_{0.1}O_3$ catalysts.

The as-prepared samples of the different nanosheets were characterized by scanning transmission electron microscopy (STEM), selected area electron diffraction (SAED) and energy dispersive spectroscopy (EDS), as shown in **Figure 4.3**. The high-angle annular dark field (HAADF) images in Figure 4.3d were employed to investigate multiple edge dislocations or strain $LaNi_{0.9}Cu_{0.1}O_3$ crystals. There are obvious crystal strains and dislocation defects in $LaNi_{0.9}Cu_{0.1}O_3$ crystal, as indicated in Figure 4.3d. These lattice strains and defects may result both from the substitution of different sized transition metal ions and from oxygen vacancy

caused by the substitution of elements with a different valence state, both of which can dramatically enhance catalytic activities. Furthermore, after the substitution of different transition metals, as shown in Figure 4.3e, a single component and phase structure distribution still exists, which is consistent with the XRD results. The EDS spectrum of $LaNi_{0.9}Cu_{0.1}O_3$ plate (Figure 4.3e) also indicates that the molar ratio of Cu to Ni is 0.105, which is close to the 10% Cu doping which is consistent with the feeding ratio.

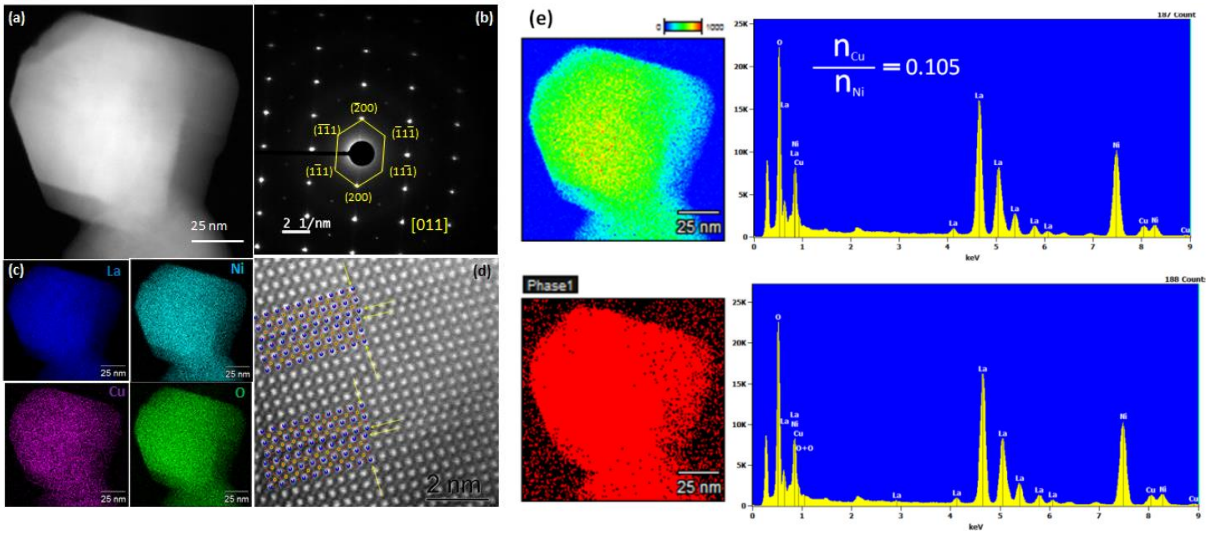

Figure 4.3 (a) TEM image of a single $LaNi_{0.9}Cu_{0.1}O_3$ nanosheet, (b) the corresponding SAED pattern, (c) TEM EDS mapping of La, Ni, Cu, and O elements on the chosen plate, (d) STEM image of $LaNi_{0.9}Cu_{0.1}O_3$ crystal with crystal strain due to edge dislocations, (e) component and phase distribution in $LaNi_{0.9}Cu_{0.1}O_3$.

4.3.2 Electrochemical characterization

The superior catalytic activity of $LaNi_{0.9}Cu_{0.1}O_3$ can be mainly attributed to the abundant highly efficient catalytic sites provided by lattice strains and oxygen vacancies. In this case, the lattice strains and oxygen vacancies can act as nucleated sites for Li_2O_2 growth during discharge process. The similar defects in graphene were also reported to enhance the Li_2O_2 formation

process.[48] Cyclic voltammograms (CVs) were collected in an O_2 saturated organic system [1 M $LiCF_3SO_3$ in tetraethylene glycol dimethyl ether (TEGDME)], and testing for lithium-oxygen battery application was carried out, as shown in Fig. 4.4. In Fig. 4.4a, during the cathodic period for the ORR, the onset potential was recorded at 2.7 V for all specimens. In the anodic regime, a characteristic earlier decomposition peak was observed at 3.5 V for both $LaNi_{0.9}Cu_{0.1}O_3$ and $LaNi_{0.9}Co_{0.1}O_3$, suggesting superior catalytic activity in the organic system after the different types of transition metal doping. Looking at the overall CV profiles, $LaNi_{0.9}Cu_{0.1}O_3$ shows the highest current density in both the cathodic and the anodic regions among all samples. The capacity-limited method was employed to evaluate the electrochemical performance in lithium-oxygen batteries. Compared to the other samples, $LaNi_{0.9}Cu_{0.1}O_3$ shows the lowest overpotential, 1.5 V at 0.1 mA cm^{-2} current density with a fixed specific capacity of 1000 mAh g^{-1}. After 100 cycles [Figure 4.4c], the overpotential gradually increased to 2 V. In Figure 4.4d, the discharge and charge capacities remained stable, and in addition, the discharge terminal voltage was higher than 2.36 V after 100 cycles. Generally speaking, the perovskite oxide $LaNi_{0.9}Cu_{0.1}O_3$ can be used as an electrocatalyst in the Li-O_2 battery and demonstrates good electrochemical performance, which can be attributed to the high catalytic activity of the $LaNi_{0.9}Cu_{0.1}O_3$ and the porous air electrode structure, with the porous channels facilitating rapid O_2 diffusion and providing a high density of reactive sites.

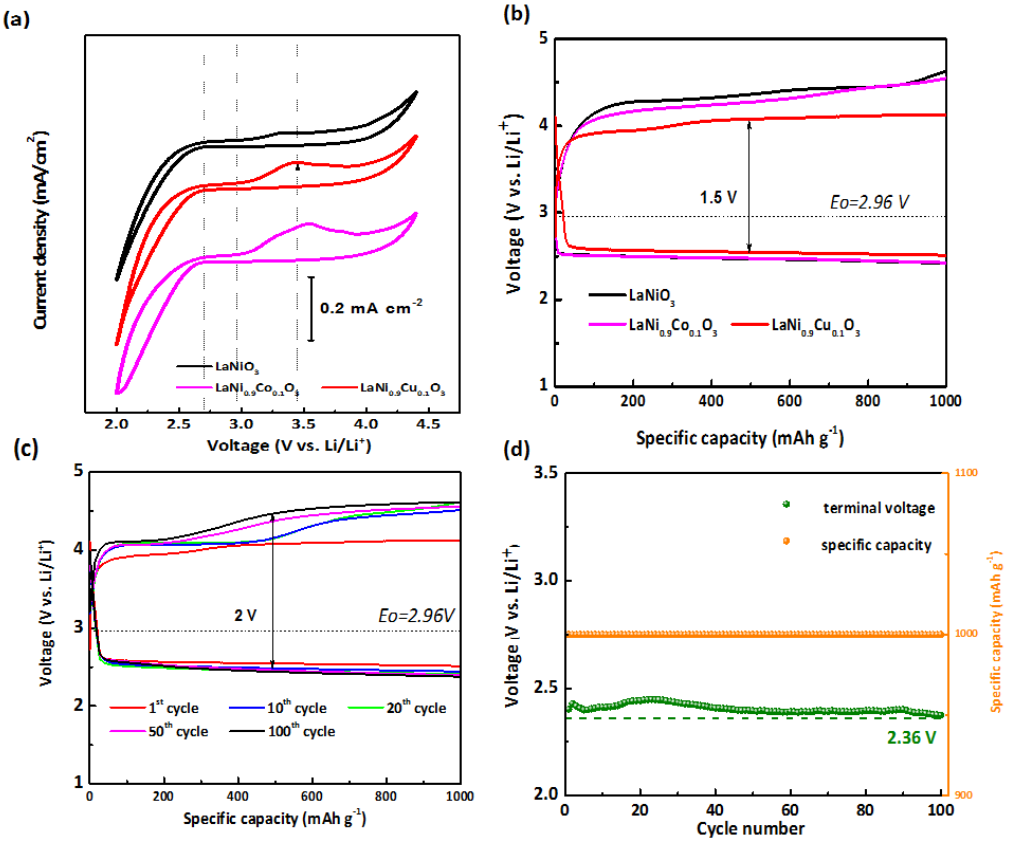

Figure 4.4 (a) Cyclic voltammograms (CVs) and (b) voltage profiles of the first discharge/charge cycle for $LaNiO_3$, $LaNi_{0.9}Cu_{0.1}O_3$, and $LaNi_{0.9}Co_{0.1}O_3$ catalysts grown on nickel foam; (c) voltage profiles of $LaNi_{0.9}Cu_{0.1}O_3$ sample for selected cycles at 0.1 mA cm^2, with the capacity limited to 1000 mAh g^{-1}; (d) discharge terminal voltage and specific capacity vs. the cycle number for $LaNi_{0.9}Cu_{0.1}O_3$ catalyst grown on nickel foam.

To investigate the discharge product formation on $LaNi_{0.9}Cu_{0.1}O_3$ catalyst, XRD measurements were carried out on the electrode at different discharge-charge stages. The XRD patterns of $LaNi_{0.9}Cu_{0.1}O_3$ after the first discharge and first cycle are shown in **Figure 4.5a**. Compared with the XRD pattern of the fresh electrode, the (101) peak of Li_2O_2 at 35.5° can be observed in the discharge pattern. The second strong peak (100) of Li_2O_2 is not visible because of the overlapping with the strong peak of $LaNi_{0.9}Cu_{0.1}O_3$ at 32.8°. After the first charge, the (101) peak also disappears in the 1st cycle XRD pattern, which indicates that the Li_2O_2 was completely reduced in the cathode. The schematic diagrams of Li_2O_2 formation on the catalyst clearly illustrate the reaction process during the whole progress of discharge and charge [Figure

4.5e]. We propose that Li_2O_2 is slowly deposited on the catalyst plate. At the end of the discharge process, the whole catalyst is covered with Li_2O_2. From the scanning electron microscope (SEM) image of the discharge cathode in Figure 4.5c, we can see that Li_2O_2 has covered all the gaps between the $LaNi_{0.9}Cu_{0.1}O_3$ nanosheets. During the charging process, Li_2O_2 is decomposed and then oxidized to O_2. It can be seen from Figure 4.5d that all the Li_2O_2 has been removed, and the plates and the gaps are visible again. The recovery of these $LaNi_{0.9}Cu_{0.1}O_3$ structures also indicates that the Li_2O_2 formation is reversible and that the porous catalyst can be used as an efficient catalyst in the Li-O_2 battery.

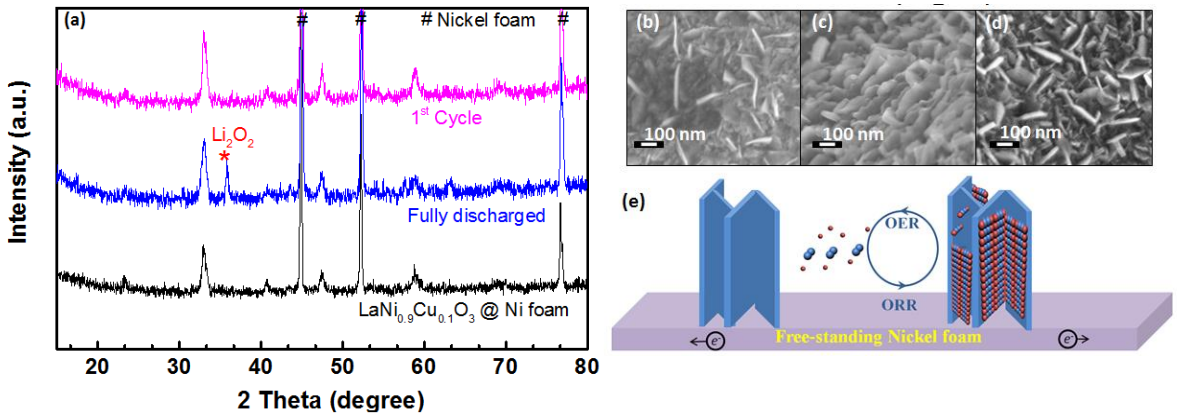

Figure 4.5 (a) XRD patterns of $LaNi_{0.9}Cu_{0.1}O_3$ electrode at different states of discharge and charge; (b) FESEM image of fresh cathode electrode; FESEM images of cathode after: (c) full discharge and (d) the 1st charge; (e) schematic illustration of the discharging and charging processes.

The utilization of redox mediators has been well proposed by P. Bruce and other groups to reduce charge-discharge overpotential.[178-181] As indicated in **Figure 4.6**a, the addition of the redox mediator tetrathiafulvalene (TTF) can further reduce the overpotential from 1.5 V to 0.72 V. The charge plateau of the cell at the first cycle is also lower than 3.6 V, with a high 80% round-trip efficiency, which is essential for electrochemical energy storage devices. The discharge and charge overpotentials stay at the low values of 0.19 V and 0.53 V, respectively. The charge terminal potential and overpotential in this work is compared

with previously published works in Figure 4.6b. Although different current densities were used, we can roughly conclude that the combination of the TTF mediator and $LaNi_{0.9}Cu_{0.1}O_3$ exhibits both low overpotential and low charge potential. The low overpotential and charge voltage can be attributed to the combination of the microporous structured air electrode and the highly efficient $LaNi_{0.9}Cu_{0.1}O_3$ nanosheet catalyst together with TTF additive.

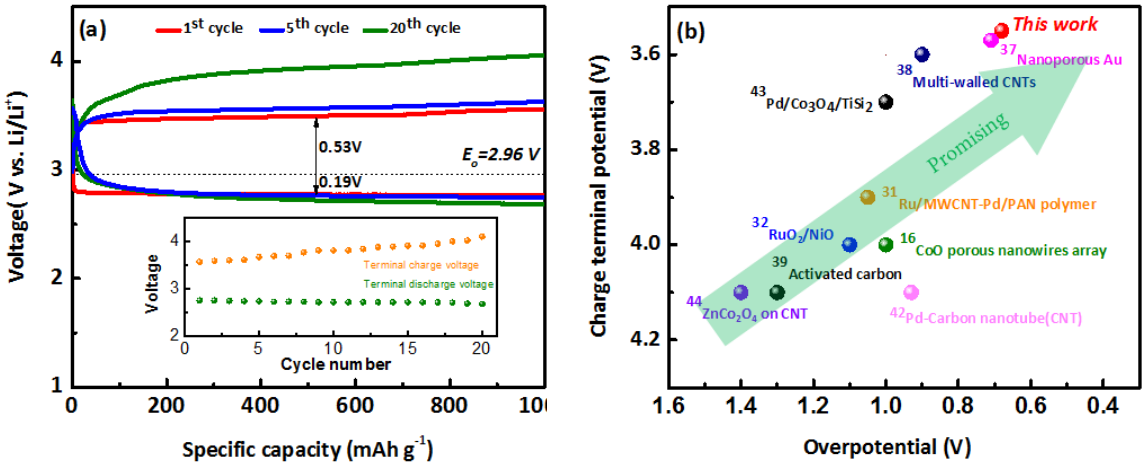

Figure 4.6 (a) Cycling profiles for selected cycles of $LaNi_{0.9}Cu_{0.1}O_3$ sample at 0.1 mA cm^{-2} with TTF added as redox mediator (inset: terminal charge and discharge voltages over the first 20 cycles); (b) Charge terminal potential vs. overpotential from this work and previously published works on cathode electrocatalysts.[52]

4.4 Summary

In conclusion, nanosheets of the transition-metal-doped perovskite oxides $LaNi_{0.9}M_{0.1}O_3$ (M = Cu, Co) grown on 3D microporous nickel foam can serve as a complete carbon- and binder-free air electrode for Li-O_2 batteries. Perovskite oxide with substitution on Ni^{3+} sites by Cu^{2+} ions with a different size and valence state demonstrates dramatically enhanced catalytic activity, both in aqueous and non-aqueous systems, because of the abundant lattice strains and oxygen vacancies. Together with the designed microporous structure and redox mediator utilization, this $LaNi_{0.9}Cu_{0.1}O_3$ air electrode is a promising catalyst for high efficiency lithium-

oxygen batteries, with lower cost and higher electrochemical performance compared with some precious metal catalysts.

Chapter 5 Three-Dimensional Array of TiN@Pt_3Cu Nanowires as an Efficient Electrode for the Lithium–Oxygen Battery

5.1 Introduction

Pt-based bimetallic nanocrystals have drawn extensive attention owing to their excellent catalytic activity in both aqueous and nonaqueous systems. It has also been evident that the optimization of different types of lattice facets expressed on the surface and the introduction of surface lattice strain resulting from deposited transition metals can dramatically modify the binding properties of adsorbates and thus enhance their catalytic activity. [182-183] For example, it has been found that the {111} surface can be made catalytically more active than other low-index surfaces by introducing compressive strain into the Pt lattice to weaken the binding of adsorbed O and OH. [184] Therefore, due to abundant {111} active facets and multiple twin boundaries, an active-surface-dominated type of nanocrystal, icosahedral nanocrystal, was synthesized and applied in many different related fields. [185] For a regular icosahedral nanocrystal, one important characteristic is that the surface is made up of 20 tetrahedral subunits with 30 twin boundaries, resulting in a surface bounded by 20 {111} facets. This structural feature may result in inherently superior properties toward oxygen catalytic behavior, which will be even more promising for obtaining excellent catalytic activity in the lithium–oxygen battery. Nevertheless, such tiny active nanocrystals generally tend to

aggregate and/or be detached from conventional carbon supports, leading to major deterioration in performance over time during device operation. [186] In addition, the commonly used carbon-based supports or catalysts, such as graphene or carbon nanotubes, are not stable in the oxygen-rich electrochemical environment in the lithium–oxygen battery system, being vulnerable to nucleophilic attack from highly active intermediate radicals and then being decomposed to LiF, LiOH, and Li_2CO_3.

Therefore, in this work, for the porous air electrode, icosahedral Pt_3Cu nanocrystals, deposited uniformly on a flower-like array consisting of one-dimensional (1D) high-orientation crystalline titanium nitride (TiN), have been employed as a novel, carbon-free three-dimensional (3D) porous air electrode in lithium–oxygen batteries. Owing to its 20 high-catalytic-activity tetrahedral subunits with 30 twin boundaries, together with a combination of ligand, geometric, and/or ensemble effects, the icosahedral Pt_3Cu bimetallic nanocrystal catalyst can significantly enhance the kinetics of the ORR and OER in the lithium–oxygen battery system. Meanwhile, stable TiN holds great promise as an electronic material due to its high corrosion resistance and superior electrical conductivity (4–555 K S cm^{-1}). [187-189] Thus, this flower-like array of TiN can also form a continuous conductive electrode framework and improve the adsorption of and immersion in electrolyte in order to facilitate the electrode reaction kinetics for high-energy conversion.

5.2 Experimental

Experiment Method

Synthesis of 3D Array TiN@Pt_3Cu Air Electrodes

The TiN nanowire array was synthesized by a two-step process. First, TiO_2 NWs were grown on carbon cloth by a seed-assisted hydrothermal method reported elsewhere. [190] The obtained TiO_2 grown on the carbon cloth was annealed at 350 °C for 3 h in air atmosphere to remove the

carbon fiber template and then annealed at 900 °C for 1 h in NH_3 atmosphere to convert the TiO_2nanowires into TiN nanowires. Platinum(II) acetylacetonate ($Pt(acac)_2$) and copper(II) acetylacetonate ($Cu(acac)_2$) in a molar ratio of 3:1 was dissolved in *N*,*N*-dimethylformamide solution, and the obtained TiN array powder was then dispersed into the above solution by a 1 h ultrasonication treatment. The feeding weight ratio of Pt_3Cu was 10% in the composite. The 65 mL homogeneous solution was transferred into a Teflon-lined stainless steel autoclave (120 mL, Parr) for the hydrothermal reaction at 200 ℃ for 24 h. The obtained composites were further washed with water and acetone several times and then dried to obtain the final product.

Characterization

The structure and phase purity were analyzed by X-ray powder diffraction (GBC MMA) on an instrument equipped with Cu Kα radiation that was operated over a 2θ range of 20–80° in continuous scan mode with a scan rate of 1° min^{-1}. The morphology of the samples was examined using field-emission scanning electron microscopy (JEOL JSM-7500). Transmission electron microscopy investigations were performed using a 200 kV JEOL 2011 instrument. Scanning transmission electron microscopy was performed using a 200 kV JEOL 2011 instrument.

Catalytic and Electrochemical Performance

The electrochemical performance was tested using CR2032-type coin cells with holes in the cathode part. To prepare the TiN@Pt_3Cu working electrodes, a mixture of the as-synthesized catalyst and poly(tetrafluoroethylene) (PTFE) solution in a weight ratio of 90:10, respectively, was pasted onto the stainless steel mesh in the cathode part (with the mesh edge welded onto the cathode shell). The same procedure and ratio were used to prepare the Pt_3Cu air electrode, using the same amount of TiN as a conductive material and using PTFE as a binder. Typical loading of cathode powder for the 1x1 cm^2 area was ~2 mg cm^{-2}. The electrolyte consisted of

a solution of 1 M $LiClO_4$ in dimethylsulfoxide, and 0.1 mM tetrathiafulvalene was added to the electrolyte as the redox mediator. The solvents were refluxed with calcium hydride and distilled under an argon atmosphere, before being stored over 4 Å molecular sieves under argon. The $LiClO_4$ was dried at 180 °C in vacuum for 12 h. Pure lithium foil was used as the counter electrode. The cells were assembled in an argon-filled glovebox (Mbraun, Unilab, Germany). Galvanostatic deep, full charge–discharge curves were collected at various current densities of 0.2, 0.4, 0.6, and 0.8 mA cm^{-2} between 3.8 and 2.45 V *vs* Li/Li^+, and discharge–charge cycling was conducted with a 1000 mAh g^{-1} cutoff discharge and charge capacity. All tests were conducted on LAND CT 2001A multichannel battery testers at room temperature in oxygen atmosphere, using our designed facility. RDE tests were performed using a computer-controlled potentiostat (Princeton 2273 and 616, Princeton Applied Research) in a conventional three-electrode cell at room temperature. The glassy carbon (GC) working electrode (5 mm in diameter) was first polished with 1.0 and 0.05 μm alumina powder, rinsed with deionized water, and sonicated first in ethanol and then in double-distilled water. A platinum wire and Ag/AgCl (saturated KCl filled) were used as the counter and reference electrodes, respectively. Typically, the $NiCo_2O_4$ was redispersed in deionized water + isopropanol + 5% Nafion® (v/v/v = 4/1/0.05) to form a homogeneous catalyst ink with a concentration of 2 mg mL^{-1}. Then, 30 μL of this dispersion was pipetted onto the surface of the GC working electrode and dried under ambient conditions. For comparison, the control samples were Super P and commercial Pt/C (10 wt.% Pt on Vulcan XC-72), and were also obtained by the same method described above. Cyclic voltammograms (CVs) were collected in O_2 saturated 0.1 M KOH solution from - 0.9 V – 0.1 V at a scan rate of 10 mV s^{-1}. Linear sweep voltammograms (LSVs) to measure the ORR performance were collected in O_2 saturated 0.1 M KOH solution with different rotation speeds from 100 to 2500 rpm from - 0.9 -0.1 V with a scan rate of 10 mV s^{-1}, while OER plots were obtained in Ar atmosphere from

0.1 -0.9 V with a scan rate of 10 mV s^{-1} and a rotation speed of 1600 rpm. Koutecky-Levich (K-L) plots show the inverse current density (j^{-1}) as a function of the inverse of the square root of the rotation speed ($\omega^{-1/2}$) at different potential values. The number of electrons involved per O_2 in the ORR was determined by the Koutecky-Levichequation:

$$\frac{1}{j} = \frac{1}{j_k} + \frac{1}{j_d} = \frac{1}{B\omega^{1/2}} + \frac{1}{j_k} \quad (1)$$

where j, j_k j_d are the measured, the kinetically controlled and the diffusion controlled current densities, respectively, and ω is the electrode rotation rate. *B* is determined from the slope of the K-L plot based on the Levich equation:

$$B = 0.2nF(D_{O2})^{2/3} v^{-1/6} C_{O2} \quad (2)$$

where *n* represents the number of electrons gained per O_2, *F* is the Faraday constant (*F* = 96485 C mol^{-1}), Do_2 is the diffusion coefficient of O_2 in 0.1 M KOH (1.9×10^{-5} cm^2 s^{-1}), *v* is the kinetic viscosity (0.01 cm^2 s^{-1}), and C_{O2} is the bulk concentration of O_2 (1.2×10^{-6} mol cm^{-3}). CVs were also obtained using the same procedure.

5.3 Results and discussion

5.3.1 Structure and morphology

The general synthesis process for the 3D flower-like array-structured porous air electrodecontaining the $TiN@Pt_3Cu$ composite (denoted as FLA-$TiN@Pt_3Cu$) is illustrated in Figure 5.1a. Typically, the TiO_2 nanowire array was synthesized by the seed-assisted hydrothermal method. As shown in Figure 5.1a, the carbon fiber template is totally removed, and the TiO_2 nanowires exhibit a 3D porous flower-like array structure. Then, the TiN nanowire array was obtained by annealing the as-prepared TiO_2 nanowire array in an

ammonia atmosphere at 900 °C, with the nanowire diameters still kept in the range of 100 nm. In the following stage, icosahedral stoichiometric Pt_3Cu bimetallic nanocrystal catalysts were deposited on the nanowires uniformly via the solvothermal method. As shown in Figure 5.1b, TiN exhibits a standard cubic diffraction pattern, whereas the Pt_3Cu reflection peaks, from the (111), (200), and (220) planes, are shifted right compared with the standard Pt pattern. The FLA-TiN@Pt_3Cu air electrode can be indexed as mixed phase, with TiN and Pt_3Cu phases. Pt_3Cu bimetallic nanocrystals were deposited uniformly on the surfaces of nanowires, as shown in Figure 5.1c, with a majority of 2.5 nm particles in the size distribution. According to some reported results, [191-192] there is a definite link between the catalyst particle size distribution and catalytic activity. Much evidence has also confirmed that this appropriate particle size distribution, especially with a peak at 2–5 nm, is beneficial for achieving high catalytic activity. In the FLA-TiN@Pt_3Cu air electrode, the Pt_3Cu nanocrystals with proper particle size and a narrow size distribution were deposited uniformly on the 1D TiN nanowires. Meanwhile, the electron diffraction pattern of an individual nanowire, as shown in Figure 5.1d, reveals that the TiN nanowires show a strong high-orientation crystalline texture along the [001] growth direction, which can provide superior electrical conductivity for the FLA-TiN@Pt_3Cu air electrode because of the nearly single-crystalline structure.

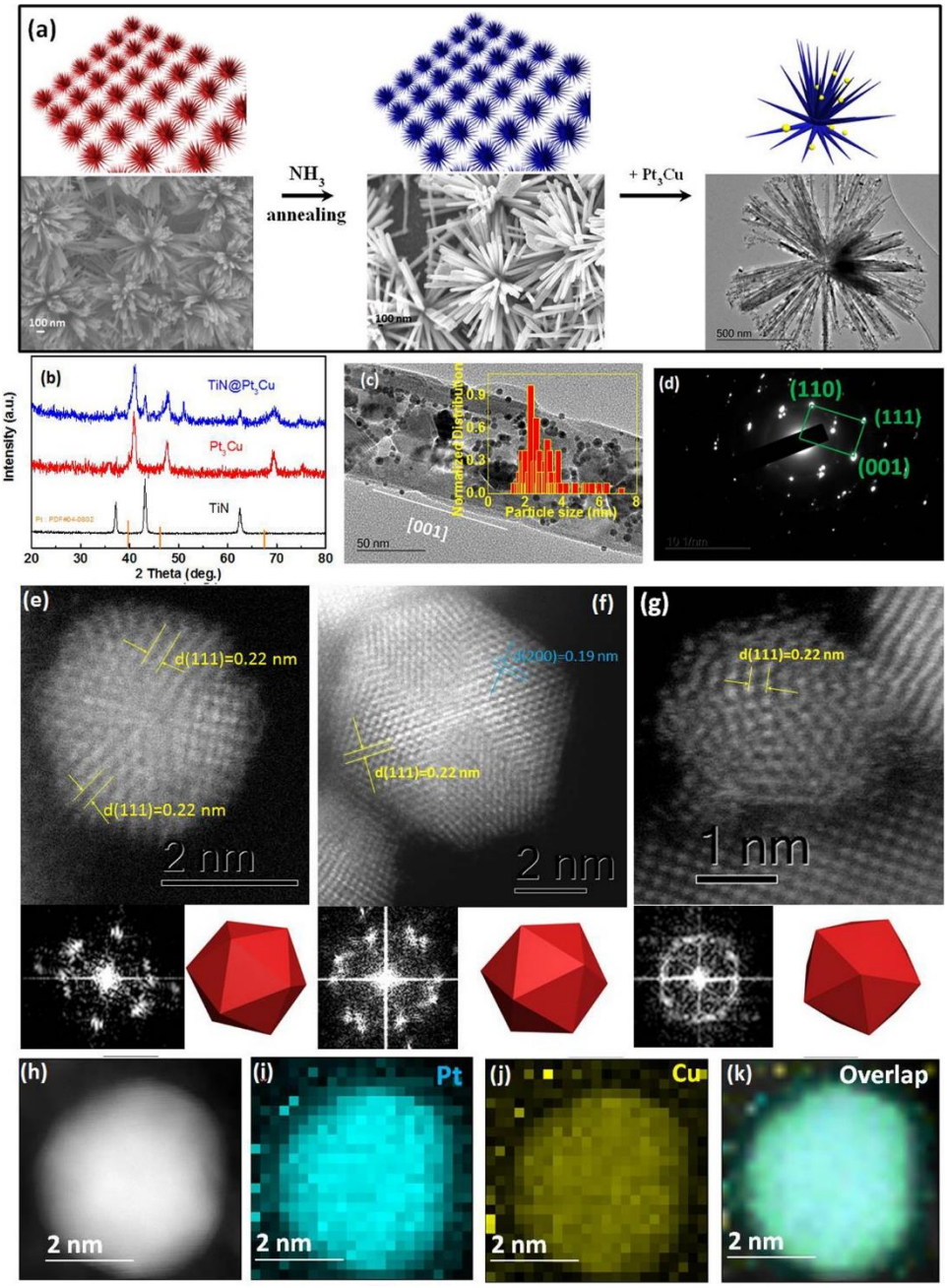

Figure 5.1 (a) Schematic illustration of the formation of the FLA-TiN@Pt_3Cu air electrode. (b) X-ray diffraction results for TiN, Pt_3Cu, and TiN@Pt_3Cu. (c) Transmission electron microscope (TEM) image of an individual TiN@Pt_3Cu electrocatalyst nanowire (with Pt_3Cu particle size distribution as inset image). (d) Electron diffraction pattern of an area of (c). (e–g) HAADF-STEM images, corresponding FFT images, and geometrical models of Pt_3Cu icosahedral nanocrystals. (h–k) HAADF-STEM energy-dispersive X-ray spectroscopy element mapping of an individual Pt_3Cu icosahedral nanocrystal.

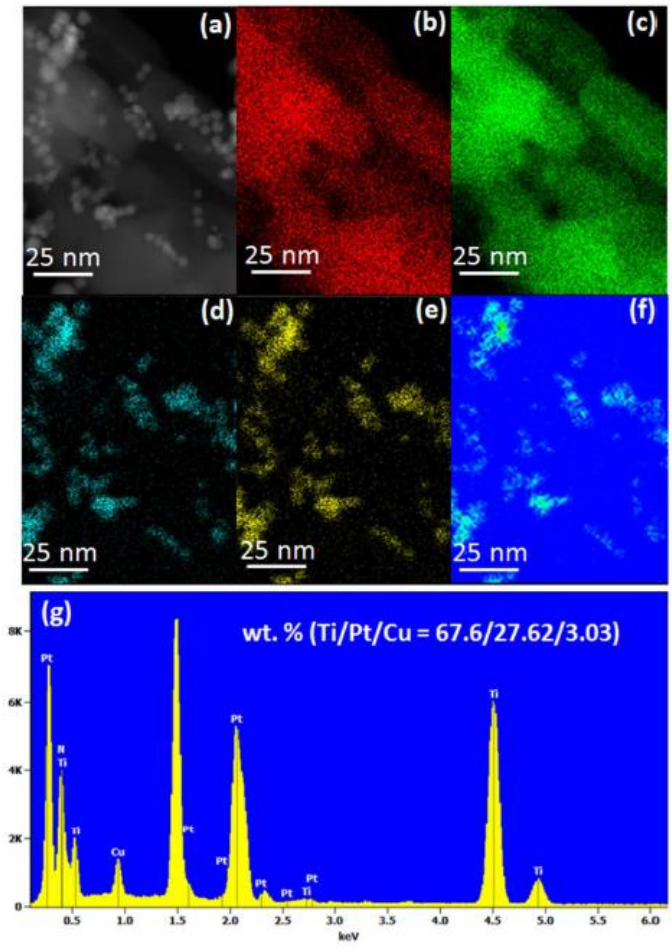

Figure 5.2 (a) High-angle annular dark-field scanning TEM (HAADF-STEM) image of TiN@Pt_3Cu; HAADF-STEM-energy-dispersive X-ray spectroscopy (EDS) element mapping of (b) Ti, (c) N, (d) Pt, (e) Cu; (f) phase distribution of Pt_3Cu icosahedral nanocrystals; (g) corresponding EDS spectrum.

The scanning transmission electron microscopy (STEM) image in **Figure 5.2**a indicates that the Pt_3Cu nanocrystals are distributed uniformly on the walls of the one-dimensional TiN nanowires, which comprise identical crystalline orientated TiNnanorods. Meanwhile, all the elements in Figure 5.2b–e, such as Ti, N, Pt, and Cu, demonstrate the corresponding homogeneous distributions over the given area. The combined component distribution shown in Figure 5.2f further reveals the formation of the alloyed structure of the Pt_3Cu nanocrystals. The ratio of Pt to Cu in the composition is approximately 3:1, and the Pt_3Cu nanocrystals occupy nearly 10 wt % in the composite, as confirmed by STEM energy-

dispersive X-ray spectroscopy (EDS) (Figure 5.2g), both of which are consistent with the feeding rate. Detailed information on the as-prepared Pt_3Cu nanocrystals was provided by high-angle annular dark-field scanning TEM (HAADF-STEM). As shown in Figure 5.1e–g, typical images of individual Pt_3Cu nanocrystals projected along the three-fold, two-fold, and five-fold axes collectively indicate that the deposited alloyed nanocrystals are essential icosahedra, which is highly consistent with geometric models of icosahedra consisting of 20 tetrahedral subunits with 30 twin boundaries and 20 exposed {111} triangular facets. The corresponding fast Fourier transforms (FFT) of individual icosahedral nanocrystals also confirm the multiply twinned icosahedral structure. The lattice fringes in Pt_3Cu icosahedral nanocrystals have measured spacings of 2.2 and 1.9 Å, which can be indexed to the (111) and (220) planes of face-centered cubic (fcc nanocrystals), respectively. These planar spacings are smaller than those of fcc Pt, and they also provide evidence of the formation of the alloyed structure.[182] The distribution of elements in the alloyed structure was characterized by HAADF-STEM energy-dispersive X-ray spectroscopy (HAADF-STEM-EDS), as shown in Figure 5.1h–k. The elements Pt and Cu show a similar homogeneous distribution over the entire area.

5.3.2 Electrochemical characterization

The hydrodynamic technique based on a rotating disk electrode (RDE) was used to evaluate the oxygen reduction reaction activities of these three samples, including pure TiN nanowires(NWs), Pt_3Cu icosahedral nanocrystals, and a TiN@Pt_3Cu composite, benchmarked against high-quality commercial Pt/C (20 wt % Pt on Vulcan XC-72) in an O_2-saturated 0.1 M KOH electrolyte at a scan rate of 10 mV s^{-1}. The RDE curves at various rotation speeds were investigated to determine each sample's ORR kinetic performance, as shown in Figure 5.3.

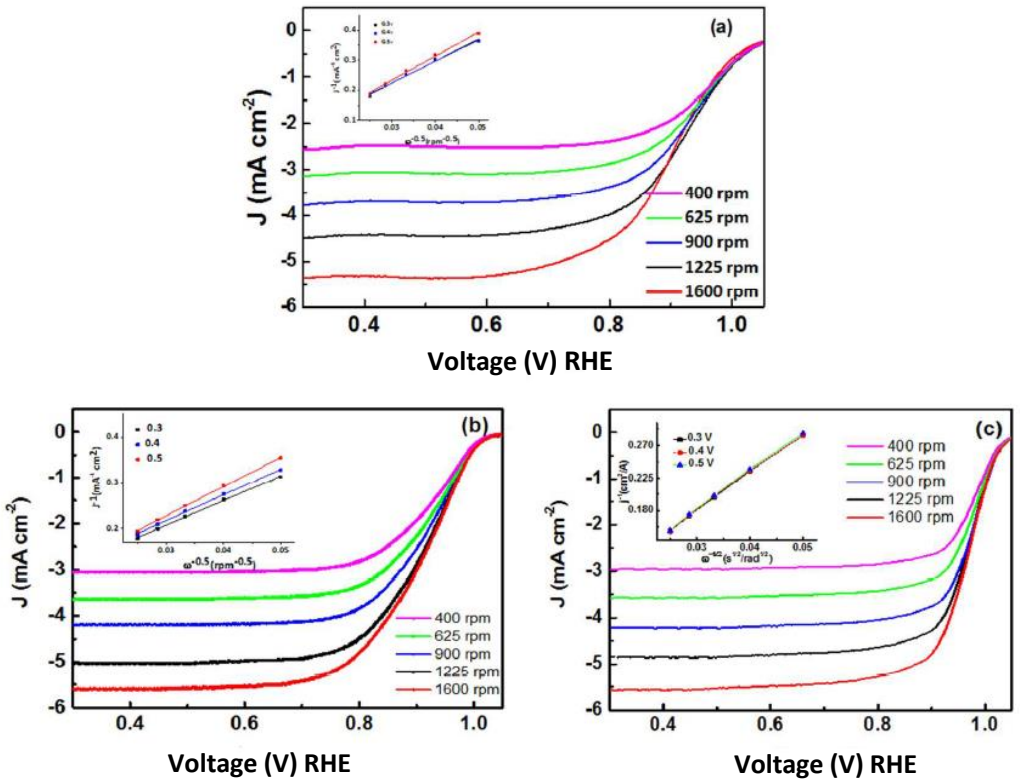

Figure 5.3 (a) RDE curves of commercial Pt/C (20 wt.% Pt on Vulcan XC-72); (b) Pt_3Cu, and (c)TiN@Pt_3Cu in O_2-saturated 0.1 M KOH solution with various rotation speeds and a sweep rate of 10 mV s^{-1}.

The corresponding Koutecky–Levich (K–L) plots (J^{-1} vs $\omega^{-1/2}$) at various electrode potentials exhibit good linearity. The linearity and parallelism of the K–L plots suggest first-order reaction kinetics toward the concentration of dissolved oxygen and similar electron transfer numbers for the ORR at different potentials. Both the Pt_3Cu and the TiN@Pt_3Cu composite favor a nearly four-electron ORR process. Furthermore, as shown in the RDE curves and the corresponding Tafel curves in Figure 5.4a,b, compared with commercial Pt/C, Pt_3Cu and TiN@Pt_3Cu composites exhibit excellent ORR activities, with a positive onset potential and large limiting current density.

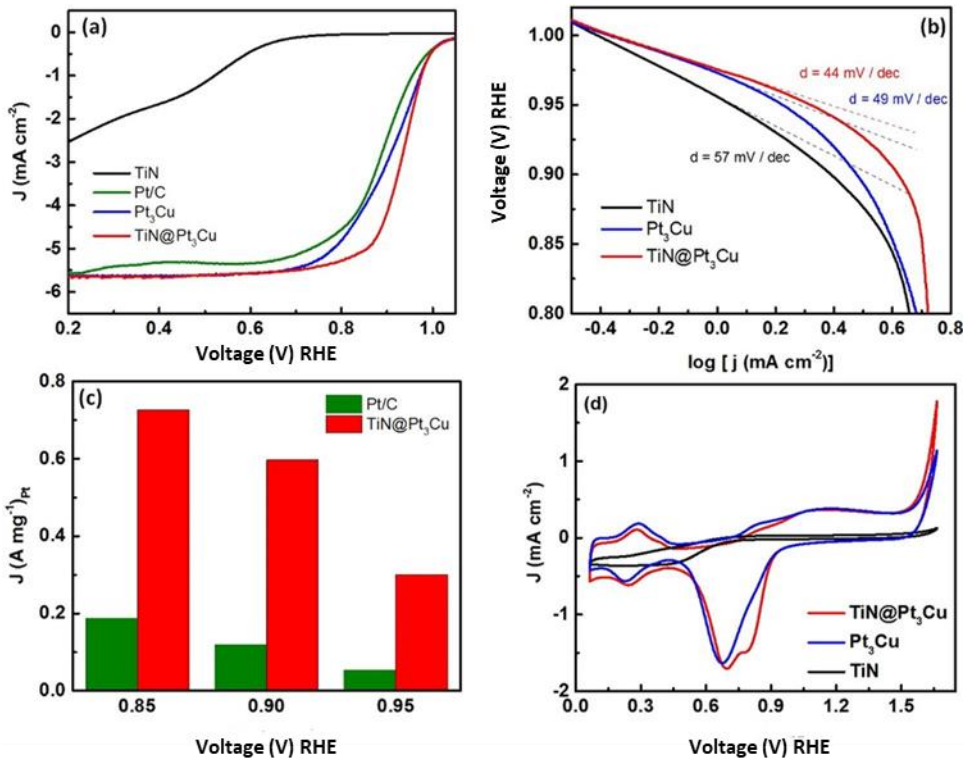

Figure 5.4 (a) RDE curves of high-quality commercial Pt/C (20 wt % Pt on Vulcan XC-72) and TiN NWs, Pt_3Cu, and TiN@ Pt_3Cu. (b) Tafel slopes of high-quality commercial Pt/C (20 wt % Pt on Vulcan XC-72) and TiN NWs, Pt_3Cu, and TiN@ Pt_3Cu. (c) Activity enhancement relative to commercial Pt/C based on Pt total mass, from the data shown in (a). (d) Cyclic voltammograms of TiN NWs, Pt_3Cu, and TiN@ Pt_3Cu. RHE: reversible hydrogen electrode.

The kinetic current densities at 0.85, 0.9, and 0.95 V were calculated based on the total Pt mass, as shown in Figure 5.4c. The TiN@Pt_3Cu composite shows mass activities of 0.72 A mg^{-1}_{Pt}, 0.59 A mg^{-1}_{Pt}, and 0.31 A mg^{-1}_{Pt}, respectively, a 3.8, 5, and 6.3 times enhancement compared with the commercial Pt/C. This excellent catalytic performance can be attributed to the high dispersion of icosahedral Pt_3Cu nanocrystal with multiple-twinned boundaries and abundant high-activity exposed {111} triangular facets. Cyclic voltammograms (CVs) in O_2-saturated 0.1 M KOH electrolyte were also used to reveal the ORR activity of the as-prepared samples and are presented in Figure 5.4d. Similar to pure Pt_3Cu, the TiN@Pt_3Cu composite also exhibits characteristic oxidation peaks as well as higher current density. The

electrochemical properties of the as-prepared FLA-TiN@Pt_3Cu were then tested by using it as an air electrode in a lithium–oxygen cell without any additional conductive carbon black. The specific capacities were calculated based on the total composite mass in the cathodes. The full discharge and charge performance at current density of 0.2 mA cm^{-2} is shown in **Figure 5.5**a.

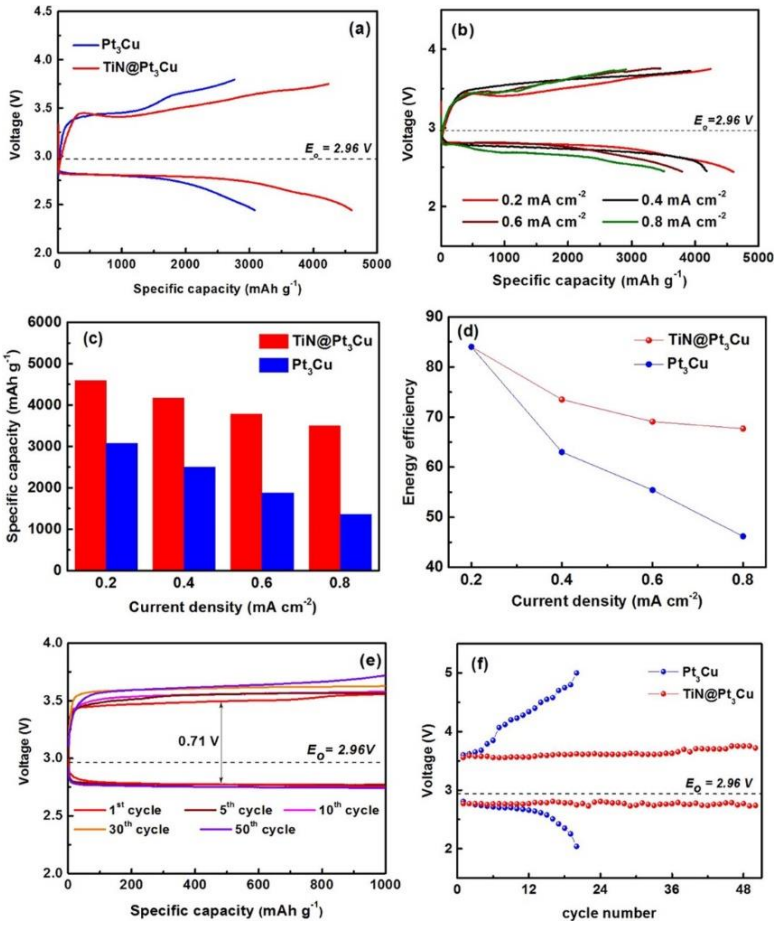

Figure 5.5 (a) Comparison of pure Pt_3Cu catalyst and TiN@Pt_3Cu composite on first-cycle full discharge/charge results at 0.2 mA cm^{-2} current density. (b) Discharge/charge curves of the TiN@Pt_3Cu composite at different current densities. (c) Capacity and (d) energy conversion efficiency comparison between pure Pt_3Cu catalyst and TiN@Pt_3Cu composite. (e) Discharge and charge curves of the TiN@Pt_3Cu composite for selected cycles. (f) Comparison of cycling performance of pure Pt_3Cu catalyst and TiN@Pt_3Cu composite with specific capacity limited to 1000 mAh g^{-1} at 0.2 mA cm^{-2} current density.

The pure Pt_3Cu icosahedral nanocrystals exhibit a low overpotential with discharge and charge capacities of 3065 and 2751 mAh g–1, respectively. Furthermore, compared with the Pt_3Cu icosahedral nanocrystals, FLA-TiN@Pt_3Cu shows much lower overpotential and higher

round-trip efficiency, up to 84%, which is vital for electrochemical energy storage devices, together with a discharge capacity of 4600 mAh g^{-1} and a charge capacity of 4310 mAh g^{-1}. These results can also be further confirmed by the CV and RDE curves in O_2-saturated nonaqueous electrolyte, as shown in **Figure 5.6**.

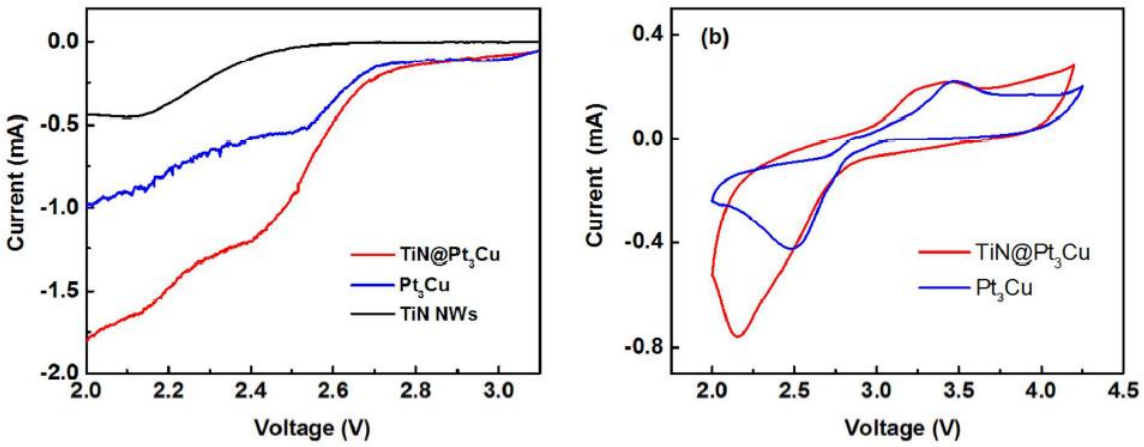

Figure 5.6 a) RDE curves from open voltage to 2.0 V in O2 saturated non-aqueous electrolyte at thespeed of 900 rpm; (b) Cyclic voltammograms (CV) in O_2 saturated non-aqueous electrolyte at 0.2 mVs^{-1} scan rate.

Compared with pure Pt_3Cu, the FLA-TiN@Pt_3Cu air electrode displays obviously higher ORR and OER currents and earlier OER potentials, which indicate that the FLA-TiN@Pt_3Cu air electrode provides a bifunctional catalyst performance in the anodic and cathodic scan processes. The comparison of capacity and energy conversion efficiency between pure Pt_3Cu icosahedral nanocrystals and the FLA-TiN@Pt_3Cu air electrode at different current densities is summarized in Figure 5.5b–d and **Figure 5.7**a.

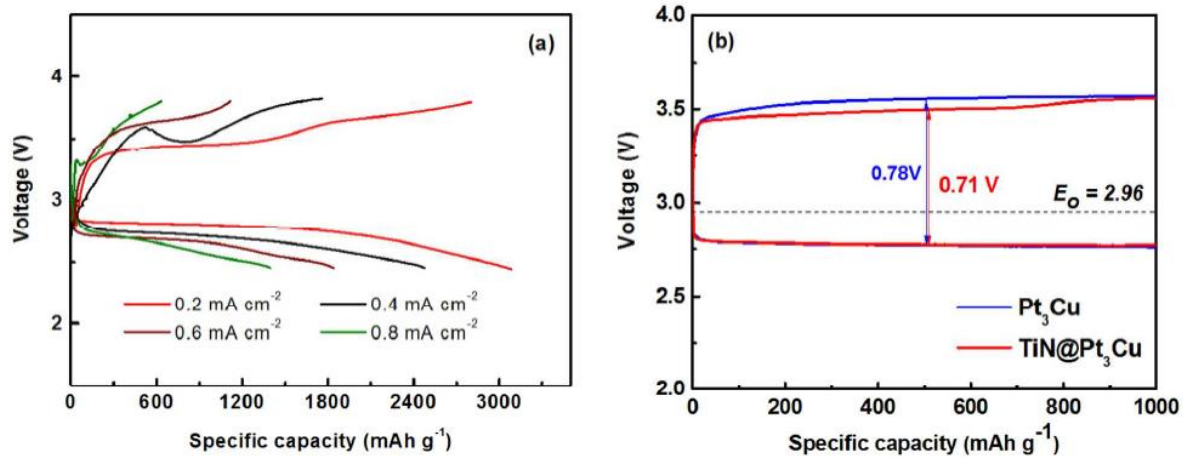

Figure 5.7 (a) Full discharge and charge profiles of pure Pt_3Cu at different current densities: 0.2 mA cm^{-2}, 0.4 mA cm^{-2}, 0.6 mA cm^{-2}, and 0.8 mA cm^{-2}. (b) Comparison of first cycle discharge/charge results at 0.2 mA cm^{-2} current density with 1000 mAh g^{-1} specific limited capacity for pure Cu catalyst and TiN@Pt_3Cu composite.

Excellent electrochemical performance is demonstrated by the FLA-TiN@Pt_3Cu air electrode. The FLA-TiN@Pt_3Cu exhibits excellent rate performance, with the energy efficiency reaching about 70% when the current density was increased from 0.2 to 0.8 mA cm^{-2}. When the current density was increased to 0.4, 0.6, and 0.8 mA cm^{-2}, as shown in Figure 5.5b, the FLA-TiN@Pt_3Cu still exhibited a high discharge capacity and low overpotential. In contrast, the energy conversion efficiency retention rate of the pure Pt_3Cu icosahedral air electrode was only 53% when the current density was increased from 0.2 to 0.8 mA cm^{-2}. This excellent electrochemical and rate performance is primarily attributable to the particular design of the FLA-TiN@Pt_3Cu porous air electrode structure and its high catalytic activity. This 3D array structure consists of long 1D TiN nanowires with high electrical conductivity, while the Pt_3Cu icosahedra can provide abundant reactive sites and enough space for rapid O_2 and electrolyte diffusion to avoid coverage of the active sites and blockage of diffusion pathways. The capacity-limited mode was used to evaluate the comprehensive

electrochemical performance. In Figure 5.7b, the overpotential of the FLA-TiN@Pt_3Cu air electrode is 0.71 V at a current density of 0.2 mA cm^{-2} with a fixed specific capacity of 1000 mAh g^{-1}, slightly smaller than that of the pure Pt_3Cu catalyst. Figure 5.5e,f and **Figure 5.8** evaluate the cycling performances of a pure TiN array and Pt_3Cu and TiN@Pt_3Cu composites at a 0.2 mA cm^{-2} current density with a fixed specific capacity of 1000 mAh g^{-1}.

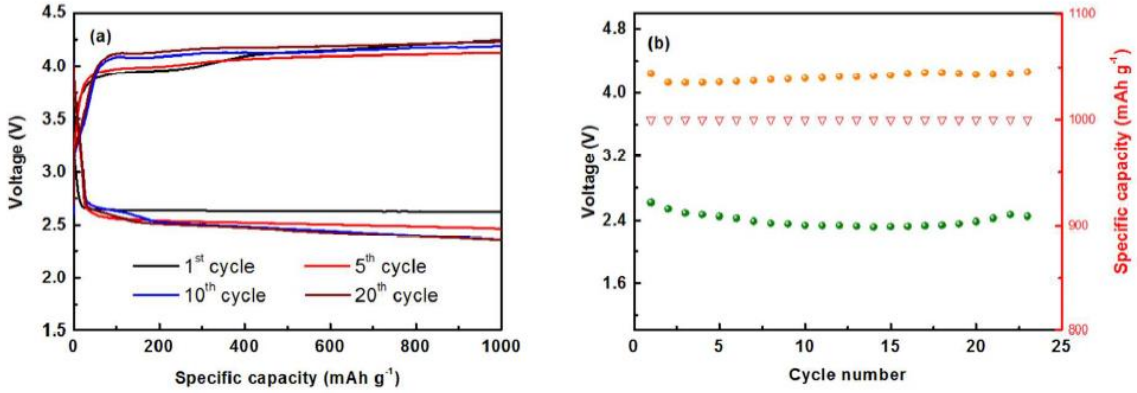

Figure 5.8 (a) discharge and charge curves of pure TiN array for selected cycles; (b) cycling performance of pure TiN array with specific capacity limited to 1000 mAh g^{-1} at 0.2 mA cm^{-2} current density.

Although the pure TiN array can also be used as an air electrode in a Li-O_2 battery, it exhibits unsatisfactory electrochemical performance. Compared with pure Pt_3Cu icosahedral nanocrystals, the discharge terminal voltage of the TiN@Pt_3Cu composite is greater than 2.7 V, whereas its charge terminal potential is less than 3.72 V for 50 cycles. Meanwhile, the energy efficiency of the FLA-TiN@Pt_3Cu air electrode at 50 cycles is still as high as 73%, as shown in **Figure 5.9**.

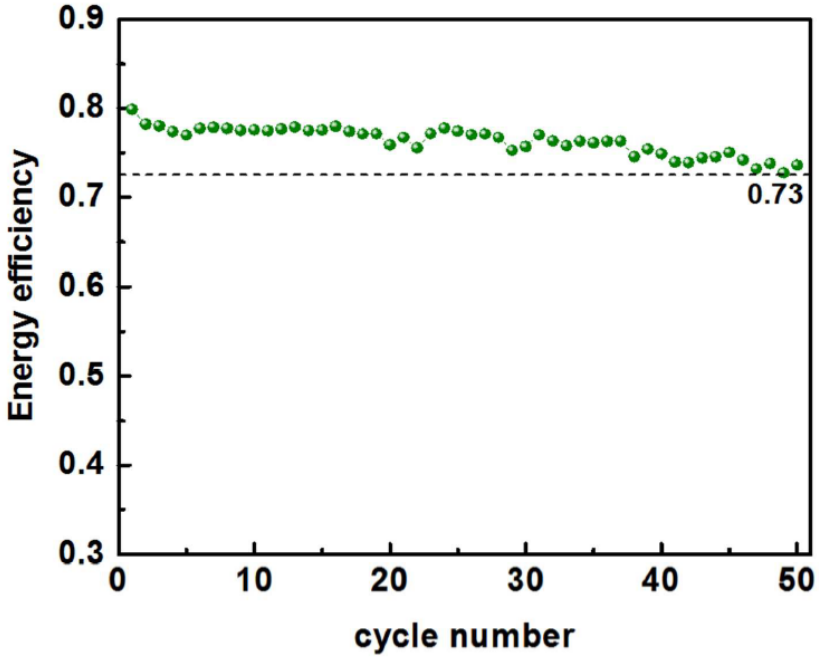

Figure 5.9 Energy conversion efficiency changes with cycling for TiN@Pt_3Cu composite.

The cycling performance without the redox mediator (tetrathiafulvalene) was also confirmed, as shown in Figure 5.10.

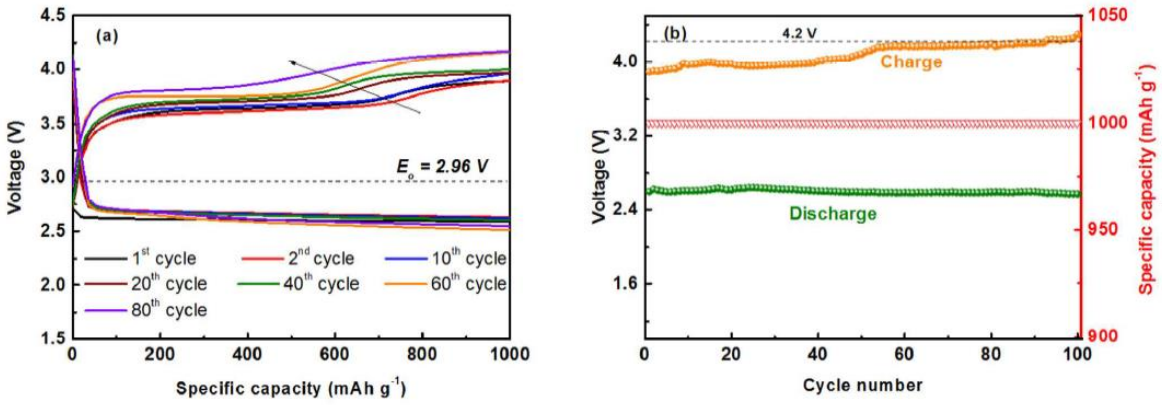

Figure 5.10 (a) Discharge/charge curves of FLA-TiN@Pt_3Cu for selected cycles and (b) cycling performance of the FLA-TiN@Pt_3Cu with specific capacity limited to 1000 mAh g^{-1} at 0.2 mA cm^{-2} current density without redox mediator (TTF).

The FLA-TiN@Pt_3Cu air electrode still exhibits a good cycling performance. The discharge and charge capacities retain stable values, and in addition, the discharge terminal voltage is greater than 2.5 V, and the charge terminal potential is less than 4.2 V for 100 cycles. The superior cycling performance of the FLA-TiN@Pt_3Cu air electrode is largely attributable to the porous air electrode structure, using a stable TiN nanowire as support for the icosahedral Pt_3Cu nanocrystals to avoid catalyst aggregation or detachment from the support during a long cycling period. To further understand the reaction mechanism over the whole performance, the morphology and the corresponding selected area electron diffraction (SAED) pattern of an individual 1D TiN@Pt_3Cu catalyst nanowire were investigated by high-resolution TEM (HRTEM), as shown in **Figure 5.11**.

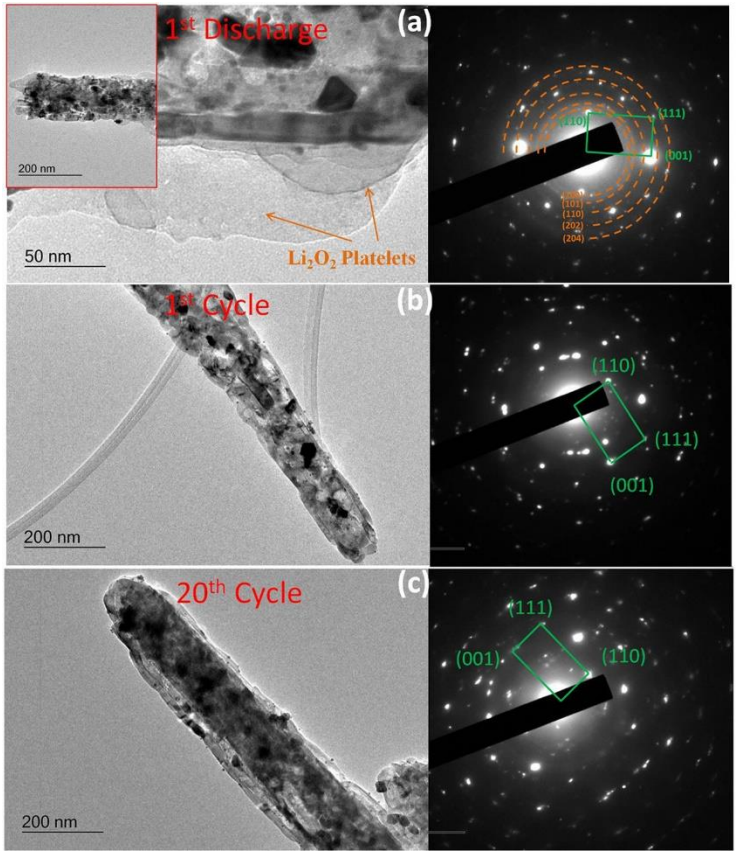

Figure 5.11 HRTEM images (left) and SAED patterns (right) of individual TiN@Pt_3Cu electrocatalyst nanowires: (a) after full discharge, (b) after the first cycle, and (c) after 20 cycles.

In the sample after the first discharge, the reaction products were deposited on the surface of the catalyst, and the TiN@Pt_3Cu catalyst still maintained its stable 1D morphology. As confirmed by the electron diffraction signal, besides the regular diffraction spots from the 1D TiN@Pt_3Cu catalyst, the five additional characteristic diffraction rings proved the formation of crystallized Li_2O_2. These Li_2O_2 platelets, roughly parallel to each other, are stacked layer-by-layer to form a nanosheet-shaped Li_2O_2 reaction product structure (inset image in Figure 5.11a). This stacked type of reaction product morphology was also observed in previous reported work.[193] In contrast to the large-sized reaction products, this stacked type can be proven to efficiently protect catalytic reaction sites from devitalization effects, including coverage of the active reaction sites and blockage of the gas and electrolyte diffusion. After full charging, as shown in Figure 5.11b, the corresponding five diffraction rings of Li_2O_2 disappear, indicating the high reversibility of Li_2O_2. [193] On the other hand, it can be observed that the TiN@Pt_3Cu catalyst maintains its stable 1D morphology, and the homogeneously deposited Pt_3Cu nanocrystals are still attached on the walls of the TiN NWs, even after 20 cycles, as shown in Figure 5.11c. This feature provides further evidence that TiN@Pt_3Cu will not passivate the catalytic activity during long cycling periods, a problem that mainly results from catalyst detachment.

5.4 Summary

In conclusion, this 3D array design comprising one-dimensional TiN@Pt_3Cu nanowires was employed as a complete porous air electrode in lithium–oxygen batteries, which has the inherent advantages of energy conversion by the highly efficient catalytic activity of icosahedral Pt_3Cu and the high electronic conductivity of the 3D TiN nanowire array as the framework for the electrode. In full discharge and charge mode, the discharge capacity reaches as high as 4600 mAh g^{-1}, along with 84% conversion efficiency at a current density of 0.2 mA

cm^{-2}. When the current density was increased to 0.8 mA mA cm^{-2}, the discharge capacity was still greater than 3500 mAh g^{-1}, together with nearly 70% efficiency. In 1000 mAh g^{-1} capacity-limited mode, the terminal discharge voltage is greater than 2.7 V, and the terminal charge voltage is less than 3.73 V after 50 cycles at a current density of 0.2 mA cm^{-2}. The reaction mechanism was also studied. The Li_2O_2 reaction products stack layer-by-layer to form a nanosheet-shaped Li_2O_2 reaction product structure. This formation process can efficiently protect catalytic reaction sites from devitalization effects, including coverage of the active reaction sites and blockage of the gas and electrolyte diffusion. Therefore, this carbon-free porous air electrode based on a 3D array of nanowires is a promising bifunctional electrocatalyst for lithium–oxygen batteries, with high energy density and favorable rechargeability combined with high energy conversion efficiency.

Chapter 6 Integrated Air Electrode for Zn-Air Battery

6.1 Introduction

From the catalyst point of view, Pt alloy is the promising catalyst for the ORR.[53] In catalyst review, Pt_xNi alloy exhibited several enhancement in catalytic activity comparing to polycrystalline Pt. [194-195] The active single crystal $Pt_3Ni(111)$ surface is reported to enhance ORR activity in Pt_xNi alloy. [196] The Ni_3Pt catalyst in this work was proved to be efficient in OER process and ORR process by rotating disk electrode (RDE) technique. Our previous works on Pt-Gd[21] and Pt-Cu[194] also prove that the Pt alloy catalyst is essential in improving ORR activity.

The Ni_3Pt was deposited on nickel foam by pulsed laser deposition (PLD). [197] This technique is common among physical vapor depostion (PVD) techniques. The ZAB fabricated by this air

cathode (denoted as Ni@Ni_3Pt) can perform at relatively low overpotential (<0.62V) for 478 cycles (10 minutes each cycle). The low overpotential is encouraging to improve round-trip efficiency of air batteries. The low overpotential and charge voltage (<1.7 V) can be attributed to the excellent catalytic of Ni_3Pt catalyst and the deposition method, as PLD can produce a porous film with very strong adhesion to the substrate.

6.2 Experimental

Synthesis of Ni_3Pt on Ni foam by PLD: The targets were made by sintering a pressed mixture of platinum powder (<40 nm, Sigma) and nickel powder (−40 mesh, Sigma) according to the element stoichiometry at 700 °C for 6 h in argon gas. The laser outputs 248 nm wavelength, 30 ns pulses at a frequency that may be chosen between 1 and 10 Hz. The energy of this pulse is determined by choosing the pumping high voltage (HV) of the laser. The laser HV ranges from 24 to 32 kV and, depending on the state of the gas medium, will produce energies in the pulse between 400 and 1200 mJ. The rectangular output pulse of the laser has dimensions of ≈30 mm × 12 mm. The substrates for deposition include nickel foam to get air electrode, TEM grids convenient for TEM operation, and glassy carbon electrode to test RDE performance.

Characterization: The corroded zinc anode was characterized by X-ray powder diffraction (XRD; GBC MMA) with Cu Kα radiation that was operated over a 2θ range of 20°–70°. The morphological studies were performed by field emission scanning electron microscopy (FE-SEM; JEOL-JSM-7500). Transmission electron microscopy (TEM) energy-dispersive X-ray spectroscopy (EDS) were used to investigate the Ni_3Pt film on nickel foam. XPS experiments were carried out on a VG Scientific ESCALAB 2201XL instrument using aluminum Kα X-ray radiation. XPS spectral analysis was conducted using XPS Peak-fit software. In this study, the BET measurements were conducted on a Quantachrome Nova 1000 nitrogen gas analyser, and

an Autosorb-iQ-Cx nitrogen adsorption instrument was used to determine the specific surface area of the synthesized powders.

Electrochemical measurements: All the cells with coin cell (CR2032) type were assembled, using the Ni@Ni_3Pt as cathode, a glass fibre separator, a polished zinc foil anode, and an aqueous electrolyte containing 6 M KOH + 0.2 M $Zn(Ac)_2$. For CV testing, the cells were sealed in a self-designed bottle. Then, the bottle was filled with O_2. The CVs were obtained between 0.7 V and 2.1 V at a scan rate of 0.2 mV s^{-1}. In these tests, Ni@Ni_3Pt and Ni@(Pt/C+IrO_2) acted as the working electrode. Ni@(Pt/C+IrO_2) was prepared by drop casting 50 wt% Pt/C-50 wt% IrO_2 on nickel foam (the loading was 1 mg cm^{-2}). On the other hand, zinc foil served as both counter and reference electrode. All battery tests were carried out on LAND CT 2001A multi-channel battery testers at room temperature in oxygen atmosphere. All the potentials throughout this paper are referred to the potential of the Zn/Zn^{2+} standard couple.

Catalyst performance: The aqueous electrochemical tests involving a rotating disk electrode (RDE) were carried out using a computer-controlled potentiostat (Biological VMP3) with a typical three-electrode cell, including a platinum wire as the counter electrode and an Ag/AgCl (saturated KCl filled) electrode as the reference electrode. The working electrodes were glassy carbon (GC) disk electrodes (5 mm in diameter) loaded with the respective active material inks. The details of preparation can be found in our previous works. [53] The detailed kinetic analysis

was conducted according to Koutecky-Levich plots

$$\frac{1}{j} = \frac{1}{j_k} + \frac{1}{B\omega^{0.5}} \quad (1)$$

where j is the current density, j_k is the kinetic current, and B is the Levich slope, which is given by

$$B = 0.2nF(D_{O_2})^{2/3}v^{-1/6}C_{O_2} \quad (2)$$

Here, n is the number of electrons transferred in the reduction of one O_2 molecule, F is the Faraday constant (F = 96 485 C mol^{-1}), D_{O_2} is the diffusion coefficient of O_2 (D_{O_2} = 1.9 × 10^{-5} cm^2 s^{-1}), ν is the kinematic viscosity for KOH (v = 0.01 cm^2 s^{-1}), and C_{O_2} is the concentration of O_2 in the solution (C_{O_2} = 1.2 × 10^{-6} mol cm^{-3}). The constant 0.2 is adopted when the rotation speed is expressed in rpm. According to Equations (1) and (2), the number of electrons transferred (n) can be obtained from the slope of the Koutecky–Levich plot of j^{-1} versus $\omega^{-1/2}$.

Flexible ZAB assembly: A polished zinc foil (0.25 mm thickness) was used as anode. The air electrode was Ni@Ni$_3$Pt mentioned above. The gel polymer electrolyte was prepared as follows: 1.0 g polyvinyl alcohol (PVA) powder (Sigma) was dissolved in 10.0 mL deionized water at 95 ^{o}C under magnetic stirring for 2.0 h. Then 1.0 mL of 18.0 M KOH filled with 0.20 M Zn(Ac)$_2$ was added, and the electrolyte solution was kept stirring at 95 ^{o}C for 40 min. Then the solution was freezed, and then thawed at room temperature. The procedure was repeated

twice to form gel electrolyte. Then the flexible ZAB was assembled with air electrode Ni@Ni_3Pt and zinc foil placed on the two sides of PVA gel.

6.3 Results and discussion

6.3.1 Structure and morphology

The scheme in **Figure 6.1a** illustrates the fabrication process of Ni@Ni_3Pt. The element stoichiometry 3:1 of Nickel versus Platinum is based on the powder mixture ratio of Nickel versus Pt.

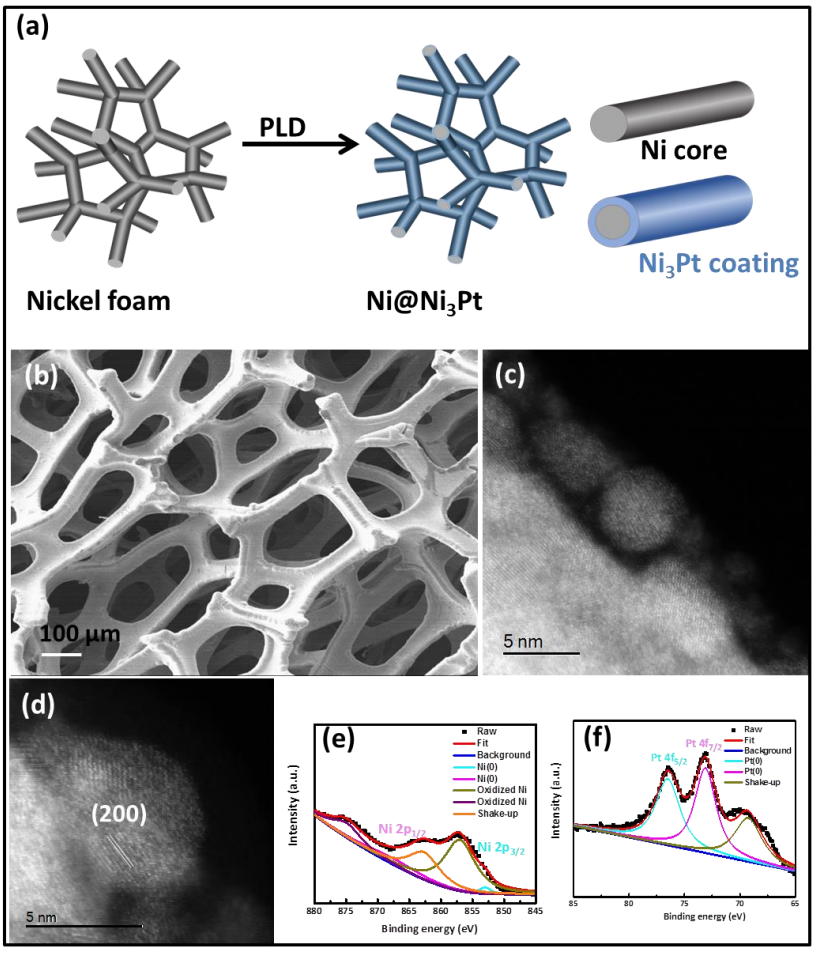

Figure 6.1 (a) PLD coating process to form Ni@Ni_3Pt (b) FESEM image of Ni@Ni_3Pt; (c) HRTEM image of Ni_3Pt alloy PTF; (d) HRTEM image of Ni_3Pt polyhedron crystals; XPS spectra of the electron binding energies for (e) Ni 2p and (f) Pt 4f in Ni@Ni_3Pt.

Firstly the nickel foam was cleaned thoroughly with acetone and ethanol and dried overnight in vacum oven at 80^{o}C. Then, the nickel foam was transfered to PLD chamber to prepare Ni@Ni_3Pt. The PLD coating was expected to form a layer of Ni_3Pt on nickel foam which created a core-shell structure of Ni_3Pt around Ni core like in schematic illustration in Figure 6.1a. Field emission scanning electron microscopy (FESEM) and high resolution transmission electron microscopy (HRTEM) were used to analyse the structure of Ni@Ni_3Pt. Figure 6.1b shows the 3D porous network of Ni@Ni_3Pt. Figure 6.1c clearly shows that the film contains many small polyhedon Ni_3Pt nano crystals. The Ni_3Pt (200) plane is observed in Figure 6.1d which agree with the $PtNi_3$ reported by Chen et al.[198] The TEM energy dispersive spectroscopy (EDS) shows clearly the presence of Pt and Ni in Figure 6.2a-e. The elements Ni and Pt show a similar homogeneous distribution over the entire area and the entire phase is a single alloy phase, with elements ratio of ≈3:1. Meanwhile, the whole area indicates a single alloy phase. The chemical binding energy of the Ni 2p signal (observed at 867.5 and 853.0 eV) and Pt 4f signal (observed at 76.6 and 73.1 eV) in Figure 6.1e and Figure 6.1f also indicate the coexistence of both metals. The reference of Ni-Pt X-ray photoelectron spectroscopy (XPS) is based on the Cao et al's. [199] The surface area of this catalyst was measured by Brunauer–Emmett–Teller (BET). From the BET isotherm in Figure 6.2f, the surface area is estimated to be 1359.8 m^2 g^{-1} which is a little lower than the 1663 m^2 g^{-1} value of N and P co-doped mesoporous nanocarbon (NPMC) foams catalyst reported by Liming Dai's group.[200]

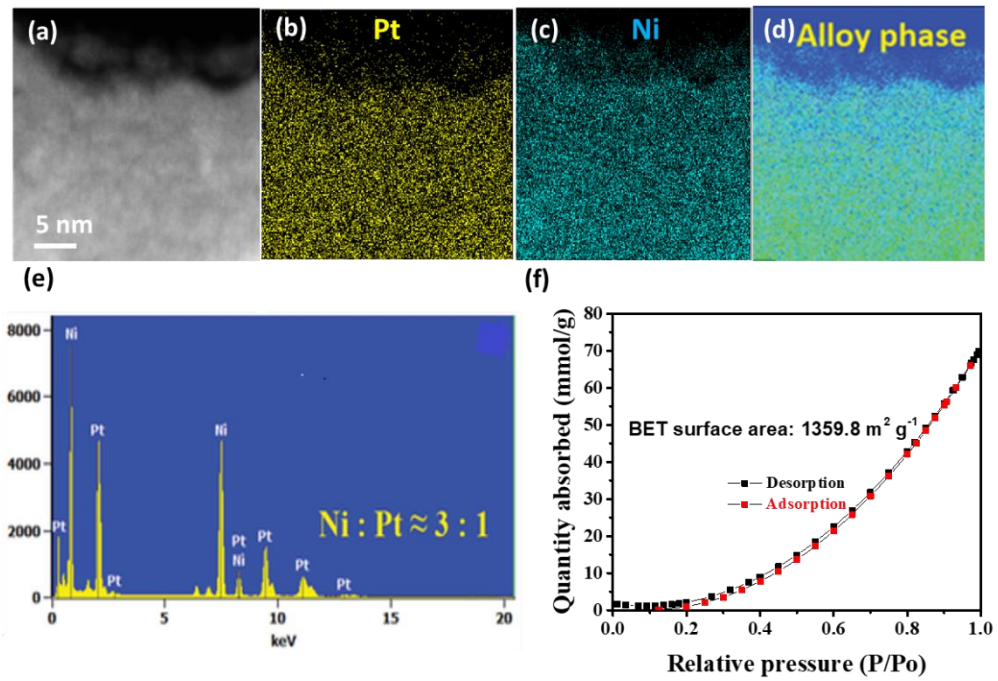

Figure 6.2 (a) TEM image at Pt_3Ni film; TEM EDS mapping of (b) Pt, (c) Ni elements; (d) alloy phase; (e) EDS spectrum of the film layer with the presence of Pt vs Ni; (f) N_2 adsorption-desorption isotherm.

6.3.2 Electrochemical characterization

The ORR and OER activities of Ni_3Pt, carbon super P were measured by rotating disk electrode (RDE) in O_2 saturated 0.1 M KOH electrolyte at a scan rate of 10 mV s^{-1}.

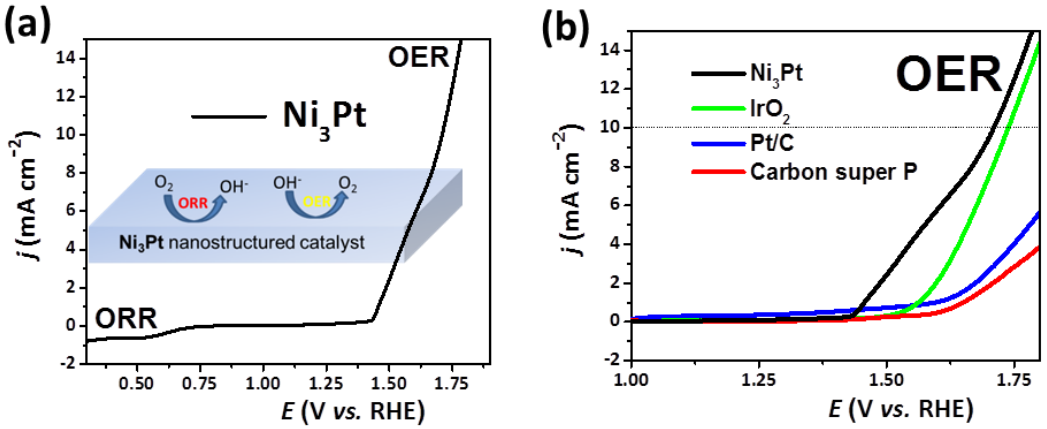

Figure 6.3 (a) RDE curves of Ni_3Pt alloy (b) OER curves of carbon, Pt/C, IrO_2, Ni_3Pt alloy at 1600 rpm in 0.1 M KOH. RHE: reversible hydrogen electrode.

The RDE curves in **Figure 6.3**a confirm the electrocatalystic performance of Ni_3Pt.[201] The electron transfer number per oxygen molecule (n) for ORR was determined from the RDE curves of Ni_3Pt alloy according to Koutechy-Levich (K-L) equation (details can be found in the experimental section). [202-204]The high catalytic activity of Ni_3Pt can be attributed to the addition of Ni to Pt crystal structure which increase the ORR activity in Pt_xNi alloy. [196] Figure 6.3b shows the rapidly increased anodic current above 1.43 V of Ni_3Pt associated with OER. As the reference, the standard OER catalyst (IrO_2) was used to compare peformance with Ni_3Pt alloy, and found that Ni_3Pt exhibited the lower onset potential than IrO_2. In an O_2 saturated aqueous system [6 M KOH + 0.2 M $Zn(Ac)_2$], as shown in **Figure 6.4**, the cyclic voltamogarm (CV) curves of Ni@Ni_3Pt and Ni@(Pt/C+IrO_2) were collected. Compared with Ni@(Pt/C+IrO_2), Ni@Ni_3Pt shows similar ORR and OER potentials in O_2-saturated electrolyte, which indicate that Ni_3Pt features bifunctional catalyst performance in the anodic and cathodic scan process in an O_2-saturated aqueous system. Generally, this Pt alloy skeleton-structured composite allows optimization of the surface electronic structure, weakening its binding to the O-containing reaction intermediates and maximizing the ORR activity. [205]

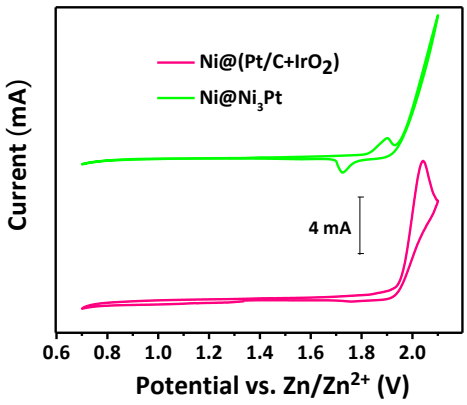

Figure 6.4 CV curves of Ni@(Pt/C+IrO_2) & Ni@Ni_3Pt in aqueous system (6 M KOH + 0.2 M $Zn(Ac)_2$).

Finally, the air-electrode Ni@Ni_3Pt was used as the air electrode for rechargeable ZAB, the kinetics is mainly limited by the cathode reaction [206]:

$$O_2 + H_2O + 4e^- \underset{OER}{\overset{ORR}{\rightleftarrows}} 4OH^-$$

A ZAB with Ni@Ni_3Pt as its air cathode was fabricated; the cell components are shown in **Figure 6.5**a.

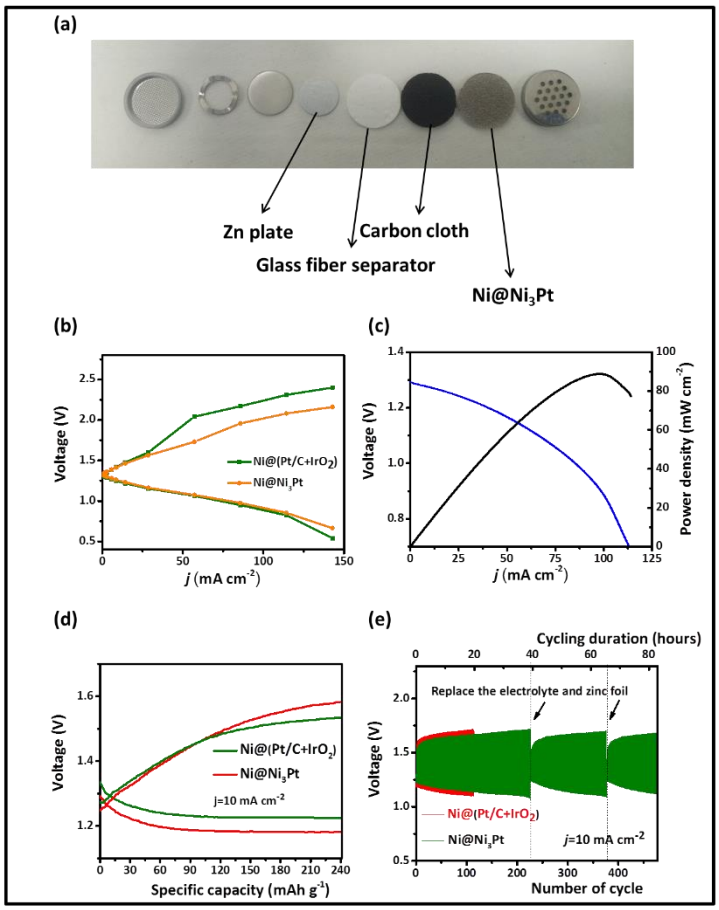

Figure 6.5 (a) Image of the components used for assembling of coin cell (CR2032) type; Zn plate, glass fiber carbon cloth (CC) and **Ni@Ni_3Pt** were served as anode, separator, GDL and cathode, respectively. (b) Battery voltages measured at different current densities (*j*); (c) Battery voltage and power density of Ni@Ni_3Pt versus *j*; (d) Galvanostatic discharge/charge measured at the 1st cycle; (e) Battery voltages versus number of cycle and time (each cycle include 5 minutes of discharge and 5 minutes of charge).

In **Figure 6.6**, three coin cells in series show open potential of 3.93 V, which can power a small red light.

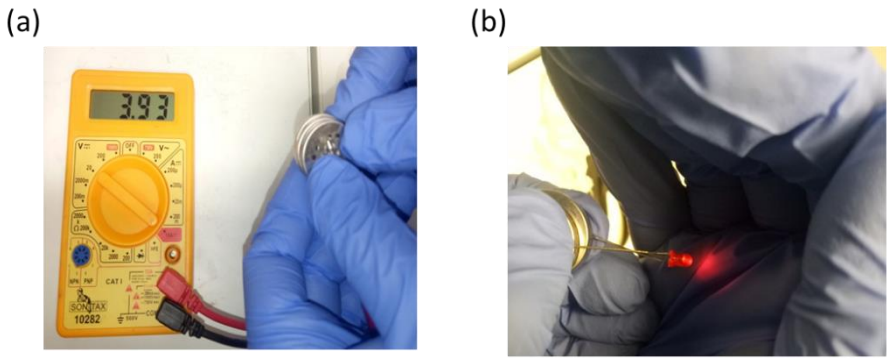

Figure 6.6 (a) Image of three-cell zinc-air battery, showing open circuit voltage of 3.93 V; (b) Photo of red LED powered by the zinc-air device.

The battery voltages measured at different current density is presented in Figure 6.5b. It clearly reveals that the Ni@Ni_3Pt cathode has the lower overpotential than Ni@(Pt/C+IrO_2) at any current density from 0 to 150 mA cm^{-2}. Battery voltage is above 1 V at the high current density of 50 mA cm^{-2}. The battery voltage and the power density are shown in Figure 6.5c. It can be seen that this battery can operate with the max power density as 90 mW cm^{-2} at the current density of 100 mA cm^{-2}. This value is higher than the max power density of NCNT/$Co_xMn_{1-x}O$ cathode (81 mW cm^{-2}) reported in Liu et al's. [207] The discharge/charge curve of Ni@Ni_3Pt at the first cycle is given in Figure 6.5d. Ni@Ni_3Pt shows a slightly higher open circuit potential (1.31 V) than those of the state-of-art commercial Pt/C and IrO_2 catalyst (1.29 V). In addition to the excellent charge and discharge capabilities, ZAB with Ni@Ni_3Pt as its air cathode showed good rechargeability (Figure 6.5e), evidenced by 478 discharge/charge cycles over a duration of 79 h (6 cycles for 1h), which ran at lower overpotential than ZAB using Pt/C and IrO_2 catalyst. The performance of Ni@Ni_3Pt catalyst is comparable to $CuCo_2O_4$@C reported by Wang et al [208], which also outperformed Pt/C and IrO_2. As shown in Figure 6.5e, the discharge/charge voltage was stable for almost 80 h, and the discharge/charge voltage could be

recovered with the electrolyte and zinc replaced. It can be observed from **Figure 6.7**a that the flexible cell include 4 layers of Ni@Ni_3Pt, carbon cloth, PVA gel electrolyte and zinc foil. Figure 6.7b and figure 6.7c show the fresh zinc electrode and a corroded zinc electrode. It can be seen in Figure 6.7c that zinc is corroded and there is a white compact layer of zinc hydroxide. XRD pattern in **Figure 6.8c** showed the presence of zinc hydroxide in the corroded electrode.

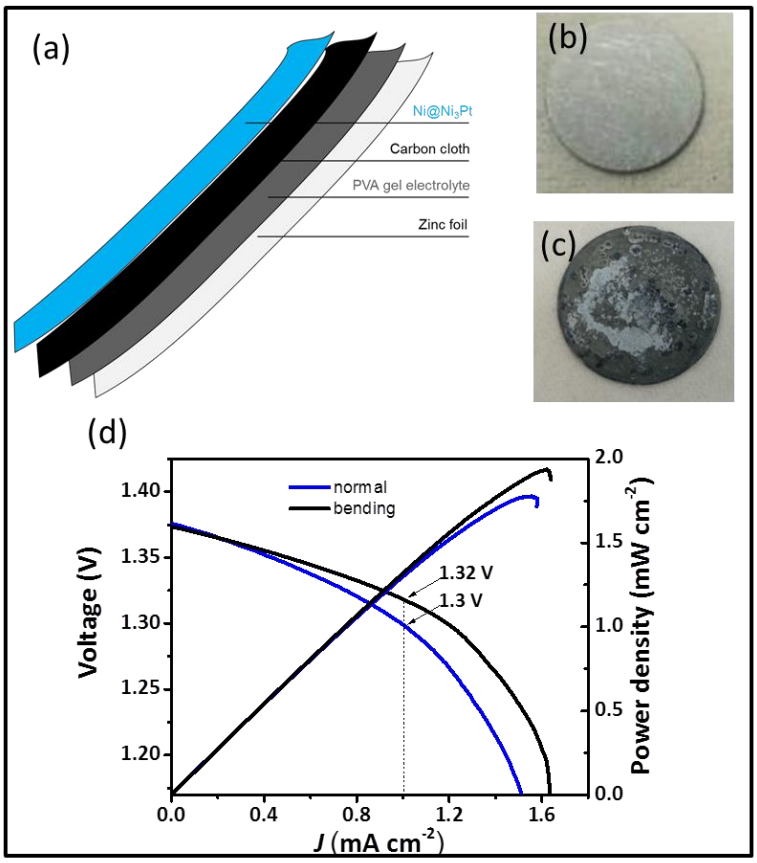

Figure 6.7 (a) Schematic illustration of the flexible ZAB;(b) fresh zinc electrode;(c) corroded zinc foil after 220 cycles;(d) Battery voltage and power density of the single flexible cell as a function of current density at normal and bending condition.

Figure 6.7d shows the battery voltage and power density versus the current density. It can be seen that the flexible cell reach the max current density of 2 mW cm^{-2} at the current density of 1.6 mA cm^{-2}. For the current density at 1 mA cm^{-2}, the open voltage of the bending cell is 1.32 V and the open voltage of the normal cell is 1.3 V.

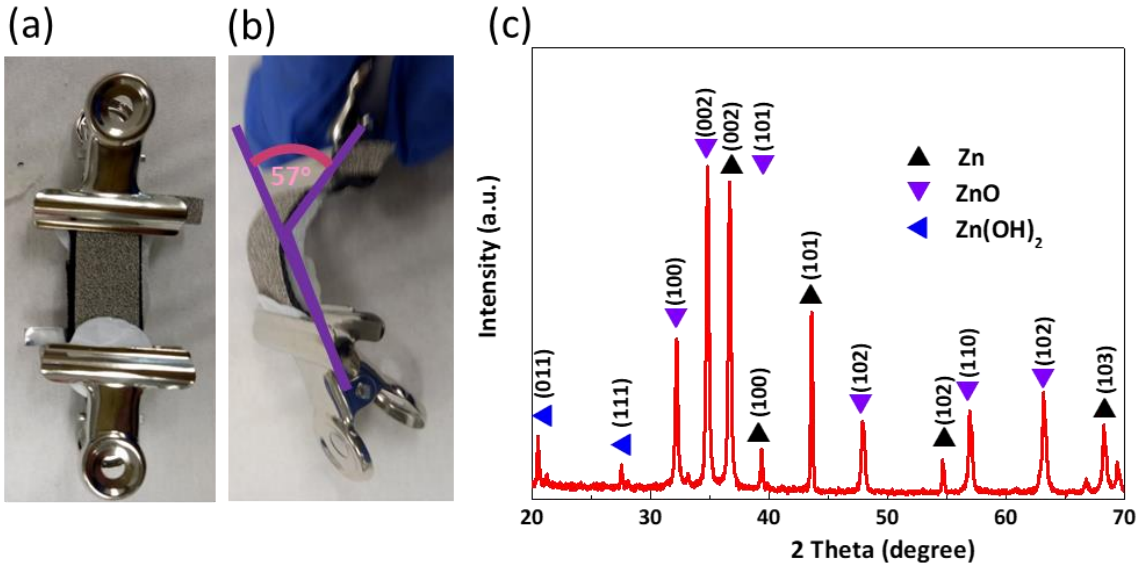

Figure 6.8 (a) flexible cell in normal state;(b) flexible cell bended to 57°(c) XRD pattern of the cycled zinc electrode with Zn (JCPDS 04-0831); $Zn(OH)_2$ (JCPDS 38-0385); ZnO (JCPDS 036-1451).

Figure 6.8a shows the flexible cell in normal condition and Figure 6.8b shows the cell bended to 57°. The phase of ZnO and $Zn(OH)_2$ were confirmed by XRD in Figure 6.8c. From the XRD pattern in Figure 6.8c, we can see the diffraction peaks of 3 materials which are zinc, zinc oxide and zinc hydroxide. It confirms that the zinc electrode corroded to zinc oxide and zinc hydroxide after battery cycling. Because of the zinc corrosion, zinc electrode have to be replaced after 220 cycles. After the replacement, battery lasted for another 154 cycles. The second replacement helped battery operate for 104 cycles. After the replacement of zinc, the battery discharge and charge voltage return to its originial value (1.20 V and 1.55 V) which indicate that the capacity is unchanged after zinc replacement. The replacement of zinc and electrolyte is common and it was also reported by Cheng et al. [209] From the cycling curve [Figure 6.5e], the overpotential always stays lower than 0.62 V, and the charge voltage is below 1.7 V. These overpotential and charge potential are the best ever reported among precious materials (listed in **Table 6.1**). This strongly indicates a high bifunctional activity and excellent stability of $Ni@Ni_3Pt$ catalyst, which is essential for rechargeable ZAB.

Table 6.1 Performance of this work secondary ZAB compared with other noble metal catalysts and other significant electrocatalysts.

Catalyst material	**Electrolyte**	**Charge potential (V)**	**Charge/ discharge overpotential (V)**	**Cycling condition (mA cm^{-2})/(mA g^{-1})**	**Stability**	**Ref**
Ni_3Pt on Ni foam	6 M KOH + 0.2 M $Zn(Ac)_2$	**1.7**	**0.31**	10	10 min/cycle for 478 cycles (up to 79 hours), overpotential increased to 0.62 V	This work
Ag-Cu on Ni foam	6 M KOH + 0.2 M $ZnCl_2$	2.05	0.96	20	20 min/cycle for 100 cycles with neligible voltage change	[210]
Pd_3Pb	6 M KOH + 0.2 M $ZnCl_2$	2.1	0.72	10	240 min/cycle for 137 cycles, overpotential increased to 0.86 V	[211]
RuO_2-MCNA	6 M KOH	2	0.8	4	120 min/cycle for 80 cycles with neligible voltage change	[212]
Ag-Cu nanoalloys on Ni foam	6 M KOH + 0.1 M $Zn(Ac)_2$	2.2	1.12	20	30 min/cycle for 252 cycles with neligible voltage change	[213]
Ag decorated $LaMnO_3$ nanorod/graphene	6 M KOH	2	0.86	25	60 min/cycle for 80 cycles, overpotential increased to 0.95 V	[214]
Atomically coupled Pt nanoparticles (NPs) and single-crystal (SC) CoO nanorods (NRs)	3 M KOH + 0.2 M $Zn(Ac)_2$	2.2	1.2	5 mA cm^{-2} for discharge and 10 mA cm^{-2} for charge	30 cycles with neligible voltage change	[215]
NGM-Co	6 M KOH + 0.2 M $ZnCl_2$	2	1	2	20 min/cycle for 180 cycles , overpotential increased to 1.12 V	[209]
CoO/N-CNT+NiFe LDH	6 M KOH + 0.2 M $Zn(Ac)_2$	2	0.7	20	10 cycles with negligible voltage change	[216]
N and P co-doped porous carbon (NPMC)	6 M KOH	2.25	0.95	2	10 min/cycle for 600 cycles	[200]

NiCo2O4/Ni F@C	6 M KOH + 0.2 M $Zn(Ac)_2$	2	1	5	30 min/cycle for >5000 cycles	[217]
CuCo2O4@ C	6 M KOH	1.9	0.79	10	160 cycles for 80 h	[208]
PC and QAFC membranes	1 M KOH in nanoporous cellulose membrane	2	0.8	250 mA g^{-1}	60 min/cycle for 1000 mins	[218]

From Table 6.1, Ni@Ni_3Pt electrode exhibits the lowest charge potential of 1.7 V. We can see that for other precious materials such as atomically coupled Pt [215] and CoO nano-rods, the Ag based catalysts [210, 213-214], and Pd_3Pb [211] the charge potential is between 2 V and 2.2 V. Compared to others reported catalyst for rechargeable zinc air battery, our materials (Ni@Ni_3Pt) performs the lowest charge potential. If we look at the overpotential, other materials show the value from 0.7 V to 1.2 V. The Ni@Ni_3Pt electrode reduces the overpotential to 0.62 V which is better than any reported works.

A flexible device using Ni@Ni_3Pt as air cathode is demonstrated in **Figure 6.9** with flexible zinc foil as anode, carbon cloth as gas diffusion layer (GDL), and alkaline gel electrolyte.

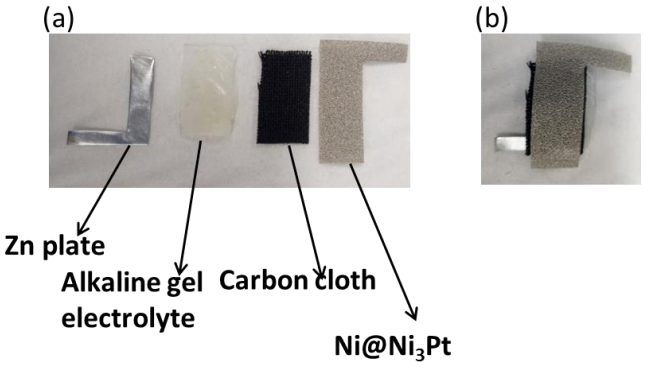

Figure 6.9 (a) Schematic diagram of a flexible zinc–air battery device including Zn plate, alkaline gel electrolyte, carbon cloth (CC) and **Ni@Ni_3Pt** served as anode, separator, GDL and cathode, respectively; (b) a stacked flexible cell battery.

The alkaline poly(vinyl alcohol) (PVA) gel electrolyte is fabricated with KOH, $Zn(Ac)_2$, and PVA in deionized water (see details in the experiment section, delivering considerable ionic conductivity and mechanical flexibility for ZAB). The two clips were used to hold all component of the flexible battery as shown in Figure 6.8a. The bending condition at 57^o is exhibited in Figure 6.8b. Figure 6.7d exhibits the battery voltage as a function of current density under the normal and bending condition. The voltage of the battery remained relatively unchanged comparing the bending and the non-bending state. Significantly, the flexible device has the open potential of 1.375 V. At the current density of 1 mA cm^{-2}, the bending battery can operate at 1.32 V and non bending at 1.3 V. The higher operating voltage of the bending state can be attributed to the better compression of the whole battery under curving condition than in the normal state. These results reveal that the Ni@Ni_3Pt catalyst has attractive potential in the rechargeable, flexible ZAB and wearable devices. Particularly, in addition to the optimization of cathode catalysts, strong efforts are also required to develop stable Zn anodes, [219] flexible [220] and highly ionic conductive electrolytes for the practical applications.

6.4 Summary

In conclusion, Ni_3Pt deposited on 3D microporous nickel foam (Ni@Ni_3Pt) by PLD can serve as an integrated air electrode for ZAB. Ni_3Pt demonstrates excellent catalytic activity, owing to highly efficient Pt-Ni alloy catalyst activity. The Ni_3Pt catalyst exhibits good ORR/OER bifunctional activities and impressive performances in rechargeable ZAB. Rechargeable ZAB (coin-cell type) was assembled using Ni@Ni_3Pt as cathode, delivering a maximum power density at 90 mW cm^{-2} and a stable discharge voltage (>1.09 V) at 10 mA cm^{-2}. The ZAB made by Ni@Ni_3Pt as air cathode was able to steadily cycle for 478 cycles (>79 hours) at a current density of 10 mA cm^{-2} which is comparable to other reported for ZABs. Moreover, the

Ni@Ni_3Pt is integrated into a rechargeable flexible ZAB showing impressive performances. A high open-circuit voltage of 1.375 V, and a high operating voltage of 1.32 V at 1.0 mA cm^{-2} under bending can be achieved. As a result, this work provides a promising technique in the future ZAB research to prepare high-efficient electrocatylist on porous substrate. The application in rechargeable coin-cell type and flexible ZAB also paves a new way for the development of high-efficient, cost-effective, and environmentally friendly flexible energy conversion and storage devices.

Chapter 7 Conclusion and Research Outlook

7.1 General conclusion

In this doctoral work, the two types of metal-air batteries, including the lithium-oxygen battery and the rechargeable zinc-air battery have been studied. The synthesis, physical characterization, and electrochemical performance of many nanostructured electrocatalysts for air batteries were researched carefully. In the case of $LaNi_{0.9}Cu_{0.1}O_3$ nanosheets, the effects of the porous structure on the catalytic activity of the electrocatalyst and the abundant catalytic active sites for Li-O_2 batteries were investigated. TiN nanorods decorated with Pt_3Cu nanoparticles were also explored as electrocatalysts and were found to achieve high capacity, high round-trip efficiency, and excellent cycling performance in Li-O_2 batteries. Additionally, an air cathode consisting of porous Ni_3Pt on Ni foam has been reported for application in rechargeable ZAB. The Ni@Ni_3Pt air electrode exhibited the lowest charge potential and overpotential among other recently reported catalysts. Based on the work presented in this thesis, these findings can broaden our knowledge in the field of electrocatalysts for the Li-O_2 battery and the rechargeable zinc air battery.

The development of the Li-O_2 battery began with $LaNi_{0.9}Cu_{0.1}O_3$ decorated on Ni foam. The $LaNi_{0.9}Cu_{0.1}O_3$ nanosheets were fabricated by hydrothermal method, which can act as an efficient bifunctional catalyst for the ORR and OER in Li-O_2 batteries. This porous nanosheet structure shows favourable rechargeability and excellent energy efficiency, facilitating rapid O_2 and electrolyte diffusion, as well as forming a continuous conductive network throughout the whole energy conversion process.

A novel composite of Pt_3Cu nanoparticles loaded onto TiN nanorods (TiN@Pt_3Cu) was synthesized by a facile approach, in which the TiN forms a continuous conductive network connecting the Pt_3Cu electrocatalyst nanoparticles together to facilitate good electrochemical performance. The Pt_3Cu electrocatalyst presents favourable rechargeability, and good phase and morphology stability in Li-O_2 batteries. Excellent discharge/charge performance is also reported. Hence, this TiN@Pt_3Cu composite is promising for use as a cathode electrocatalyst material for Li-O_2 batteries.

Ni_3Pt thin film loaded on Ni foam as an integrated electrode for the rechargeable zinc air battery (ZAB) was also reported. The air electrode showed the lowest charge potential and overpotential among other recently reported catalysts. A rechargeable ZAB (coin-cell type) was assembled using Ni@Ni_3Pt as cathode, delivering a maximum power density of 90 mW cm^{-2} and a stable discharge voltage (> 1.09 V) at 10 mA cm^{-2}. All of this high performance is based on the high catalytic activity of the Ni_3Pt film. As a result, this composite is a promising bifunctional electrocatalyst for rechargeable ZAB with low charge potential and low overpotential. Its application in rechargeable coin-cell type and flexible ZABs also opens up a new pathway for the development of highly-efficient, cost-effective, and environmentally friendly flexible energy conversion and storage devices.

In conclusion, a careful study was carried on various catalyst materials such as Ni@$LaNi_{0.9}Cu_{0.1}O_3$, TiN@Pt_3Cu, and Ni@Ni_3Pt applied as air cathodes for the lithium-oxygen battery and the rechargeable zinc-air battery. It is concluded that porous nanostructures will exhibit a high full discharge capacity. This is because the high surface area of these materials can provide plenty of space for Li_2O_2 formation, as well as favouring the gas diffusion in the cathode. Both an oxide material ($LaNi_{0.9}Cu_{0.1}O_3$) and noble metal based materials (Pt_3Cu, Ni_3Pt) were studied in this PhD thesis. The use of oxide or alloying transition metal with Pt materials can help to reduce the cost of pure Pt catalyst.

7.2 Outlook

Metal-air batteries, including the Li-O_2 battery and the rechargeable zinc-air battery are becoming one of the most promising energy storage and conversion technologies because of their ultrahigh energy density. They are, in fact, still in the infant stage of development. Overcoming the challenge to improve the performance of these batteries involves developing catalysts with low overpotential and long-term cycling stability. This doctoral work has been mainly focused on the synthesis and characterization of nanostructured cathode electrocatalysts for both the lithium-oxygen battery and the rechargeable zinc-air battery. Based on the work presented in this thesis, the reported strategies to synthesize nanostructured electrocatalysts could be expected to raise general interest and have an influence on the development of potential electrocatalytic materials for metal-air batteries. As rechargeable Li-O_2 batteries and zinc-air batteries are still in the research stage, the production of commercial rechargeable metal-air batteries still has a long way to go.

The outcomes of this Phd study are mainly focused on the development of new catalyst. $LaNi_{0.9}Cu_{0.1}O_3$ is the oxide catalyst, which is more cost effective than the standard noble metal such as Pt/C and IrO_2. Pt_3Cu was reported to outperform the standard Pt/C with the alloying of

Cu to Pt material. Ni_3Pt is also another Pt alloy, which exhibited the excellent low charge potential and the small overpotential in rechargeable ZAB. However, the problem with the ambient gas was not touched in this Phd study. The Li-O_2 batteries in this research operate in pure O_2 gas. Therefore, the next research could be advancing the new membranes, which can filter the CO_2, N_2, and moisture in the ordinary condition.

The rechargeable ZAB in this Phd study peforms the excellent low charge potential and the small overpotential compared with other reported researchs. However, the problems with zinc anode corosion limited the cycle performance of this battery, which make it is troublesome to replace zinc anode due to electrode decay. The future direction could be centered on developing the the protective layer for zinc metal, which still holds excellent charge transfer property in alkaline electrolytes.

REFERENCES

1. Jang-Soo, L.; Sun, T. K.; Ruiguo, C.; Nam-Soon, C.; Meilin, L.; Tae, L. K.; Jaephil, C., Metal-Air Batteries: Metal–Air Batteries with High Energy Density: Li–Air versus Zn–Air (Adv. Energy Mater. 1/2011). *Advanced Energy Materials* **2011,** *1* (1), 2-2.

2. Q. Li, R. Cao, J. Cho and G. Wu, Nanostructured carbon-based cathode catalysts for nonaqueous lithium–oxygen batteries. *Physical Chemistry Chemical Physics*, **2014**, *16*, 13568-13582.

3. A. K. Thapa, K. Saimen and T. Ishihara, Pd / MnO2 Air Electrode Catalyst for Rechargeable Lithium/Air Battery. *Electrochemical and Solid State Letters*, **2010**, *13*, A165-A167.

4. Z. Yang, J. Zhang, M. C. W. Kintner-Meyer, X. Lu, D. Choi, J. P. Lemmon and J. Liu, Electrochemical energy storage for green grid. *Chem. Rev.*, **2011**, *111*, 3577-3613.

5. Ben & Jerry's Homemade Holdings Inc, Unilever, accessed 11th July 2019, <https://www.benjerry.com/whats-new/2017/12/electric-car-milestones>

6. P. G. Bruce, S. A. Freunberger, L. J. Hardwick and J.-M. Tarascon, Li-O_2 and Li-S batteries with high energy storage. *Nature Materials*, **2012**, *11*, 19-29.

7. Scrosati, B.; Hassoun, J.; Sun, Y.-K., Lithium-ion batteries. A look into the future. *Energy & Environmental Science* **2011,** *4* (9), 3287-3295.

8. IOR Petroleum Australia, accessed 14th March 2019, <http://web.archive.org/web/20100825042309/http://www.ior.com.au/ecflist.html>

9. Lu, J.; Li, L.; Park, J.-B.; Sun, Y.-K.; Wu, F.; Amine, K., Aprotic and Aqueous Li–O_2 Batteries. *Chemical Reviews* **2014,** *114* (11), 5611-5640.

10. Abraham, K. M.; Jiang, Z., A polymer electrolyte-based rechargeable lithium/oxygen battery. *Journal of the Electrochemical Society* **1996,** *143* (1), 1-5.

11. Débart, A.; Paterson, A. J.; Bao, J.; Bruce, P. G., α-MnO_2 nanowires: A catalyst for the O2 electrode in rechargeable lithium batteries. *Angewandte Chemie - International Edition* **2008,** *47* (24), 4521-4524.

12. Lee, H.; Kim, Y.-J.; Lee, D. J.; Song, J.; Lee, Y. M.; Kim, H.-T.; Park, J.-K., Directly grown Co_3O_4 nanowire arrays on Ni-foam: structural effects of carbon-free and binder-free

cathodes for lithium-oxygen batteries. *Journal of Materials Chemistry A* **2014,** *2* (30), 11891-11898.

13. Sun, B.; Munroe, P.; Wang, G., Ruthenium nanocrystals as cathode catalysts for lithium-oxygen batteries with a superior performance. *Scientific Reports* **2013,** *3*, 2247.

14. Liu, T.; Leskes, M.; Yu, W.; Moore, A. J.; Zhou, L.; Bayley, P. M.; Kim, G.; Grey, C. P., Cycling Li-O_2 batteries via LiOH formation and decomposition. *Science* **2015,** *350* (6260), 530-533.

15. Lim, H. D.; Song, H.; Kim, J.; Gwon, H.; Bae, Y.; Park, K. Y.; Hong, J.; Kim, H.; Kim, T.; Kim, Y. H.; Leprõ, X.; Ovalle-Robles, R.; Baughman, R. H.; Kang, K., Superior rechargeability and efficiency of lithium-oxygen batteries: Hierarchical air electrode architecture combined with a soluble catalyst. *Angewandte Chemie - International Edition* **2014,** *53* (15), 3926-3931.

16. Liu, W.; Rodriguez, P.; Borchardt, L.; Foelske, A.; Yuan, J.; Herrmann, A. K.; Geiger, D.; Zheng, Z.; Kaskel, S.; Gaponik, N.; Kötz, R.; Schmidt, T. J.; Eychmüller, A., Bimetallic aerogels: High-performance electrocatalysts for the oxygen reduction reaction. *Angewandte Chemie - International Edition* **2013,** *52* (37), 9849-9852.

17. Li, Q.; Xu, P.; Gao, W.; Ma, S.; Zhang, G.; Cao, R.; Cho, J.; Wang, H. L.; Wu, G., Graphene/graphene-tube nanocomposites templated from cage-containing metal-organic frameworks for oxygen reduction in Li-O_2 batteries. *Advanced Materials* **2014,** *26* (9), 1378-1386.

18. Li, L.; Chai, S.-H.; Dai, S.; Manthiram, A., Advanced hybrid Li-air batteries with high-performance mesoporous nanocatalysts. *Energy & Environmental Science* **2014,** *7* (8), 2630-2636.

19. Jung, H.-G.; Jeong, Y. S.; Park, J.-B.; Sun, Y.-K.; Scrosati, B.; Lee, Y. J., Ruthenium-Based Electrocatalysts Supported on Reduced Graphene Oxide for Lithium-Air Batteries. *ACS Nano* **2013,** *7* (4), 3532-3539.

20. Lu, Y.-C.; Xu, Z.; Gasteiger, H. A.; Chen, S.; Hamad-Schifferli, K.; Shao-Horn, Y., Platinum−Gold Nanoparticles: A Highly Active Bifunctional Electrocatalyst for Rechargeable Lithium−Air Batteries. *Journal of the American Chemical Society* **2010,** *132* (35), 12170-12171.

21. Luo, W.-B.; Gao, X.-W.; Shi, D.-Q.; Chou, S.-L.; Wang, J.-Z.; Liu, H.-K., Binder-Free and Carbon-Free 3D Porous Air Electrode for Li-O_2 Batteries with High Efficiency, High Capacity, and Long Life. *Small* **2016,** *12* (22), 3031-3038.

22. B. Scrosati, J. Hassoun and Y.-K. Sun, Lithium-ion batteries. A look into the future. *Energy & Environmental Science*, **2011**, 4, 3287-3295.

23. X.-h. Yang, P. He and Y.-y. Xia, Preparation of mesocellular carbon foam and its application for lithium/oxygen battery. *Electrochemistry Communications*, **2009**, 11, 1127-1130.

24. Y. Li, J. Wang, X. Li, J. Liu, D. Geng, J. Yang, R. Li and X. Sun, Nitrogen-doped carbon nanotubes as cathode for lithium–air batteries. *Electrochemistry Communications*, **2011**, 13, 668-672.

25. G. Q. Zhang, J. P. Zheng, R. Liang, C. Zhang, B. Wang, M. Hendrickson and E. J. Plichta, Lithium–Air Batteries Using SWNT/CNF Buckypapers as Air Electrodes. *J. Electrochem. Soc*., **2010**, 157, A953-A956.

26. A. Debart, A. J. Paterson, J. Bao and P. G. Bruce, Alpha-MnO_2 nanowires: a catalyst for the O_2 electrode in rechargeable lithium batteries. *Angewandte ChemieInternational Edition*, **2008**, 47, 4521-4524.

27. H. Cheng and K. Scott, Carbon-supported manganese oxide nanocatalysts for rechargeable lithium–air batteries. *Journal of Power Sources*, **2010**, 195, 1370-1374.

28. A. Debart, J. Bao, G. Armstrong and P. G. Bruce, An O_{-2} cathode for rechargeable lithium batteries: The effect of a catalyst. *Journal of Power Sources*, **2007**, 174, 1177-1182.

29. Y. Cui, Z. Wen and Y. Liu, A free-standing-type design for cathodes of rechargeable Li–O_2 batteries. *Energy & Environmental Science*, **2011**, 4, 47274734

30. H. Cheng and K. Scott, Selection of oxygen reduction catalysts for rechargeable lithium–air batteries—Metal or oxide?. *Applied Catalysis B-Environmental*, **2011**, 108, 140151.

31. S. S. Zhang, X. Ren and J. Read, Heat-treated metal phthalocyanine complex as an oxygen reduction catalyst for non-aqueous electrolyte Li/air batteries. *Electrochimica Acta*, **2011**, 56, 4544-4548.

32. X. Ren, S. S. Zhang, D. T. Tran and J. Read, Oxygen reduction reaction catalyst on lithium/air battery discharge performance. *Journal of Materials Chemistry*, **2011**, 21, 10118-10125.

33. J. Read, Characterization of the Lithium/Oxygen Organic Electrolyte Battery. *J. Electrochem. Soc.*, **2002**, 149, A1190-A1195.

34. J. Read, Ether-Based Electrolytes for the Lithium/Oxygen Organic Electrolyte Battery. *J. Electrochem. Soc.*, **2006**, 153, A96-A100.

35. J. Read, K. Mutolo, M. Ervin, W. Behl, J. Wolfenstine, A. Driedger and D. Foster, Oxygen Transport Properties of Organic Electrolytes and Performance of Lithium/Oxygen Battery. *J. Electrochem. Soc.*, **2003**, 150, A1351-A1356.

36. International Business Machines, accessed 14th March 2018, <http://www.ibmcom/smarterplanet/us/en/smart_grid/article/battery500.html>

37a. Girishkumar, G.; McCloskey, B.; Luntz, A. C.; Swanson, S.; Wilcke, W., Lithium−Air Battery: Promise and Challenges. *The Journal of Physical Chemistry Letters* **2010**, 1 (14), 2193-2203.

37b. Ding, F.; Xu, W.; Graff, G. L.; Zhang, J.; Sushko, M. L.; Chen, X.; Shao, Y.; Engelhard, M. H.; Nie, Z.; Xiao, J.; Liu, X.; Sushko, P. V.; Liu, J.; Zhang, J.-G., Dendrite-Free Lithium Deposition via Self-Healing Electrostatic Shield Mechanism. *Journal of the American Chemical Society* **2013,** *135* (11), 4450-4456.

37c. Qian, J.; Henderson, W. A.; Xu, W.; Bhattacharya, P.; Engelhard, M.; Borodin, O.; Zhang, J.-G., High rate and stable cycling of lithium metal anode. *Nature Communications* **2015,** *6*, 6362.

37d. Li, N.-W.; Yin, Y.-X.; Yang, C.-P.; Guo, Y.-G., An Artificial Solid Electrolyte Interphase Layer for Stable Lithium Metal Anodes. *Advanced Materials* **2016,** *28* (9), 1853-1858.

38. Zhang, J.; Zhao, Y.; Zhao, X.; Liu, Z.; Chen, W., Porous Perovskite $LaNiO_3$ Nanocubes as Cathode Catalysts for Li-O_2 Batteries with Low Charge Potential. *Scientific Reports* **2014**, 4, 6005.

39. D. Aurbach, Y. Gofer, M. Benzion and P. Aped, The behaviour of lithium electrodes in propylene and ethylene carbonate: Te major factors that influence Li cycling efficiency. *Journal of Electroanalytical Chemistry*, **1992**, 339, 451-471.

40. D. Aurbach, I. Weissman, A. Zaban and O. Chusid, Correlation between surface chemistry, morphology, cycling efficiency and interfacial properties of Li electrodes in solutions containing different Li salts. *Electrochimica Acta*, **1994**, 39, 51-71.

41. K. Takechi, T. Shiga and T. Asaoka, A Li–O2/CO2 battery. *Chemical Communications*, **2011**, 47, 3463-3465.

42. P. G. Bruce, Energy storage beyond the horizon: Rechargeable lithium batteries. *Solid State Ionics*, **2008**, 179, 752-760.

43. M. Armand and J. M. Tarascon, Building better batteries. *Nature*, **2008**, 451, 652-657.

44. M. A. Rahman, X. Wang and C. Wen, A review of high energy density lithium–air battery technology. *Journal of Applied Electrochemistry*, **2014**, 44, 5-22.

45. H. L. Wang, Y. Yang, Y. Y. Liang, G. Y. Zheng, Y. G. Li, Y. Cui and H. J. Dai, Rechargeable Li-O_2 Batteries with Covalently Coupled MnCo2O4-Graphene Hybrid as Oxygen Cathode Catalyst. *Energy & Environmental Science*, **2012**, 5, 7931-7935.

46. B. D. McCloskey, D. S. Bethune, R. M. Shelby, G. Girishkumar and A. C. Luntz, Solvents' Critical Role in Nonaqueous Lithium–Oxygen Battery Electrochemistry. *Journal of Physical Chemistry Letters*, **2011**, 2, 1161-1166.

47. G. Wu, N. H. Mack, W. Gao, S. G. Ma, R. Q. Zhong, J. T. Han, J. K. Baldwin and P. Zelenay, Nitrogen-doped graphene-rich catalysts derived from heteroatom polymers for oxygen reduction in nonaqueous lithium-O_2 battery cathodes. *Acs Nano*, **2012**, 6, 9764-9776.

48. Y. Chen, S. A. Freunberger, Z. Peng, F. Barde and P. G. Bruce, Li-O-$_2$ Battery with a Dimethylformamide Electrolyte. *Journal of the American Chemical Society*, **2012**, 134, 7952-7957.

49. D. Xu, Z. L. Wang, J. J. Xu, L. L. Zhang, L. M. Wang and X. B. Zhang, A stable sulfone based electrolyte for high performance rechargeable Li–O_2 batteries. *Chemical Communications*, **2012**, 48, 11674-11676.

50. Z. Zhang, J. Lu, R. S. Assary, P. Du, H.-H. Wang, Y.-K. Sun, Y. Qin, K. C. Lau, J. Greeley, P. C. Redfern, H. Iddir, L. A. Curtiss and K. Amine, *Journal of Physical Chemistry C*, **2011**, 115, 25535-25542.

51. Liang, Z.; Lu, Y.-C., Critical Role of Redox Mediator in Suppressing Charging Instabilities of Lithium–Oxygen Batteries. *Journal of the American Chemical Society* **2016,** *138* (24), 7574-7583.

52. T. V. Pham, H. P. Guo, W. B. Luo, S. L. Chou, J. Z. Wang, H. K. Liu, *J, Carbon- and binder-free 3D porous perovskite oxide air electrode for rechargeable lithium–oxygen batteries. Journal of Materials Chemistry A* **2017**, 5, 5283.

53. W.-B. Luo, T. V. Pham, H.-P. Guo, H.-K. Liu, S.-X. Dou, Three-Dimensional Array of TiN@Pt_3Cu Nanowires as an Efficient Porous Electrode for the Lithium-Oxygen Battery. *ACS Nano* **2017**, 11, 1747.

54. Scrosati, B.; Garche, J., Lithium batteries: Status, prospects and future. *Journal of Power Sources* **2010,** *195* (9), 2419-2430.

55. Peng, Z.; Freunberger, S. A.; Chen, Y.; Bruce, P. G., A Reversible and Higher-Rate Li-O_2 Battery. *Science* **2012,** *337* (6094), 563-566.

56. Xiao, J.; Mei, D.; Li, X.; Xu, W.; Wang, D.; Graff, G. L.; Bennett, W. D.; Nie, Z.; Saraf, L. V.; Aksay, I. A.; Liu, J.; Zhang, J.-G., Hierarchically Porous Graphene as a Lithium–Air Battery Electrode. *Nano Letters* **2011,** *11* (11), 5071-5078.

57. Guo, Z.; Li, J.; Xia, Y.; Chen, C.; Wang, F.; Tamirat, A. G.; Wang, Y.; Xia, Y.; Wang, L.; Feng, S., A flexible polymer-based Li–air battery using a reduced graphene oxide/Li composite anode. *Journal of Materials Chemistry A* **2018,** *6* (14), 6022-6032.

58. Liu, L.; Wang, J.; Hou, Y.; Chen, J.; Liu, H. K.; Wang, J.; Wu, Y., Self-Assembled 3D Foam-Like $NiCo_2O_4$ as Efficient Catalyst for Lithium Oxygen Batteries. *Small* **2016**, 12 (5), 602-611.

59. Wu, F.; Zhang, X.; Zhao, T.; Chen, R.; Ye, Y.; Xie, M.; Li, L., Hierarchical mesoporous/macroporous Co_3O_4 ultrathin nanosheets as free-standing catalysts for rechargeable lithium-oxygen batteries. *Journal of Materials Chemistry A* **2015,** *3* (34), 17620-17626.

60. Li, F.; Zhang, T.; Zhou, H., Challenges of non-aqueous Li-O_2 batteries: electrolytes, catalysts, and anodes. *Energy & Environmental Science* **2013,** *6* (4), 1125-1141.

61. Liu, Q.-C.; Xu, J.-J.; Xu, D.; Zhang, X.-B., Flexible lithium-oxygen battery based on a recoverable cathode. *Nat Commun* **2015,** *6*.

62. Gallant, B. M.; Mitchell, R. R.; Kwabi, D. G.; Zhou, J.; Zuin, L.; Thompson, C. V.; Shao-Horn, Y., Chemical and Morphological Changes of Li–O_2 Battery Electrodes upon Cycling. *The Journal of Physical Chemistry C* **2012**, 116 (39), 20800-20805.

63. McCloskey, B. D.; Speidel, A.; Scheffler, R.; Miller, D. C.; Viswanathan, V.; Hummelshøj, J. S.; Nørskov, J. K.; Luntz, A. C., Twin Problems of Interfacial Carbonate

Formation in Nonaqueous Li–O2 Batteries. *The Journal of Physical Chemistry Letters* **2012,** *3* (8), 997-1001.

64. Ottakam Thotiyl, M. M.; Freunberger, S. A.; Peng, Z.; Bruce, P. G., The Carbon Electrode in Nonaqueous Li–O_2 Cells. *Journal of the American Chemical Society* **2013,** *135* (1), 494-500.

65. Kong, D.; Luo, J.; Wang, Y.; Ren, W.; Yu, T.; Luo, Y.; Yang, Y.; Cheng, C., Three-Dimensional Co_3O_4@MnO_2 Hierarchical Nanoneedle Arrays: Morphology Control and Electrochemical Energy Storage. *Advanced Functional Materials* **2014,** *24* (24), 3815-3826.

66. Yuan, C.; Yang, L.; Hou, L.; Shen, L.; Zhang, X.; Lou, X. W., Growth of ultrathin mesoporous Co_3O_4 nanosheet arrays on Ni foam for high-performance electrochemical capacitors. *Energy & Environmental Science* **2012,** *5* (7), 7883-7887.

67. Liu, J.; Jiang, J.; Cheng, C.; Li, H.; Zhang, J.; Gong, H.; Fan, H. J., Co_3O_4 Nanowire@MnO_2 Ultrathin Nanosheet Core/Shell Arrays: A New Class of High-Performance Pseudocapacitive Materials (Adv. Mater. 18/2011). *Advanced Materials* **2011,** *23* (18), 2075-2075.

68. Li, J.; Zhao, Y.; Zou, M.; Wu, C.; Huang, Z.; Guan, L., An Effective Integrated Design for Enhanced Cathodes of Ni Foam-Supported Pt/Carbon Nanotubes for Li-O_2 Batteries. *ACS Applied Materials & Interfaces* **2014,** *6* (15), 12479-12485.

69. Jian, Z.; Liu, P.; Li, F.; He, P.; Guo, X.; Chen, M.; Zhou, H., Core–Shell-Structured CNT@RuO_2 Composite as a High-Performance Cathode Catalyst for Rechargeable Li–O_2 Batteries. *Angewandte Chemie International Edition* **2014,** *53* (2), 442-446.

70. Zhang, Z.; Su, L.; Yang, M.; Hu, M.; Bao, J.; Wei, J.; Zhou, Z., A composite of Co nanoparticles highly dispersed on N-rich carbon substrates: an efficient electrocatalyst for Li-O2 battery cathodes. *Chemical Communications* **2014,** *50* (7), 776-778.

71. Wang, M.; Qin, X.; Jiang, K.; Dong, Y.; Shao, M.; Cai, W.-B., Electrocatalytic Activities of Oxygen Reduction Reaction on Pd/C and Pd–B/C Catalysts. *The Journal of Physical Chemistry C* **2017,** *121* (6), 3416-3423.

72. Shui, J.-L.; Karan, N. K.; Balasubramanian, M.; Li, S.-Y.; Liu, D.-J., Fe/N/C Composite in Li–O_2 Battery: Studies of Catalytic Structure and Activity toward Oxygen Evolution Reaction. *Journal of the American Chemical Society* **2012,** *134* (40), 16654-16661.

73. Cui, C.; Gan, L.; Li, H.-H.; Yu, S.-H.; Heggen, M.; Strasser, P., Octahedral PtNi Nanoparticle Catalysts: Exceptional Oxygen Reduction Activity by Tuning the Alloy Particle Surface Composition. *Nano Letters* **2012,** *12* (11), 5885-5889.

74. Kim, B. G.; Kim, H.-J.; Back, S.; Nam, K. W.; Jung, Y.; Han, Y.-K.; Choi, J. W., Improved reversibility in lithium-oxygen battery: Understanding elementary reactions and surface charge engineering of metal alloy catalyst. *Scientific Reports* **2014,** *4*, 4225.

75. Suntivich, J.; May, K. J.; Gasteiger, H. A.; Goodenough, J. B.; Shao-Horn, Y., A perovskite oxide optimized for oxygen evolution catalysis from molecular orbital principles. *Science* **2011,** *334* (6061), 1383-1385.

76. Du, Z.; Yang, P.; Wang, L.; Lu, Y.; Goodenough, J. B.; Zhang, J.; Zhang, D., Electrocatalytic performances of $LaNi_{1-x}Mg_xO_3$ perovskite oxides as bi-functional catalysts for lithium air batteries. *Journal of Power Sources* **2014,** *265*, 91-96.

77. Hassoun, J.; Jung, H.-G.; Lee, D.-J.; Park, J.-B.; Amine, K.; Sun, Y.-K.; Scrosati, B., A Metal-Free, Lithium-Ion Oxygen Battery: A Step Forward to Safety in Lithium-Air Batteries. *Nano Letters* **2012,** *12* (11), 5775-5779.

78. Guo, Z.; Dong, X.; Wang, Y.; Xia, Y., A lithium air battery with a lithiated Al-carbon anode. *Chemical Communications* **2015,** *51* (4), 676-678.

79. Freunberger, S. A.; Chen, Y.; Peng, Z.; Griffin, J. M.; Hardwick, L. J.; Bardé, F.; Novák, P.; Bruce, P. G., Reactions in the Rechargeable Lithium–O2 Battery with Alkyl Carbonate Electrolytes. *Journal of the American Chemical Society* **2011**, 133 (20), 8040-8047.

80. Luo, W.-B.; Chou, S.-L.; Zhai, Y.-C.; Liu, H.-K., Self-assembled graphene and $LiFePO_4$ composites with superior high rate capability for lithium ion batteries. *Journal of Materials Chemistry A* **2014**, 2 (14), 4927-4931.

81. Chou, S.-L.; Wang, J.-Z.; Liu, H.-K.; Dou, S.-X., Rapid Synthesis of $Li_4Ti_5O_{12}$ Microspheres as Anode Materials and Its Binder Effect for Lithium-Ion Battery. T*he Journal of Physical Chemistry C* **2011**, 115 (32), 16220-16227.

82. Gao, X.-W.; Wang, J.-Z.; Chou, S.-L.; Liu, H.-K., Synthesis and electrochemical performance of LiV_3O_8/polyaniline as cathode material for the lithium battery. *Journal of Power Sources* **2012**, 220, 47-53.

83. Xu, J.; Chou, S.-L.; Gu, Q.-f.; Liu, H.-K.; Dou, S.-X., The effect of different binders on electrochemical properties of $LiNi_{1/3}Mn_{1/3}Co_{1/3}O_2$ cathode material in lithium ion batteries. *Journal of Power Sources* **2013**, 225, 172-178.

84. Gao, X.; Luo, W.; Zhong, C.; Wexler, D.; Chou, S.-L.; Liu, H.-K.; Shi, Z.; Chen, G.; Ozawa, K.; Wang, J.-Z., Novel Germanium/Polypyrrole Composite for High Power Lithium-ion Batteries. *Scientific Reports* **2014**, 4, 6095.

85. Peng, Z.; Freunberger, S. A.; Hardwick, L. J.; Chen, Y.; Giordani, V.; Bardé, F.; Novák, P.; Graham, D.; Tarascon, J.-M.; Bruce, P. G., Oxygen Reactions in a Non-Aqueous Li+ Electrolyte. *Angewandte Chemie International Edition* **2011**, 50 (28), 6351-6355.

86. Zhang, Z.; Lu, J.; Assary, R. S.; Du, P.; Wang, H.-H.; Sun, Y.-K.; Qin, Y.; Lau, K. C.; Greeley, J.; Redfern, P. C.; Iddir, H.; Curtiss, L. A.; Amine, K., Increased Stability Toward Oxygen Reduction Products for Lithium-Air Batteries with Oligoether-Functionalized Silane Electrolytes. *The Journal of Physical Chemistry C* **2011**, 115 (51), 25535-25542.

87. Oh, D.; Qi, J.; Lu, Y.-C.; Zhang, Y.; Shao-Horn, Y.; Belcher, A. M., Biologically enhanced cathode design for improved capacity and cycle life for lithium-oxygen batteries. *Nature Communications* **2013**, 4, 2756.

88. McCloskey, B. D.; Valery, A.; Luntz, A. C.; Gowda, S. R.; Wallraff, G. M.; Garcia, J. M.; Mori, T.; Krupp, L. E., Combining Accurate O_2 and Li_2O_2 Assays to Separate Discharge and Charge Stability Limitations in Nonaqueous Li–O_2 Batteries. *The Journal of Physical Chemistry Letters* **2013**, 4 (17), 2989-2993.

89. Hu, X.; Cheng, F.; Zhang, N.; Han, X.; Chen, J., Nanocomposite of Fe_2O_3@C@MnO_2 as an Efficient Cathode Catalyst for Rechargeable Lithium−Oxygen Batteries. *Small* **2015**, 11 (41), 5545-5550.

90. Laoire, C. O.; Mukerjee, S.; Abraham, K. M.; Plichta, E. J.; Hendrickson, M. A., Influence of Nonaqueous Solvents on the Electrochemistry of Oxygen in the Rechargeable Lithium−Air Battery. *The Journal of Physical Chemistry C* **2010**, 114 (19), 9178-9186.

91. Gutmann, V., Solvent effects on the reactivities of organometallic compounds. *Coordination Chemistry Reviews* **1976**, 18 (2), 225-255.

92. Freunberger, S. A.; Chen, Y.; Drewett, N. E.; Hardwick, L. J.; Bardé, F.; Bruce, P. G., The Lithium–Oxygen Battery with Ether-Based Electrolytes. *Angewandte Chemie International Edition* **2011**, 50 (37), 8609-8613.

93. McCloskey, B. D.; Scheffler, R.; Speidel, A.; Bethune, D. S.; Shelby, R. M.; Luntz, A. C., On the Efficacy of Electrocatalysis in Nonaqueous Li–O_2 Batteries. *Journal of the American Chemical Society* **2011**, 133 (45), 18038-18041.

94. Yu, Q.; Ye, S., In Situ Study of Oxygen Reduction in Dimethyl Sulfoxide (DMSO) Solution: A Fundamental Study for Development of the Lithium–Oxygen Battery. *The Journal of Physical Chemistry C* **2015**, 119 (22), 12236-12250.

95. Sharon, D.; Afri, M.; Noked, M.; Garsuch, A.; Frimer, A. A.; Aurbach, D., Oxidation of Dimethyl Sulfoxide Solutions by Electrochemical Reduction of Oxygen. *The Journal of Physical Chemistry Letters* **2013**, 4 (18), 3115-3119.

96. Ottakam Thotiyl, M. M.; Freunberger, S. A.; Peng, Z.; Chen, Y.; Liu, Z.; Bruce, P. G., A stable cathode for the aprotic Li–O_2 battery. *Nature Materials* **2013**, 12, 1050.

97. Kwabi, D. G.; Batcho, T. P.; Amanchukwu, C. V.; Ortiz-Vitoriano, N.; Hammond, P.; Thompson, C. V.; Shao-Horn, Y., Chemical Instability of Dimethyl Sulfoxide in Lithium–Air Batteries. *The Journal of Physical Chemistry Letters* **2014**, 5 (16), 2850-2856.

98. Giordani, V.; Tozier, D.; Tan, H.; Burke, C. M.; Gallant, B. M.; Uddin, J.; Greer, J. R.; McCloskey, B. D.; Chase, G. V.; Addison, D., A Molten Salt Lithium–Oxygen Battery. *Journal of the American Chemical Society* **2016**, 138 (8), 2656-2663.

99. Han, H.-B.; Zhou, S.-S.; Zhang, D.-J.; Feng, S.-W.; Li, L.-F.; Liu, K.; Feng, W.-F.; Nie, J.; Li, H.; Huang, X.-J.; Armand, M.; Zhou, Z.-B., Lithium bis(fluorosulfonyl)imide (LiFSI) as conducting salt for nonaqueous liquid electrolytes for lithium-ion batteries: Physicochemical and electrochemical properties. *Journal of Power Sources* **2011**, 196 (7), 3623-3632.

100. Kubota, K.; Nohira, T.; Goto, T.; Hagiwara, R., Novel inorganic ionic liquids possessing low melting temperatures and wide electrochemical windows: Binary mixtures of alkali bis(fluorosulfonyl)amides. *Electrochemistry Communications* **2008**, 10 (12), 1886-1888.

101. Khan, A.; Zhao, C., Enhanced performance in mixture DMSO/ionic liquid electrolytes: Toward rechargeable Li–O_2 batteries. *Electrochemistry Communications* **2014**, 49, 1-4.

102. Ferrari, S.; Quartarone, E.; Tomasi, C.; Bini, M.; Galinetto, P.; Fagnoni, M.; Mustarelli, P., Investigation of Ether-Based Ionic Liquid Electrolytes for Lithium-O_2 Batteries. *J. Electrochem. Soc.* **2015**, 162 (2), A3001-A3006.

103. Neale, A. R.; Goodrich, P.; Hughes, T.-L.; Hardacre, C.; Ball, S. C.; Jacquemin, J., Physical and Electrochemical Investigations into Blended Electrolytes Containing a Glyme Solvent and Two Bis{(trifluoromethyl)sulfonyl}imide-Based Ionic Liquids. *J. Electrochem. Soc.* **2017**, 164 (8), H5124-H5134.

104. Hayyan, M.; Mjalli, F. S.; Hashim, M. A.; AlNashef, I. M., An investigation of the reaction between 1-butyl-3-methylimidazolium trifluoromethanesulfonate and superoxide ion. *Journal of Molecular Liquids* **2013**, 181, 44-50.

105. Nakamoto, H.; Suzuki, Y.; Shiotsuki, T.; Mizuno, F.; Higashi, S.; Takechi, K.; Asaoka, T.; Nishikoori, H.; Iba, H., Ether-functionalized ionic liquid electrolytes for lithium-air batteries. *Journal of Power Sources* **2013**, 243, 19-23.

106. Higashi, S.; Kato, Y.; Takechi, K.; Nakamoto, H.; Mizuno, F.; Nishikoori, H.; Iba, H.; Asaoka, T., Evaluation and analysis of Li-air battery using ether-functionalized ionic liquid. *Journal of Power Sources* **2013**, 240, 14-17.

107. Mozhzhukhina, N.; Tesio, A. Y.; De Leo, L. P. M.; Calvo, E. J., In Situ Infrared Spectroscopy Study of PYR14TFSI Ionic Liquid Stability for Li–O_2 Battery. *J. Electrochem. Soc.* **2017**, 164 (2), A518-A523.

108. Radjenovic, P. M.; Hardwick, L. J., Time-resolved SERS study of the oxygen reduction reaction in ionic liquid electrolytes for non-aqueous lithium–oxygen cells. *Faraday Discussions* **2018**, 206 (0), 379-392.

109. Piana, M.; Wandt, J.; Meini, S.; Buchberger, I.; Tsiouvaras, N.; Gasteiger, H. A., Stability of a Pyrrolidinium-Based Ionic Liquid in Li-O2 Cells. *J. Electrochem. Soc.* **2014**, 161 (14), A1992-A2001.

110. Das, S.; Højberg, J.; Knudsen, K. B.; Younesi, R.; Johansson, P.; Norby, P.; Vegge, T., Instability of Ionic Liquid-Based Electrolytes in Li–O_2 Batteries. *The Journal of Physical Chemistry C* **2015**, 119 (32), 18084-18090.

111. Elia, G. A.; Hassoun, J.; Kwak, W. J.; Sun, Y. K.; Scrosati, B.; Mueller, F.; Bresser, D.; Passerini, S.; Oberhumer, P.; Tsiouvaras, N.; Reiter, J., An Advanced Lithium–Air Battery Exploiting an Ionic Liquid-Based Electrolyte. *Nano Letters* **2014**, 14 (11), 6572-6577.

112. Wu, S.; Tang, J.; Li, F.; Liu, X.; Yamauchi, Y.; Ishida, M.; Zhou, H., A Synergistic System for Lithium–Oxygen Batteries in Humid Atmosphere Integrating a Composite Cathode and a Hydrophobic Ionic Liquid-Based Electrolyte. *Advanced Functional Materials* **2016**, 26 (19), 3291-3298.

113. Neale, A. R.; Li, P.; Jacquemin, J.; Goodrich, P.; Ball, S. C.; Compton, R. G.; Hardacre, C., Effect of cation structure on the oxygen solubility and diffusivity in a range of bis{(trifluoromethyl)sulfonyl}imide anion based ionic liquids for lithium–air battery electrolytes. *Physical Chemistry Chemical Physics* **2016**, 18 (16), 11251-11262.

114. Cecchetto, L.; Salomon, M.; Scrosati, B.; Croce, F., Study of a Li–air battery having an electrolyte solution formed by a mixture of an ether-based aprotic solvent and an ionic liquid. *Journal of Power Sources* **2012**, 213, 233-238.

115. Monaco, S.; Soavi, F.; Mastragostino, M., Role of Oxygen Mass Transport in Rechargeable Li/O_2 Batteries Operating with Ionic Liquids. *The Journal of Physical Chemistry Letters* **2013**, 4 (9), 1379-1382.

116. Allen, C. J.; Hwang, J.; Kautz, R.; Mukerjee, S.; Plichta, E. J.; Hendrickson, M. A.; Abraham, K. M., Oxygen Reduction Reactions in Ionic Liquids and the Formulation of a General ORR Mechanism for Li–Air Batteries. *The Journal of Physical Chemistry C* **2012**, 116 (39), 20755-20764.

117. Khetan, A.; Luntz, A.; Viswanathan, V., Trade-Offs in Capacity and Rechargeability in Nonaqueous Li–O_2 Batteries: Solution-Driven Growth versus Nucleophilic Stability. *The Journal of Physical Chemistry Letters* **2015**, 6 (7), 1254-1259.

118. Laoire, C. O.; Mukerjee, S.; Abraham, K. M.; Plichta, E. J.; Hendrickson, M. A., Elucidating the Mechanism of Oxygen Reduction for Lithium-Air Battery Applications. *The Journal of Physical Chemistry C* **2009**, 113 (46), 20127-20134.

119. Younesi, R.; Norby, P.; Vegge, T., A New Look at the Stability of Dimethyl Sulfoxide and Acetonitrile in Li-O_2 Batteries. *ECS Electrochemistry Letters* **2014**, 3 (3), A15-A18.

120. Walker, W.; Giordani, V.; Uddin, J.; Bryantsev, V. S.; Chase, G. V.; Addison, D., A Rechargeable Li–O_2 Battery Using a Lithium Nitrate/N,N-Dimethylacetamide Electrolyte. *Journal of the American Chemical Society* **2013**, 135 (6), 2076-2079.

121. Bryantsev, V. S.; Giordani, V.; Walker, W.; Uddin, J.; Lee, I.; van Duin, A. C. T.; Chase, G. V.; Addison, D., Investigation of Fluorinated Amides for Solid–Electrolyte Interphase Stabilization in Li–O_2 Batteries Using Amide-Based Electrolytes. *The Journal of Physical Chemistry C* **2013**, 117 (23), 11977-11988.

122. Zhou, B.; Guo, L.; Zhang, Y.; Wang, J.; Ma, L.; Zhang, W.-H.; Fu, Z.; Peng, Z., A High-Performance Li–O_2 Battery with a Strongly Solvating Hexamethylphosphoramide Electrolyte and a LiPON-Protected Lithium Anode. *Advanced Materials* **2017**, 29 (30), 1701568.

123. Luo, W.-B.; Chou, S.-L.; Wang, J.-Z.; Kang, Y.-M.; Zhai, Y.-C.; Liu, H.-K., A hybrid gel–solid-state polymer electrolyte for long-life lithium oxygen batteries. *Chemical Communications* **2015**, 51 (39), 8269-8272.

124. Wu, S.; Qiao, Y.; Yang, S.; Tang, J.; He, P.; Zhou, H., Clean Electrocatalysis in a Li_2O_2 Redox-Based Li–O_2 Battery Built with a Hydrate-Melt Electrolyte. *ACS Catalysis* **2018**, 8 (2), 1082-1089.

125. Kichambare, P.; Rodrigues, S.; Kumar, J., Mesoporous Nitrogen-Doped Carbon-Glass Ceramic Cathodes for Solid-State Lithium–Oxygen Batteries. *ACS Applied Materials & Interfaces* **2012**, 4 (1), 49-52.

126. Kumar, B.; Kumar, J.; Leese, R.; Fellner, J. P.; Rodrigues, S. J.; Abraham, K. M., A Solid-State, Rechargeable, Long Cycle Life Lithium–Air Battery. *J. Electrochem. Soc.* **2010**, 157 (1), A50-A54.

127. Landa-Medrano, I.; Olivares-Marín, M.; Bergner, B.; Pinedo, R.; Sorrentino, A.; Pereiro, E.; Ruiz de Larramendi, I.; Janek, J.; Rojo, T.; Tonti, D., Potassium Salts as Electrolyte Additives in Lithium–Oxygen Batteries. *The Journal of Physical Chemistry C* **2017**, 121 (7), 3822-3829.

128. Gao, X.; Chen, Y.; Johnson, L. R.; Jovanov, Z. P.; Bruce, P. G., A rechargeable lithium–oxygen battery with dual mediators stabilizing the carbon cathode. *Nature Energy* **2017**, 2, 17118.

129. Chen, Y.; Freunberger, S. A.; Peng, Z.; Fontaine, O.; Bruce, P. G., Charging a Li–O_2 battery using a redox mediator. *Nature Chemistry* **2013**, 5, 489.

130. Jian, Z.; Chen, Y.; Li, F.; Zhang, T.; Liu, C.; Zhou, H., High capacity Na–O_2 batteries with carbon nanotube paper as binder-free air cathode. *Journal of Power Sources* **2014**, 251, 466-469.

131. Sharon, D.; Hirsberg, D.; Afri, M.; Chesneau, F.; Lavi, R.; Frimer, A. A.; Sun, Y.-K.; Aurbach, D., Catalytic Behavior of Lithium Nitrate in Li-O_2 Cells. *ACS Applied Materials & Interfaces* **2015**, 7 (30), 16590-16600.

132. Kwak, W.-J.; Hirshberg, D.; Sharon, D.; Afri, M.; Frimer, A. A.; Jung, H.-G.; Aurbach, D.; Sun, Y.-K., Li–O_2 cells with LiBr as an electrolyte and a redox mediator. *Energy & Environmental Science* **2016**, 9 (7), 2334-2345.

133. Zhang, T.; Liao, K.; He, P.; Zhou, H., A self-defense redox mediator for efficient lithium–O_2 batteries. *Energy & Environmental Science* **2016**, 9 (3), 1024-1030.

134. Lim, H.-D.; Lee, B.; Zheng, Y.; Hong, J.; Kim, J.; Gwon, H.; Ko, Y.; Lee, M.; Cho, K.; Kang, K., Rational design of redox mediators for advanced Li–O_2 batteries. *Nature Energy* **2016**, 1, 16066.

135. Li, Y.; Gong, M.; Liang, Y.; Feng, J.; Kim, J.-E.; Wang, H.; Hong, G.; Zhang, B.; Dai, H., Advanced zinc-air batteries based on high-performance hybrid electrocatalysts. *Nature Communications* **2013**, 4, 1805.

136. Li, P.-C.; Chien, Y.-J.; Hu, C.-C., Novel configuration of bifunctional air electrodes for rechargeable zinc–air batteries. *Journal of Power Sources* **2016**, 313, 37-45.

137. Tang, C.; Wang, B.; Wang, H.-F.; Zhang, Q., Defect Engineering toward Atomic Co–Nx–C in Hierarchical Graphene for Rechargeable Flexible Solid Zn-Air Batteries. *Advanced Materials* **2017**, 29 (37), 1703185.

138. Othman, R.; Basirun, W. J.; Yahaya, A. H.; Arof, A. K., Hydroponics gel as a new electrolyte gelling agent for alkaline zinc–air cells. *Journal of Power Sources* **2001**, 103 (1), 34-41.

139. Mohamad, A. A., Zn/gelled 6M KOH/O_2 zinc–air battery. J*ournal of Power Sources* **2006**, 159 (1), 752-757.

140. Yang, C.-C.; Lin, S.-J., Alkaline composite PEO–PVA–glass-fibre-mat polymer electrolyte for Zn–air battery. *Journal of Power Sources* **2002**, 112 (2), 497-503.

141. Fu, J.; Lee, D. U.; Hassan, F. M.; Yang, L.; Bai, Z.; Park, M. G.; Chen, Z., Flexible High-Energy Polymer-Electrolyte-Based Rechargeable Zinc–Air Batteries. *Advanced Materials* **2015**, 27 (37), 5617-5622.

142. Masri, M. N.; Nazeri, M. F. M.; Mohamad, A. A., Sago Gel Polymer Electrolyte for Zinc-Air Battery. **2011**; Vol. 72, p 305-308.

143. Thomas Goh, F. W.; Liu, Z.; Hor, T. S. A.; Zhang, J.; Ge, X.; Zong, Y.; Yu, A.; Khoo, W., A Near-Neutral Chloride Electrolyte for Electrically Rechargeable Zinc-Air Batteries. *J. Electrochem. Soc.* **2014**, 161 (14), A2080-A2086.

144. Sumboja, A.; Ge, X.; Zheng, G.; Goh, F. W. T.; Hor, T. S. A.; Zong, Y.; Liu, Z., Durable rechargeable zinc-air batteries with neutral electrolyte and manganese oxide catalyst. *Journal of Power Sources* **2016**, 332, 330-336.

145. Mainar, A. R.; Iruin, E.; Colmenares, L. C.; Kvasha, A.; de Meatza, I.; Bengoechea, M.; Leonet, O.; Boyano, I.; Zhang, Z.; Blazquez, J. A., An overview of progress in electrolytes for secondary zinc-air batteries and other storage systems based on zinc. *Journal of Energy Storage* **2018**, 15, 304-328

146. Banik, S. J.; Akolkar, R., Suppressing Dendrite Growth during Zinc Electrodeposition by PEG-200 Additive. *J. Electrochem. Soc.* **2013**, 160 (11), D519-D523.

147. R. Black, B. Adams and L. F. Nazar, *Adv Energy Mater*, **2012**, 2, 801.

148. Y. Y. Shao, F. Ding, J. Xiao, J. Zhang, W. Xu, S. Park, J. G. Zhang, Y. Wang and J. Liu, *Adv Funct Mater*, **2013**, 23, 987.

149. P. G. Bruce, S. A. Freunberger, L. J. Hardwick and J. M. Tarascon, *Nat Mater*, **2012**, 11, 19.

150. Z. L. Jian, P. Liu, F. J. Li, P. He, X. W. Guo, M. W. Chen and H. S. Zhou, *Angew Chem Int Edit*, **2014**, 53, 442.

151. B. D. McCloskey, R. Scheffler, A. Speidel, D. S. Bethune, R. M. Shelby and A. C. Luntz, *J Am Chem Soc*, **2011**, 133, 18038.

152. M. M. O. Thotiyl, S. A. Freunberger, Z. Q. Peng and P. G. Bruce, *J Am Chem Soc*, **2013**, 135, 494.

153. N. N. Feng, P. He and H. S. Zhou, *Adv Energy Mater*, **2016**, 6.

154. S. C. Wu, J. Tang, F. J. Li, X. Z. Liu, Y. Yamauchi, M. Ishida and H. S. Zhou, *Adv Funct Mater*, **2016**, 26, 3291.

155. S. A. Freunberger, Y. H. Chen, N. E. Drewett, L. J. Hardwick, F. Barde and P. G. Bruce, *Angew Chem Int Edit*, **2011**, 50, 8609.

156. Y. C. Lu, D. G. Kwabi, K. P. C. Yao, J. R. Harding, J. G. Zhou, L. Zuin and Y. Shao-Horn, *Energ Environ Sci*, **2011**, 4, 2999.

157. J. Li, Y. Zhao, M. Zou, C. Wu, Z. Huang and L. Guan, *Acs Appl Mater Inter*, **2014**, 6, 12479.

158. K. M. Liao, T. Zhang, Y. Q. Wang, F. J. Li, Z. L. Jian, H. J. Yu and H. S. Zhou, *Chemsuschem*, **2015**, 8, 1429.

159. B. Wu, H. Zhang, W. Zhou, M. Wang, X. Li and H. Zhang, *Acs Appl Mater Inter*, **2015**, 7, 23182.

160. C. Y. Zhu, A. Nobuta, I. Nakatsugawa and T. Akiyama, *Int J Hydrogen Energ*, **2013**, 38, 13238.

161. K. A. Stoerzinger, W. S. Choi, H. Jeen, H. N. Lee and Y. Shao-Horn, *J Phys Chem Lett*, **2015**, 6, 487.

162. J. R. Petrie, V. R. Cooper, J. W. Freeland, T. L. Meyer, Z. Y. Zhang, D. A. Lutterman and H. N. Lee, *J Am Chem Soc*, **2016**, 138, 2488.

163. Z. Xie, H. Zhao, Z. Du, T. Chen, N. Chen, X. Liu and S. J. Skinner, *The Journal of Physical Chemistry C*, **2012**, 116, 9734.

164. K. H. L. Zhang, Y. Du, A. Papadogianni, O. Bierwagen, S. Sallis, L. F. J. Piper, M. E. Bowden, V. Shutthanandan, P. V. Sushko and S. A. Chambers, *Adv Mater*, **2015**, 27, 5191.

165. Y. Zhu, W. Zhou, J. Sunarso, Y. Zhong and Z. Shao, *Adv Funct Mater*, **2016**, 26, 5862.

166. G. S. Gallego, F. Mondragon, J. Barrault, J. M. Tatibouet and C. Batiot-Dupeyrat, *Appl Catal a-Gen*, **2006**, 311, 164.

167. S. M. Lima, J. M. Assaf, M. A. Pena and J. L. G. Fierro, *Appl Catal a-Gen*, **2006**, 311, 94.

168. J. Sunarso, A. A. J. Torriero, W. Zhou, P. C. Howlett and M. Forsyth, *J Phys Chem C*, **2012**, 116, 5827.

169. Z. Chen, A. P. Yu, D. Higgins, H. Li, H. J. Wang and Z. W. Chen, *Nano Lett*, **2012**, 12, 1946.

170. Y. X. Wu, T. H. Wang, Y. D. Zhang, S. Xin, X. J. He, D. W. Zhang and J. L. Shui, *Sci Rep-Uk*, 2016, **6**.

171. R. Gao, Z. Li, X. Zhang, J. Zhang, Z. Hu, X. Liu, *ACS Catalysis*, **2016**, 6, 400.

172. R. Gao, L. Liu, Z. Hu, P. Zhang, X. Cao, B. Wang, X. Liu, *J Mater Chem A*, **2015**, 3, 17598.

173. J. Zhang, Y. Zhao, X. Zhao, Z. Liu, W. Chen, *Sci Rep*, **2014**, 4, 6005.

174. S. M. d. Lima and J. M. Assaf, *Materials Research*, **2002**, 5, 329.

175. R. Pereñíguez, V. M. González-DelaCruz, J. P. Holgado and A. Caballero, *Applied Catalysis B: Environmental*, **2010**, 93, 346.

176. S. P. Jiang, L. Liu, K. P. Ong, P. Wu, J. Li and J. Pu, *J Power Sources*, **2008**, 176, 82.

177. J. Xiao, D. Mei, X. Li, W. Xu, D. Wang, G. L. Graff, W. D. Bennett, Z. Nie, L. V. Saraf, I. A. Aksay, J. Liu, J.-G. Zhang, *Nano Lett*, **2011**, 11, 5071

178. T. Zhang, K. Liao, P. He and H. Zhou, *Energ Environ Sci*, **2016**, 9, 1024.

179. D. Zhai, K. C. Lau, H.-H. Wang, J. Wen, D. J. Miller, F. Kang, B. Li, K. Zavadil and L. A. Curtiss, *Chemsuschem*, **2015**, 8, 4235.

180. M. Yu, X. Ren, L. Ma and Y. Wu, *Nat Commun*, **2014**, 5, 5111.

181. W.-J. Kwak, D. Hirshberg, D. Sharon, H.-J. Shin, M. Afri, J.-B. Park, A. Garsuch, F. F. Chesneau, A. A. Frimer, D. Aurbach and Y.-K. Sun, *J Mater Chem A*, **2015**, 3, 8855

182. Huang, X.; Zhao, Z.; Cao, L.; Chen, Y.; Zhu, E.; Lin, Z.; Li, M.; Yan, A.; Zettl, A.; Wang, Y. M.; Duan, X.;Mueller, T.; Huang, Y. Transition Metal–Doped Pt3Ni Octahedra for Oxygen Reduction Reaction Science, **2015**, 348, 1230

183.Chen, C.; Kang, Y.; Huo, Z.; Zhu, Z.; Huang, W.; Xin, H.L.; Snyder, J. D.; Li, D.; Herron, J. A.; Mavrikakis, M. Highly Crystalline Multimetallic Nanoframes with Three-Dimensional Electrocatalytic Surfaces Science, 2014, 343, 1339– 1343

184. Xia, X. H.; Wang, Y.; Ruditskiy, A.; Xia, Y. N. 25th Anniversary Article: Galvanic Replacement: A Simple and Versatile Route to Hollow Nanostructures with Tunable and Well-Controlled Properties *Adv. Mater.* **2013**, 25,6313

185. Rodriguez, J. A.; Kuhn, M.; Hrbek, J. Interaction of Sulfur with Au/Pt(111) and Ag/Pt(111) Surfaces: Photoemission Studies *J. Phys. Chem.* **1996**, 100, 15494

186. Cao, J. Y.; Liu, S. Y.; Xie, J.; Zhang, S. C.; Cao, G. S.; Zhao, X. B. Tips-Bundled Pt/Co_3O_4 Nanowires with Directed Peripheral Growth of Li_2O_2 as Efficient Binder/Carbon-Free Catalytic Cathode for Lithium-Oxygen Battery ACS Catal. 2015, 5, 241

187. Milošv, I.; Strehblow, H. H.; Navinšek, B.; Metikoš-Huković, M. Electrochemical and Thermal Oxidation of TiN Coatings Studied by XPS *Surf. Interface Anal.* **1995**, 23, 529

188. Avasarala, B.; Haldar, P. Electrochemical Oxidation Behavior of Titanium Nitride Based Electrocatalysts Under PEM Fuel Cell Conditions *Electrochim. Acta* **2010**, 55, 9024

189.Lu, X.; Wang, G.; Zhai, T.; Yu, M.; Xie, S.; Ling, Y.; Liang, C.; Tong, Y.; Li, Y. Stab ilized TiN Nanowire Arrays for High-Performance and Flexible Supercapacitors *Nano Lett.* **2012**, 12, 5376

190.Wang, G.; Wang, H.; Ling, Y.; Tang, Y.; Yang, X.; Fitzmorris, R.C.; Wang, C.; Zhang, J. Z.; Li, Y. Hydrogen-Treated TiO_2 Nanowire Arrays for Photoelectrochemical Water Splitting *Nano Lett.* **2011**, 11, 3026

191.Chen, S.; Ferreira, P. J.; Sheng, W. C.; Yabuuchi, N.; Allard, L. F.; Shao-Horn, Y. Enhanced Activity for Oxygen Reduction Reaction on $''Pt_3C_O''$ nanoparticles: Direct Evidence of Percolated and Sandwich-Segregation Structures *J. Am. Chem. Soc.* **2008**, 130, 13818

192. Cui, C. H.; Gan, L.; Li, H. H.; Yu, S. H.; Heggen, M.; Strasser, P. Octahedral PtNi Nanoparticle Catalysts: Exceptional Oxygen Reduction Activity by Tuning the Alloy Particle Surface Composition *Nano Lett.* **2012**,12, 5885

193. Jian, Z. L.; Liu, P.; Li, F. J.; He, P.; Guo, X. W.; Chen, M. W.; Zhou, H. S. Core-Shell-Structured CNT@RuO_2Composite as A High-Performance Cathode Catalyst for Rechargeable Li-O_2 Batteries *Angew. Chem., Int. Ed.* **2014**, 53, 442

194. V. R. Stamenkovic, B. Fowler, B. S. Mun, G. Wang, P. N. Ross, C. A. Lucas, N. M. Marković, Science **2007**, 315, 493.

195. I. E. L. Stephens, A. S. Bondarenko, U. Gronbjerg, J. Rossmeisl, I. Chorkendorff, Energy & Environmental Science **2012**, 5, 6744.

196. C. Cui, L. Gan, H.-H. Li, S.-H. Yu, M. Heggen, P. Strasser, Nano Letters **2012**, 12, 5885.

197. J. D. Ferguson, G. Arikan, D. S. Dale, A. R. Woll, J. D. Brock, Physical Review Letters **2009**, 103, 256103.

198. C. Chen, Y. Kang, Z. Huo, Z. Zhu, W. Huang, H. L. Xin, J. D. Snyder, D. Li, J. A. Herron, M. Mavrikakis, M. Chi, K. L. More, Y. Li, N. M. Markovic, G. A. Somorjai, P. Yang, V. R. Stamenkovic, Science **2014**, 343, 1339.

199. N. Cao, L. Yang, H. Dai, T. Liu, J. Su, X. Wu, W. Luo, G. Cheng, Inorganic Chemistry **2014**, 53, 10122.

200. J. Zhang, Z. Zhao, Z. Xia, L. Dai, Nature Nanotechnology **2015**, 10, 444.

201. J.-J. Xu, Z.-L. Wang, D. Xu, F.-Z. Meng, X.-B. Zhang, Energy & Environmental Science **2014**, 7, 2213.

202. Z. Zhang, H. Li, J. Hu, B. Liu, Q. Zhang, C. Fernandez, Q. Peng, Journal of Alloys and Compounds **2017**, 694, 419.

203. X. Ge, Y. Liu, F. W. T. Goh, T. S. A. Hor, Y. Zong, P. Xiao, Z. Zhang, S. H. Lim, B. Li, X. Wang, Z. Liu, ACS Applied Materials & Interfaces **2014**, 6, 12684.

204. T. An, X. Ge, T. S. A. Hor, F. W. T. Goh, D. Geng, G. Du, Y. Zhan, Z. Liu, Y. Zong, RSC Advances **2015**, 5, 75773.

205. J. X. Wang, H. Inada, L. Wu, Y. Zhu, Y. Choi, P. Liu, W.-P. Zhou, R. R. Adzic, Journal of the American Chemical Society **2009**, 131, 17298.

206. A. Kraytsberg, Y. Ein-Eli, Nano Energy **2013**, 2, 468.

207. X. Liu, M. Park, M. G. Kim, S. Gupta, X. Wang, G. Wu, J. Cho, Nano Energy **2016**, 20, 315.

208. X. Wang, Y. Li, T. Jin, J. Meng, L. Jiao, M. Zhu, J. Chen, Nano Letters **2017**, 17, 7989.

209. T. Cheng, W. Bin, W. Hao-Fan, Z. Qiang, Advanced Materials **2017**, 29, 1703185.

210. Y. Jin, F. Chen, Electrochimica Acta **2015**, 158, 437.

211.Z. Cui, H. Chen, M. Zhao, F. J. DiSalvo, Nano Letters **2016**, 16, 2560.

212.Z. Guo, C. Li, W. Li, H. Guo, X. Su, P. He, Y. Wang, Y. Xia, Journal of Materials Chemistry A **2016**, 4, 6282.

213.X. Wu, F. Chen, Y. Jin, N. Zhang, R. L. Johnston, ACS Applied Materials & Interfaces **2015**, 7, 17782.

214.J. Hu, Q. Liu, L. Shi, Z. Shi, H. Huang, Applied Surface Science **2017**, 402, 61.

215.M. Chao, L. Tao, M. Tian-Yi, W. Hui, H. Zhenpeng, Z. Yue, M. Jing, D. Xi-Wen, J. Mietek, Q. Shi-Zhang, Advanced Materials **2017**, 29, 1604607.

216. Y. Li, M. Gong, Y. Liang, J. Feng, J.-E. Kim, H. Wang, G. Hong, B. Zhang, H. Dai, Nature Communications **2013**, 4, 1805.

217. B. Li, J. Quan, A. Loh, J. Chai, Y. Chen, C. Tan, X. Ge, T. S. A. Hor, Z. Liu, H. Zhang, Y. Zong, Nano Letters **2017**, 17, 156.

218. J. Fu, J. Zhang, X. Song, H. Zarrin, X. Tian, J. Qiao, L. Rasen, K. Li, Z. Chen, Energy & Environmental Science **2016**, 9, 663.

219. J. Vatsalarani, D. C. Trivedi, K. Ragavendran, P. C. Warrier, Journal of the Electrochemical Society **2005**, 152, A1974.

220. F. Meng, H. Zhong, D. Bao, J. Yan, X. Zhang, Journal of the American Chemical Society **2016**, 138, 10226.

APPENDIX PUBLICATIONS

1. **T. V. Pham**, H. P. Guo, W. B. Luo, S. L. Chou, J. Z. Wang, H. K. Liu, *J, Carbon- and binder-free 3D porous perovskite oxide air electrode for rechargeable lithium–oxygen batteries. Journal of Materials Chemistry A* **2017**, 5, 5283.

2. W.-B. Luo, **T. V. Pham**, H.-P. Guo, H.-K. Liu, S.-X. Dou, Three-Dimensional Array of TiN@Pt_3Cu Nanowires as an Efficient Porous Electrode for the Lithium-Oxygen Battery. *ACS Nano* **2017**, 11, 1747.

3. **T. V. Pham**, Y. Li, W.-B. Luo, H. P. Guo, J. Z. Wang, H. K. Liu Binder-free 3D Integrated Ni@Ni_3Pt Air Electrode for Zn-Air Battery. *Global Challenges* **2019**, 1900027.